SPATIAL-TEMPORAL OCEAN VARIABILITY ON THE NORTHWEST SLOPE OF FLEMISH CAP

by

Chantelle Layton

Submitted in partial fulfillment of the requirements
for the degree of Master of Science

at

Dalhousie University
Halifax, Nova Scotia
November 2016

Table of Contents

List of Tables

List of Figures

Abstract

The Flemish Cap is a region impacted by human activities ranging from offshore petroleum exploration to international fisheries. This is an area of complex bathymetry and ocean circulation that is also characterized by vulnerable marine ecosystems within the benthic zone. This is a region with few long-term moored measurements of ocean properties due to the risks associated with bottom-trawl fisheries. In an attempt to address the need for science-based advice in this area, three oceanographic moorings placed in the region of northwest Flemish Cap from July 2013 to July 2014 gave some of the first long-term moored measurements of velocity, temperature, and salinity. These time series measurements were supplemented with two hydrographic surveys, in which stations were aligned in the cross-isobath direction about each mooring. These data allowed for a summary of the spatial variability over 10 to 200 km and temporal variability from an hour to a year. The spatial analysis of velocity along the northern Flemish Cap shows an easterly intensified flow that extends throughout the water column over the slope ($\sim 1200 - 2200$ m). Spectral analysis of the moored velocity measurements revealed a prominent 3-week peak. This was laterally and vertically coherent, and the power increased towards the bottom. A dynamical analysis in terms of the dispersion relationship indicates that these signatures were consistent with baroclinic topographic Rossby waves.

List of Abbreviations and Symbols Used

Roman symbol	Description	Units
a	number of Rossby radi	
ADCP	Acoustic doppler current profiler	
B_w	Bandwidth	cycle/hour
CFC	Chloroflurocarbon	
CTD	Conductivity, temperature, depth sensor	
df	adjusted degrees of freedom	
DWBC	Deep western boundary current	
f	Coriolis parameter	1/s
$F(z)$	Vertical structure of pressure anomaly	
g	gravity	m/s^2
g'	reduced gravity	m/s^2
H	Water depth	m
h_k	coefficients of modified Daniell kernel	
I	identity matrix	
k	eastward wavenumber component	1/m
k	parameter for cluster analysis	
LADCP	Lowered acoustic doppler profile	
l	northward wavenumber component	1/m
L	distance	m
L_R	baroclinic Rossby radius	m
LSW	Labrador sea water	
M2	Principal lunar semi-diurnal	
MF	Lunar solar fortnightly	
MM	Lunar monthly	
MSM	Solar monthly	
n	number of observations	
N	Brunt-Vaisala frequency	1/s

Roman symbol	Description	Units
N^2	Buoyancy frequency	$1/s^2$
NAC	North Atlantic current	
p	Pressure	dbar
P_0	point in longitude and latitude	
P_D	maximum depth points	
P_S	minimum depth points	
PV	Potential vorticity	$K\,m^2\,kg^{-1}\,s^{-1}$
R	ratio of kinetic energy	
RCM	Recording current meter	
S2	Principal solar semi-diurnal	
SA	Solar annual	
SSA	Solar semi-annual	
S	Salinity	
SST	Sea surface temperature	°C
Sv	Sverdrup	10^6 m^3/s
T	Temperature	°C
u	eastward velocity component	m/s
U	Speed	m/s
ULSW	Upper Labrador sea water	
v	northward velocity component	m/s
VADCP	Vessel mounted acoustic doppler profiler	
w	z-direction velocity component	m/s
$\vec{x}$	eigenvector	
z_1	shallow depth	m
z_2	deeper depth	m

Greek symbol	Description	Units
α	Bottom slope	
β	df/dy	m^{-1} s^{-1}
θ_b	Along isobath angle	
θ	Angle between isobath and velocity vector	
θ	latitude	°N

Greek symbol	Description	Units
θ_v	Principal axis of velocity vectors	
κ_H	Horizontal wavenumber	1/m
λ	eigenvalue	
λ	longitude	°W
μ_i	expected values	
π	spiciness	kg/m^3
ρ	density	kg/m^3
ρ_0	depth average density	kg/m^3
$\sum_{i,j}$	$n \times n$ covariance matrix	
σ_θ	potential density anomaly of water	kg / m^3
Φ	phase	radians
Φ	angle of rotation	
ϕ	central angle	
ϕ_n	heading	
ϕ_c	positive angle anti-clockwise	
ω	frequency	cycle/hr

Acknowledgements

"I want to wish you all that you would find your own voice. But if you are so disposed that you would find collaborators to work with, that you would shine as you could never shine on your own..."

– The Edge, *Berklee College Commencement, 2007*

The work completed in this thesis could not have been accomplished without the support of the small number of people I keep close in my life.

To my supervisor, Dan, thanks for putting up with me for an additional 2 years after supervising my honours research. The knowledge, skills, and personal connections I gained from you are some that I will hold onto for the rest of my life. Thanks for introducing and thus making me fluent in R and LaTeX, both of which will forever feed my obsessive nature. I have truly valued our time together and look forward to our future collaborations. PS - get that book published !

I would like to thank Blair and Dave for giving me the opportunity to work and have complete freedom with this unique data set. Without the support you provided, this degree would not have been able to be completed in a timely manner. I am also forever grateful for the employment after the completion of my degree.

I would like to express my gratitude to the instructor, Erica, and the regulars of "Strong Return Fitness". Without the weekly Sunday and Wednesday bootcamps, I would have most likely lost my sanity, though we are all insane for returning every week, especially during Erica's pregnancies.

To Tom, thanks for our friendship, unlocking my sense of adventure, and all of life's twists and turns. Thanks to my sister for our daily communication and for keeping humour in my life. And finally, to my parents (Monique and Al, Rick and Aimee), thanks for your continued support, and for never questioning my career path.

Chapter 1

Introduction

Flemish Cap is an area of geological, biological, and dynamical interest due to its hydrocarbon drilling potential, vulnerable marine ecosystems, and importance to the dynamics of the Labrador current.

Geologically, the Flemish pass basin is stratigraphically similar to the well known shallow water oil reserves in the Jeanne d'Arc Basin, which is home to the worlds largest oil platform, Hibernia (*Lowe et al.*, 2011). In 2009, oil was discovered by StatoilHydro and Husky in the O-16 Mizzen leave block on the south side of Sackville Spur at the northern edge of Flemish Pass. The amounts found were significant enough to obtain a discovery licence. Statoil was granted a discovery licence in 2013, drilling began in late 2014, continued for 19 months, and ended in May 2016[1]. Initial estimates of total recoverable oil in the basin was 300 to 600 million barrels. After the initial drilling period, total recoverable oil was on the lower end of these estimates[1]. Statoil's future plans for drilling remain to be determined[1]. While having real time current data is common practice for offshore drilling locations, general information about a region's current variability aids for engineering purposes, as well as evaluating potential environmental impact on the biology in the event of a spill.

The northwest Flemish Cap region is associated with three fisheries which include Greenland halibut, shrimp, and thorny skate (*González-Costas and González-Troncoso*, 2009). Two of these fisheries rely on bottom trawling as the fishing technique, which consequently results in benthic by-catch. Benthic surveys conducted between 2001 and 2009 revealed evidence of high trawling activity along Sackville Spur, northwest Flemish Cap, and along the western slopes of Flemish Pass, as well as sponge and coral biomass greater than 15 kg/ha as seen in

[1] See `http://www.statoil.com/en/NewsAndMedia/News/2016/Pages/10jun-newfoundland.aspx`, last visited 2016-09-08.

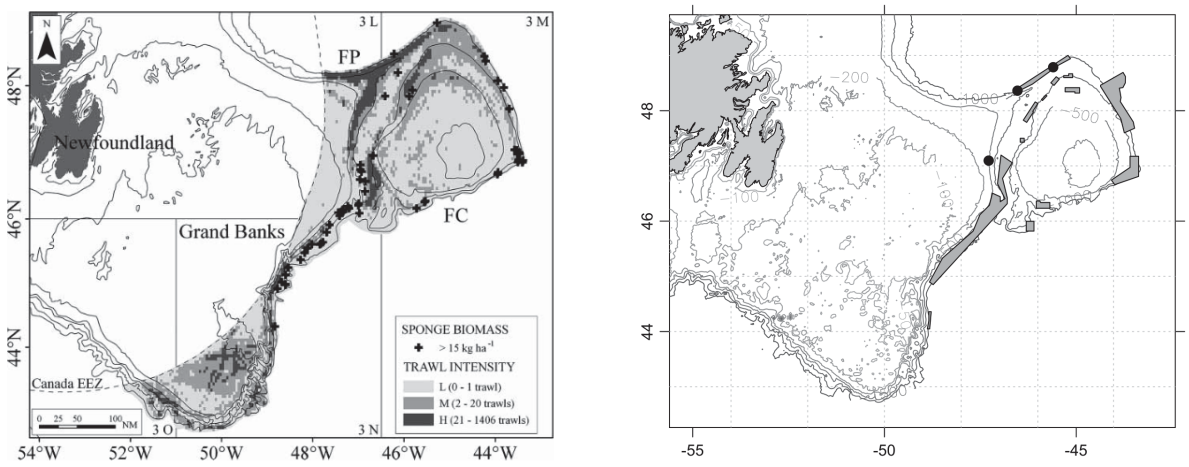

(a) (b)

Figure 1.1: (a) Trawling intensity and areas where sponge biomass was greater than 15 kg/ha reproduced from Figure 5 in *Murillo et al.* (2012). (b) Sponge and coral closures indicated by grey boxes valid for 2015 (*Northwest Atlantic Fisheries Organization*, 2015) and black dots indicate 2013-2014 mooring locations.

Figure 1.1 (*Murillo et al.*, 2011, 2012). Significantly higher sponge biomass in low trawling areas suggests either long term trawling activity or habitat preferences for sponges. Since 2003, sponge colonies have been labelled as being under immediate threat (*OSPAR*, 2008). Due to the significant sponge biomass near high trawling regions, 12 areas were closed to bottom fishing (Figure 1.1) at the beginning of 2011, and will remain closed until 2020 [2]. The goal of the closures is to monitor sponge colonies and determine if bottom trawling disrupts preferential habitats of the sponges. Presently, the preferential oceanographic properties of the colonies remains unknown. General hydrographic properties are in agreement with other colonies in the northeast Atlantic (*Murillo et al.*, 2012). The physical properties, such as bathymetry and background flow, have been suggested as factors which could influence or limit the spatial coverage of sponge colonies in this region, but this relationship remains to be investigated (*Murillo et al.*, 2012).

Few long-term oceanographic mooring measurements have been made in the northwest Flemish Cap region due to high trawling activity (*Petrie and Buckley*, 1996). This has limited measurement of the physical effects on sponge colonies, as well as large scale physical dynamics. While long term measurements of the Eulerian scheme (*e.g* moorings) have been

[2]See `http://www.fao.org/in-action/vulnerable-marine-ecosystems/vme-database/en/`, last visited 2016-09-08.

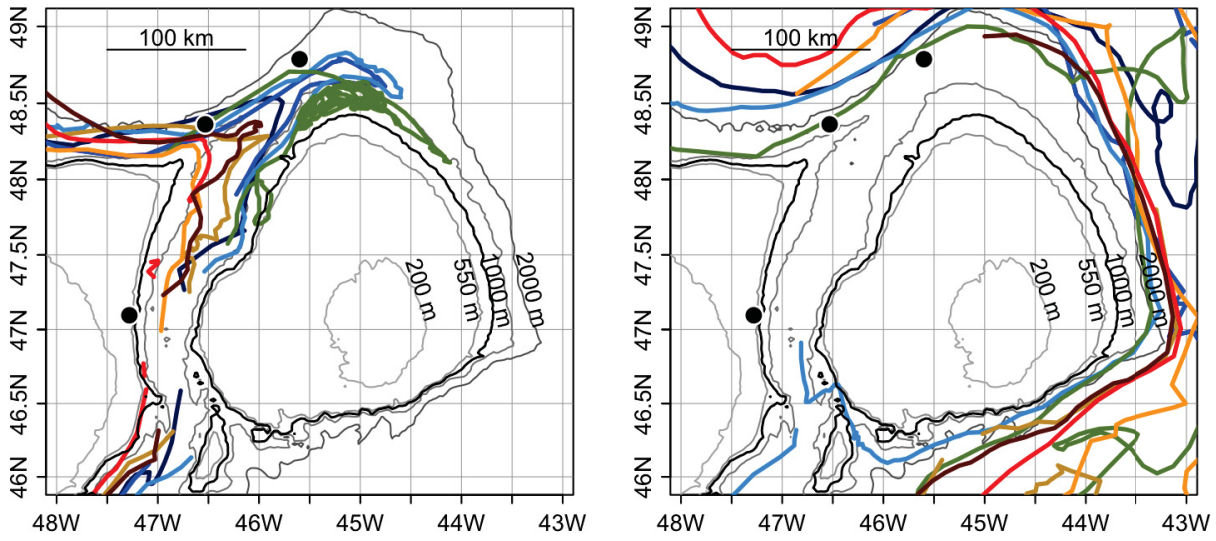

Figure 1.2: Sample of RAFOS floats ballasted for 700 m. (Left) Floats which passed went through Flemish Pass (Right) Subset of floats which did not travel through Flemish Pass.

sparse, there has been a comprehensive study of the Lagrangian perspective of the region observed via RAFOS floats. RAFOS floats are acoustically tracked and can be ballasted to a constant depth or density (more information on the technology can be found in *Rossby* (2016)). The major float project in the region is Amy Bower's "Export Pathways from the sub-polar North Atlantic" in which floats were ballasted to a constant depth (Figure 1.2). In this study, floats were ballasted for 700 m and 1500 m, and released at 4 stations across the continental slope around 50° N. From 2003 to 2008, 4 to 6 floats were released every season (*Bower et al.*, 2011). Fifty-five floats were released, with 28 ballasted for 700 m. The 8 which travelled through Flemish Pass were released at the two near-shore stations around 50°N(Figure 1.2). The other 20 floats ballasted for 700 m continued around Flemish Cap, and were then exported to the sub-polar basin or continued south to the Grand Banks. The path of each float that travels through the pass is spatially and temporally variable. While the Lagrangian perspective can give insight about transport pathways, the Eulerian point of view makes it simpler to study longer timescale processes, as well as applying theoretical knowledge about the ocean. Past studies have identified variable total transport through Flemish Pass, but associated physical processes driving bifurcation variability using observations have yet to be explained (*Schneider et al.*, 2015). While the recently obtained measurements lack the lateral coverage to resolve the bifurcation dynamics in detail, a study of the low frequency

dynamics allow for some insight on the departure about the mean flow.

In this thesis, I will address the Eulerian temporal and spatial variability of the circulation and hydrography of the northwest Atlantic Ocean using some of the first complete long term measurements of velocity, temperature, and salinity in the closed fishing areas in the northwest Flemish Cap region.

Chapter 2 will cover the spatial and temporal variability of hydrography and velocity on the study region. Two hydrographic surveys were completed during the deployments of the three moorings, which included CTD and LADCP measurements in July 2013 and 2014. The resultant data will be used to describe the spatial variability between transects for each year. The details of the temporal variability will be investigated using a full year of moored current meter and hydrographic data for each mooring location. A major finding from the analysis in Chapter 2 is that the moored current meter data revealed a significant spectral peak with a timescale of 3-weeks. At this spectral peak, the spectra power increased as depth increased, vertical and lateral coherence, and a tight velocity ellipse.

The temporal variability discussed in Chapter 2 indicated signatures of topographic Rossby waves. Chapter 3 will further test if these indicators are consistent with Rossby waves using the dispersion relationship. Theory presented by *Rhines* (1970) will be used in parallel with single mooring methods of *Thompson and Luyten* (1976) to find parameters for the dispersion relationship and conclusions will be drawn.

Chapter 2

Spatial-Temporal Hydrographic and Velocity Variability

2.1 Introduction

2.1.1 General Circulation

The major currents in the north-west Atlantic, shown in Figure 2.1, are the northward flowing North Atlantic Current (NAC), and the southward flowing western boundary current (WBC), or the Labrador Current, with the latter being the main topic of this thesis. The strength and intensity of the Labrador Current is annually variable, and thus the total transport of Labrador Sea water varies (*Kieke et al.*, 2006). The expected main pathway of the current follows contours of barotropic potential vorticity, f/H where f is Coriolis parameter and H is water depth, along the western continental slope (*Lazier and Wright*, 1993). Once it reaches Hamilton Bank, 15% of the total transport travels inshore and is referred to as the coastal branch which follows the coast of Newfoundland, and the remaining 85% continues southward along the continental slope (*Lazier and Wright*, 1993). When the main branch reaches the Flemish Cap area, 70 - 85% flows around the cap, and the remainder flows through Flemish Pass (*Schneider et al.*, 2015). These two branches then meet near the tail of the Grand Banks and continue to flow southward along the eastern seaboard of Canada and the United States. This pathway has been confirmed using multiple methods such as hydrographic surveys and moored current meters (*Lazier and Wright*, 1993; *Mertens et al.*, 2014), dynamical tracers (*Talley and McCartney*, 1982), and chemical tracers (*Kieke et al.*, 2006). While these methods infer pathways given sufficient amount of data, they do not give the Lagrangian perspective of a given particle which could be influenced by eddies and

Figure 2.1: Schematic of current flow in North Atlantic adapted from Figure 1 of *Lazier and Wright* (1993).

other physical processes. Recent float studies, *Bower et al.* (2011) and *Fischer and Schott* (2002) have indicated that floats ballasted for deeper depths (1500m) were more susceptible to getting exported to the sub-polar basin, whereas shallower floats better outline the expected pathway along bathymetry (*Lavender et al.*, 2000; *Fischer and Schott*, 2002; *Bower et al.*, 2011). In this thesis, the spatial variability of the general circulation will be summarized using hydrographic surveys.

2.1.2 Water masses

Two signature water masses have been defined in the literature pertaining to the Labrador Sea. These water masses are transported southward by the Labrador Current and surround Flemish Cap (*Pickart*, 1996). The less dense variant, termed Upper Labrador Sea Water (ULSW), may be detected by its chlorofluorocarbon (CFC) concentration and its fresher signal compared to the more dense variant (*Kieke et al.*, 2006). Near the site of formation, ULSW has CFC-11 concentration of 4.6-5.0 pmol/kg, and as it travels southward the concentration drops to 4.2-4.4 pmol/kg around Flemish Cap (*Kieke et al.*, 2006). Vertical maximum CFC-11 concentration in ULSW follow contours of barotropic potential vorticity (*Kieke et al.*, 2006). ULSW has a density range of σ_θ= 27.68-27.74 kg/m^3, with a core salinity of 34.80 (*Pickart*, 1996; *Stramma et al.*, 2004) as illustrated in Figure 2.2. The average ULSW transport during the time period 2009 to 2013 is 6.3 $\pm$0.5 Sv, with 1.2 $\pm$ 0.1 Sv passing through Flemish Pass,

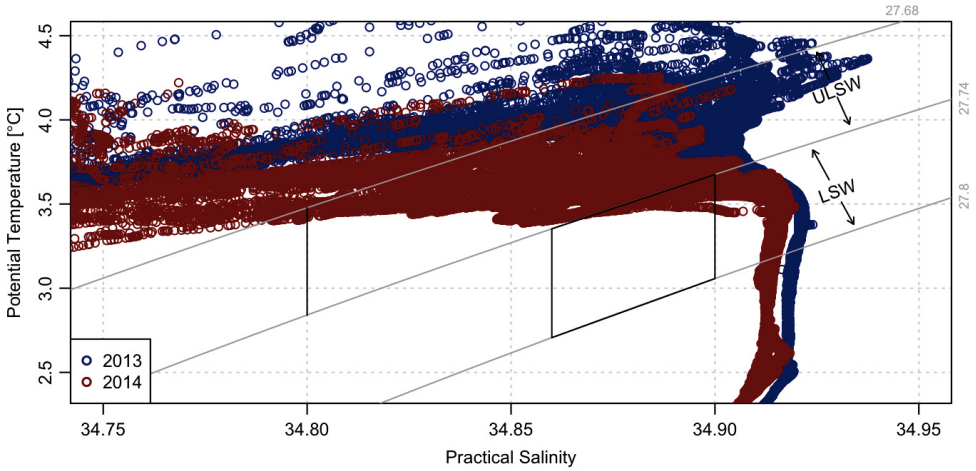

Figure 2.2: Temperature - salinity plot of all hydrographic stations for 2013 and 2014 sampled near Sackville Spur. Isopycnal lines indicate boundaries of watermass signatures for ULSW and LSW as indicated in the literature.

and 5.1±0.4 Sv being transported along the eastern side of Flemish Cap from measurements taken at the same latitude (*Schneider et al.*, 2015).

The second, more dense, water mass is Labrador Sea Water (LSW). It is formed through wintertime convection, which results in a thick homogeneous layer, so a vertical minimum in potential vorticity ($PV = f\rho_z/\rho$) may be used as a dynamical tracer (*Talley and McCartney*, 1982). A study by *Talley and McCartney* (1982) indicated PV values associated with LSW in the range of 2-6$\times 10^{-12}$ m^{-1} s^{-1}. *Stramma et al.* (2004) reported values at 56°N to be 2$\times 10^{-12}$ m^{-1} s^{-1}. LSW has a density of σ_θ= 27.74-27.80 kg/m^3, a salinity range of 34.86-34.90, a core temperature of 2.9°C and a core salinity of 34.865-34.869 (*Pickart*, 1996; *Stramma et al.*, 2004; *Talley and McCartney*, 1982). Water mass density ranges for ULSW and LSW and core properties on a temperature salinity diagram are summarized in Figure 2.2. The literature values characterizing ULSW and LSW do no align with these data. The values summarized in the literature may not reflect the temporal variability of these water masses (*Stramma et al.*, 2004).

Near the site of formation in the Labrador Sea (roughly 56°N, 50°W) ULSW is found from 100-1000 m and LSW from 900-2000 m (*Kieke et al.*, 2006). The temporal variation of water mass depth and thickness is dependent on wintertime convection strength: if winter convection is strong, the LSW layer will be thick and ULSW will be thin (*Kieke et al.*, 2006). This results in temporally variable deep watermass properties which is reflected in Figure 2.2,

	σ_θ (kg/m^3)	S	T (°C)	depth (m)
ULSW	27.68 - 27.74	34.8*	2.84 - 3.48**	100 - 1000†
LSW	27.74 - 27.8	34.86-34.9	2.71 - 3.68**	900 - 2000†

* core value

** inferred from σ_θ and S

† estimated at site of formation

Table 2.1: Summary of ULSW and LSW hydrographic properties as indicated in literature as indicated in text.

with the 2013 CTD observations being saltier than 2014.

2.1.3 Recent Observations

In 2013, three moorings were deployed, one on the northwest slope of Flemish Cap, a second on the northern slope of Sackville Spur, and a third on the western slope of central Flemish Pass (Figure 2.3). The moorings were equipped with a combination of three instruments, a Teledyne RDI LongRanger acoustic Doppler current profiler (ADCP), Aanderaa current recording meters (RCM), and Sea-Bird microCATs. Both ADCPs and RCMs measure horizontal velocity components. MicroCATs measure temperature and conductivity, and are also equipped with pressure sensors. The ADCPs sample in 8 m bins and have a reporting period of 1 hour. The RCMs have a sampling frequency of 1 hour, the microCATs of 5 minutes. The Flemish Cap and Sackville Spur mooring are similar in setup. An upward-looking ADCP is placed at 200 m, and RCMs and microCATs are placed at 350 m, then every 200 m down to 1350 m. The Flemish Pass mooring has an upward-looking ADCP at 400 m and one microCAT at 400 m. The moorings give a year of high frequency observations at a moderate vertical resolution. A detailed summary of the mooring configurations is provided in Appendix A

More detailed spatial resolution is provided at isolated times by hydrographic surveys in 2013 and 2014, each of which occurred during the first weeks in July (Figure 2.3). Data collected include CTD, lowered ADCP (LADCP), and vessel mounted ADCP (VADCP). Sampling stations in 2013 were repeated in 2014. Due to time constraints in 2014, Flemish Pass sampling stations were not repeated, and there were fewer stations along the 2014 Flemish Cap transect.

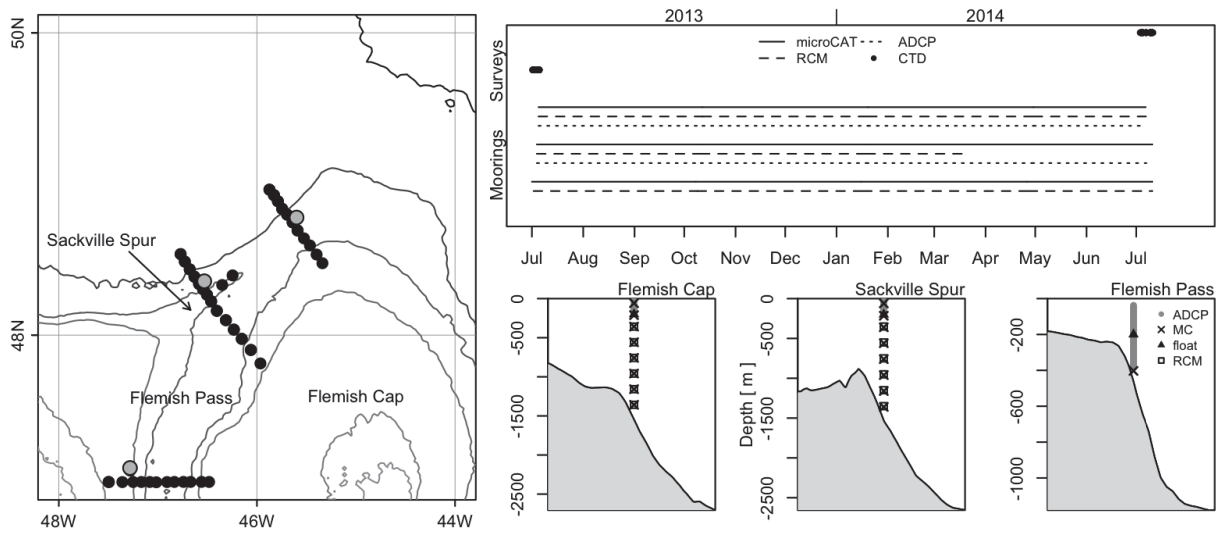

Figure 2.3: (Left) Map of CTD stations (black dots) and mooring locations (grey dots). (Top right) Time line of hydrographic surveys and moorings. (Bottom right) Vertical configuration of instruments for each mooring.

2.2 Sea Surface Temperature

In order to obtain a spatial-temporal view of the region satellite sea-surface temperature (SST) will be used in addition to the mooring and ship-based measurements. Of the many SST satellite products that are available, AMSR2 was chosen due to its ability to see through clouds, and its high sampling frequency of two swaths of the entire earth per day[1].

Three years of SST, 2013 to 2015, were obtained[2]. Figure 2.4 illustrates the data with a Hovmöller diagram for two transects roughly following the region bathymetry, one oriented east-west, the other oriented north-south. Observed SST in both transects reveal a strong seasonal signal. Note in particular that there are missing data during early spring in both years; this is a gap in a period that will prove of interest later in this thesis. In 2014, for the north-south transect the missing data region is from rain and ice, with 33% due to rain and 67% due to ice. In 2015, for the north-south transect the missing data region is from rain and ice, with 36% due to rain and 64% due to ice. In 2014, for the east-west transect the missing data region is from rain and ice, with 54% due to rain and 46% due to ice. In 2015, for the east-west transect the missing data region is from rain and ice, with 36% due to rain and 64% due to ice.

[1]See http://www.remss.com/missions/amsr for more information.

[2]Obtained from ftp site `ftp://ftp.ssmi.com/amsr2/bmaps_v07.2` on 4 February 2016

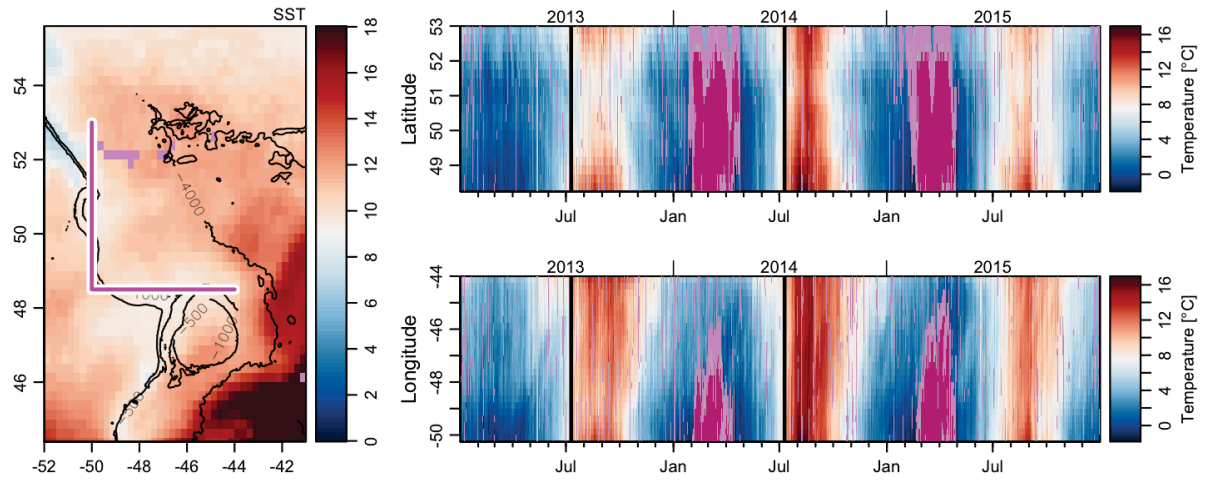

Figure 2.4: Time series of SST for two transects. (Left) Example of SST from AMSR2 with north-south and east-west transects indicated by magenta lines. Raw time-series from February 2013 - December 2015 for the (Top Right) north-south transect and (Bottom Right) east-west transect. Vertical black lines indicate mooring sampling dates. Dark pink indicates missing data due to ice and light pink indicates missing data due to rain.

In order to remove seasonal effects, a simple model,

$$SST_m = A + Bt + C\sin(\omega t) + D\cos(\omega t) + E\sin(2\omega t) + F\cos(2\omega t) \tag{2.1}$$

was used. The first two terms summarize the mean SST and a linear increase over time. Terms three and four describe the trend over the course of a year (*i.e.* $\omega = 2\pi/1\text{year}$), and the fifth and sixth term describe the semi-annual trend. This model was applied to the time series at each spatial point, and model results were subtracted from the raw data, yielding a anomaly field, $SST_a = SST - SST_m$. Both transects suggest evidence of fluctuations about the anomaly field. Parallel lines are placed to guide the eye and suggest portions of the year where periodic anomalous signals are present. In the north-south direction, the periodic anomalous signals suggest a period of 54 days, with an estimated northward velocity component of -0.11 m/s. Similarly, in the east-west direction, SST_a suggests a period of 40 days, with an estimated eastward velocity component of 0.2 m/s.

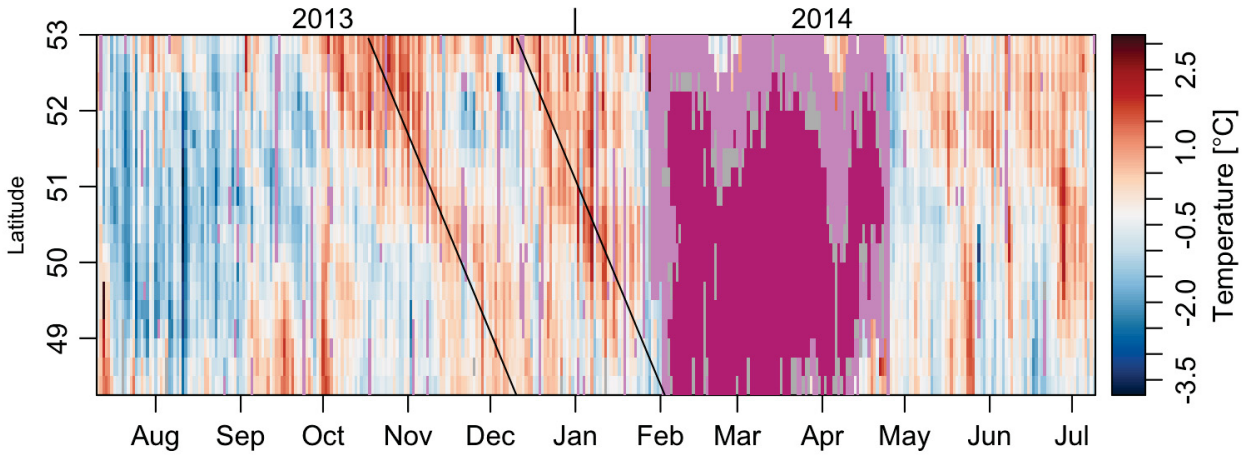

Figure 2.5: Anomaly field for the north-south transect during the mooring sampling period. Note the gap in observations from February to May for the latitude range (48°N to 53°N) chosen. Dark pink indicates missing data due to ice and light pink indicates missing data due to rain. See text for explanation of black parallel lines.

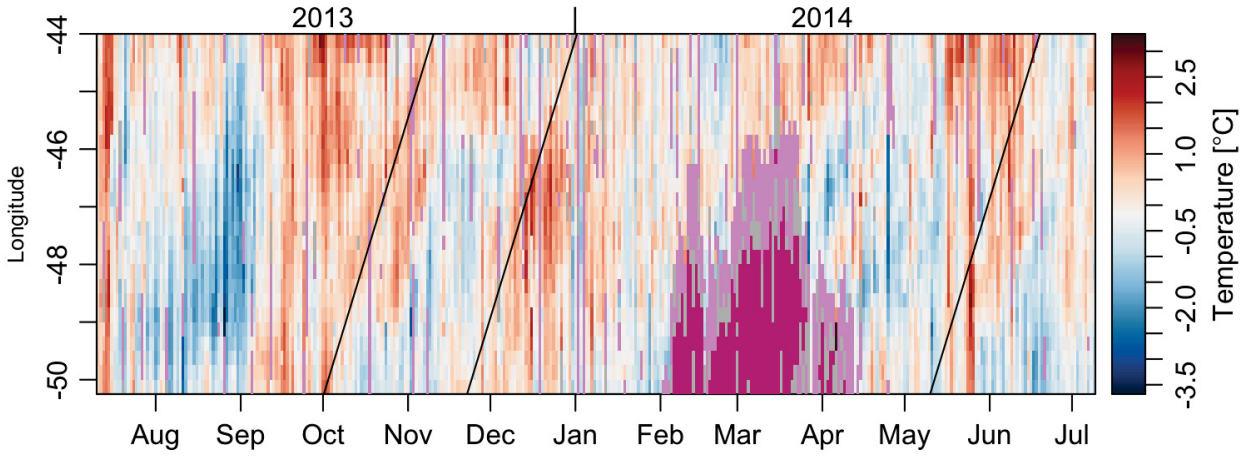

Figure 2.6: As in Figure 2.5, but for the east-west transect. Note the gap from February to March for longitudes west of 46°W. Dark pink indicates missing data due to ice and light pink indicates missing data due to rain. See text for explanation of black parallel lines.

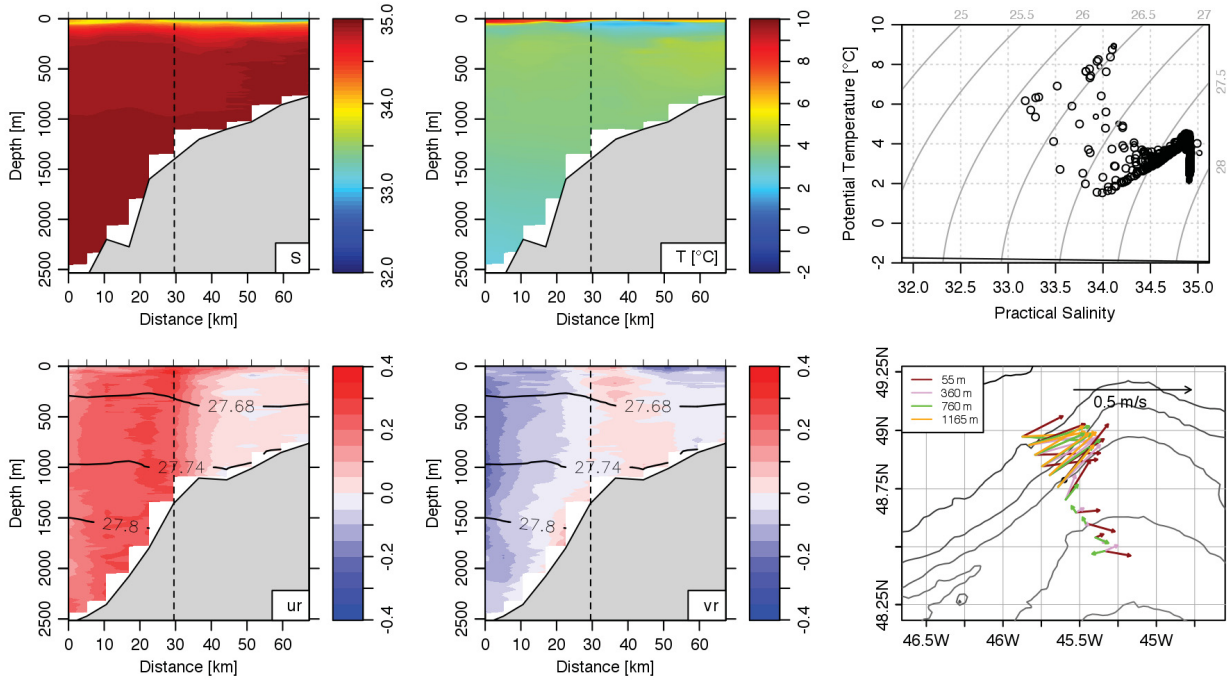

Figure 2.7: Summary of hydrographic properties and velocity for Flemish Cap using CTD and LADCP observations for 2013. The vertical dashed line in section plots is the approximate mooring location. (Top left) Temperature, (top middle) salinity, (top right) temperature-salinity. The horizontal components of velocity (u, v) which have been rotated to the transect line, yielding (u_r, v_r) with (bottom left)$u_r > 0$ indicating flow into the page and (bottom middle) $v_r > 0$ indicating flow right of the page. (Bottom right) Velocity vectors at microCAT depths for the Flemish Cap mooring.

2.3 Flemish Cap

2.3.1 Spatial

2.3.1.1 2013

For the Flemish Cap transect, as shown in Figure 2.7, the upper 170 m are stratified in both salinity and temperature, with an underlying cold layer below the warm stratified layer along the upper slope of Flemish Cap. Below the stratified layer, waters are weakly stratified with increasing salinity, 34.57 to 34.92, and decreasing temperature, (4.5 to 2.3)°C. Signatures of the ULSW range from 265 to 1020 m, and LSW ranges from 1020 to 1600 m. There is easterly intensified flow which extends throughout the water column along the slope, and roughly follows bathymetry, with the exception of the most northerly station, where flow direction is upslope (Figure 2.7).

An estimate of the geostrophic shear can be inferred using hydrographic properties with the

thermal wind equations. The method assumes geostrophic balance (*e.g* of the x-momentum equation),

$$fv = \frac{1}{\rho_0} p_x \tag{2.2}$$

where f is the Coriolis parameter, v is the y-velocity component, ρ_0 is a reference density, taken here as the depth average density, p is pressure, and subscript x is the partial derivative with respect to x. Differentiating Equation (2.2) in the vertical, and assuming a hydrostatic state ($p_z = -\rho g$) yields,

$$v_z = -\frac{g}{f\,\rho_0} \rho_x \tag{2.3}$$

which permits a calculation of the vertical shear of the y-component of velocity. Velocity can be recovered by integrating, *i.e*,

$$v = -\int_{z_0}^{z} v_z dz + v_0 \tag{2.4}$$

where v_0 is the velocity at z_0. If velocity is assumed to vanish at the seafloor, where $z = -H$, then surface velocity can be estimated with

$$v_s = -\int_{-H}^{z} \frac{g}{\rho_0 f} \rho_x dz \tag{2.5}$$

Calculated geostrophic velocity from Equation (2.5) across the transect is summarized in Figure 2.8. This velocity is weak across the transect, and does not capture the vertical and lateral structure of the observed velocity.

2.3.1.2 2014

For the 2014 Flemish Cap transect, Figure 2.9, there were 5 fewer stations than 2013, with those being the shallower stations on the cap. The upper 135 m are stratified in temperature and salinity, but stratification is weaker than 2013. One station suggests a cold fresh layer below the surface layers. Below these surface layers, the salinity and temperature are similar to 2013. Signatures of the ULSW range from 320 to 1270 m, and LSW ranges from 1270 to 1795 m. The easterly intensified flow is weaker than 2013. Velocity suggests, as in 2013, weakened flow farther upslope on the cap. The agreement of the geostrophic velocity and observations appears to be weaker than the 2013 transect, *e.g.* geostrophic velocity is reversed compared to the observations (Figure 2.10). Comparing the depth average velocity from LADCP observations to the geostropic estimates suggests that the the disagreement could be

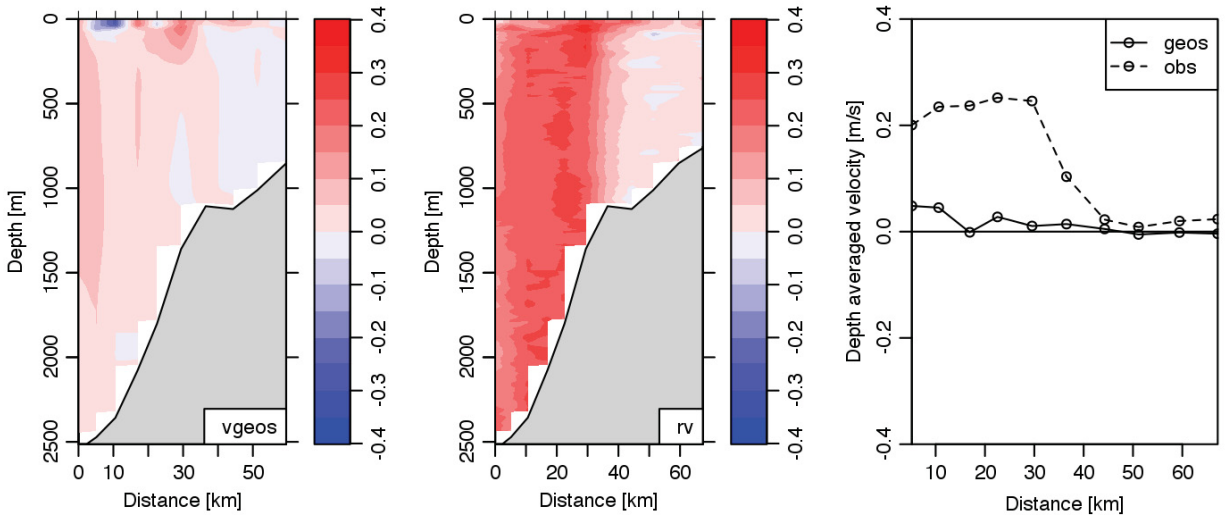

Figure 2.8: Calculated geostropic northward (v) velocity component (left) and LADCP v_r-velocity observations (middle), as well as the depth averaged northward (v) velocity (right) for Flemish Cap 2013 transect.

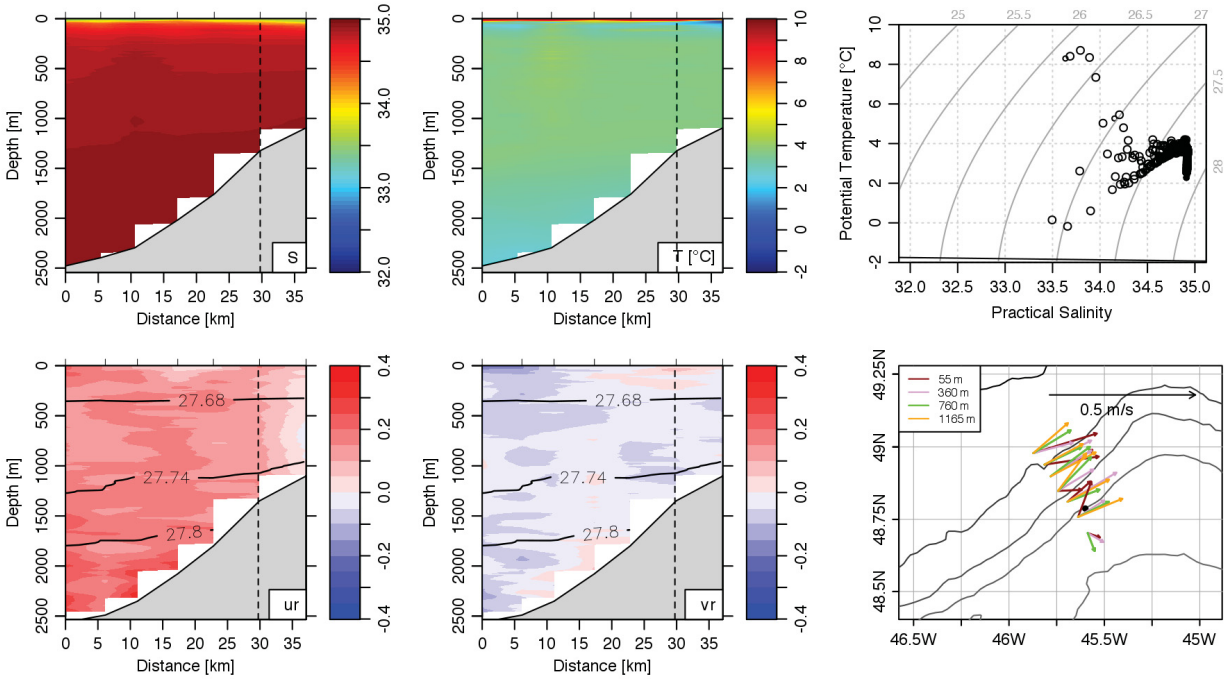

Figure 2.9: As in Figure 2.7, but for Flemish Cap 2014 transect.

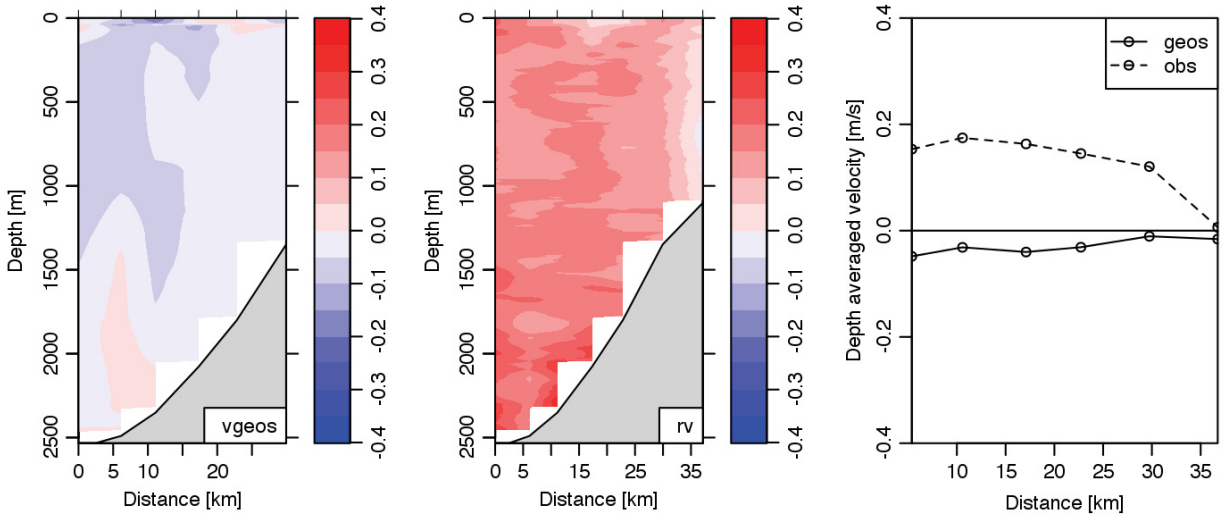

Figure 2.10: As in Figure 2.8, but for Flemish Cap 2014 transect.

due to the bottom boundary condition used in depth-integrating vertical shear in Equation (2.5). LADCP data suggest bottom intensified flow between 0.15 and 0.25m/s. Including bottom velocity in the geostrophic calculation would yield a better agreement between observations. The flat isopycnal lines, Figure 2.9, suggest the flow is barotropic.

2.3.2 Temporal

constituent	period	60 m	185 m	365 m	555 m	760 m	960 m	1165 m	1365 m
SA	365.26 days	x	x	x		x	x	x	
SSA	182.62 days	x	x	x	x	x	x	x	x
MM	27.55 days			x	x	x	x	x	x
M2	12.42 hours			x	x	x	x	x	x
S2	12 hours								x

Table 2.2: Tidal constituents with an amplitude greater than 0.01 m/s for the Northern Flemish Cap mooring.

The time series of the eastward(u) and northward(v) velocity components can be seen in Figures 2.11 and 2.12 respectively. Near-surface velocity varies in direction and magnitude, primarily between November and February, with relatively small low-frequency variation. Below 60 m, flow direction is predominantly towards the northeast. Tidal constituents with an amplitude greater than 0.01 m/s from the u velocity component include solar annual (SA), solar semi-annual (SSA), lunar monthly (MM), principal lunar semi-diurnal (M2), and the principal solar semi-diurnal (S2), which are summarized in Table 2.2.

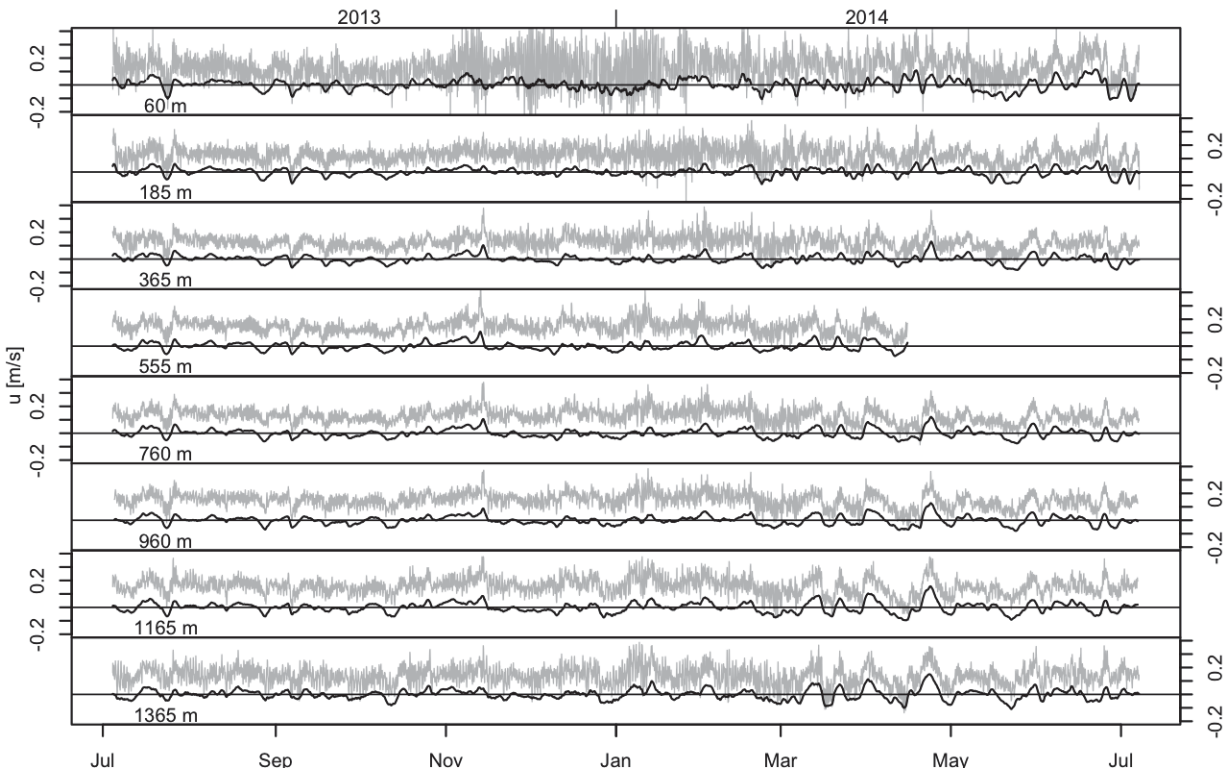

Figure 2.11: Time series of the eastward (u) velocity component for Flemish Cap mooring. Grey line represents the raw data. The black line is the detided then low passed using a first order Butterworth filter with a cutoff period of 4 days.

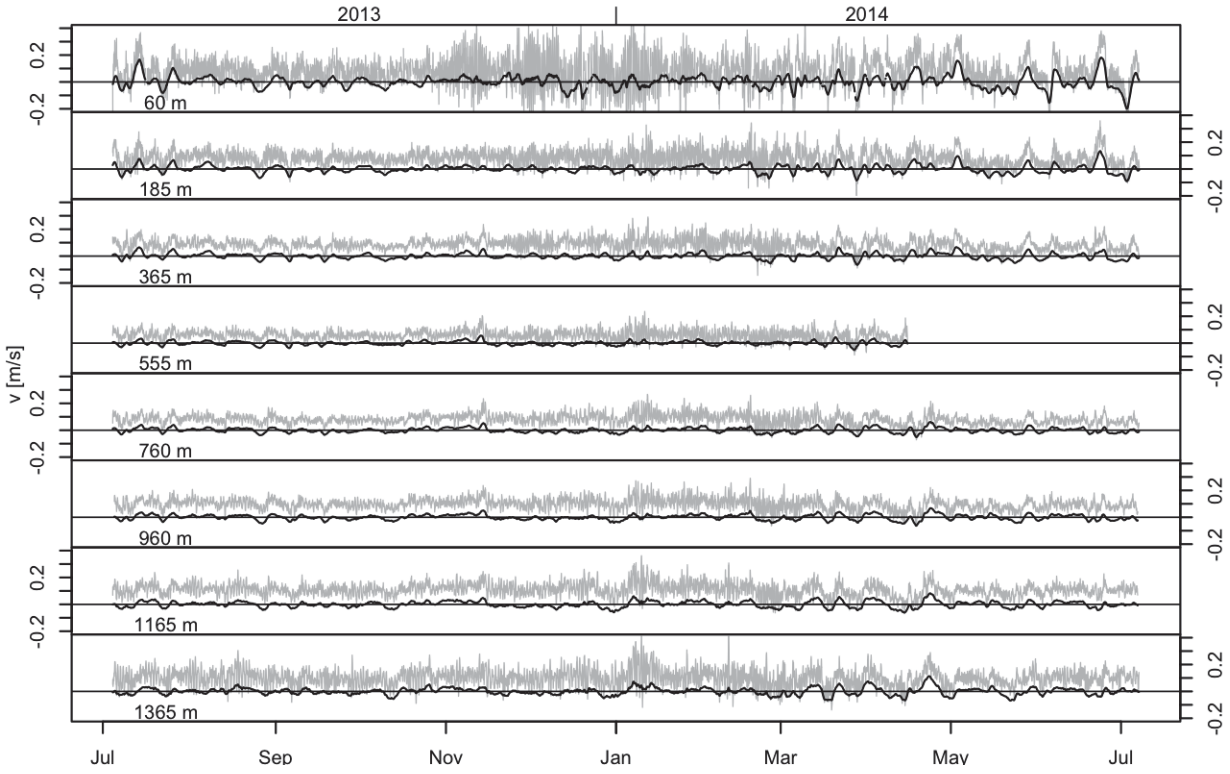

Figure 2.12: As in Figure 2.11, but for the northward (v) velocity component.

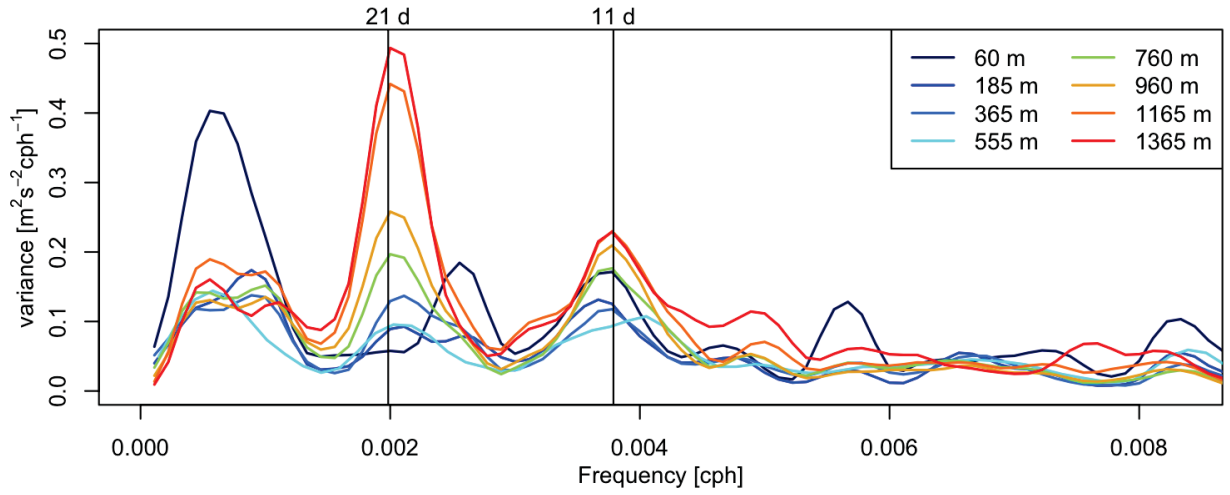

Figure 2.13: Spectrum of speed for Flemish Cap mooring at all microCAT instrument depths. The shallower spectrum are from ADCP data, and the deeper six are from RCM instruments.

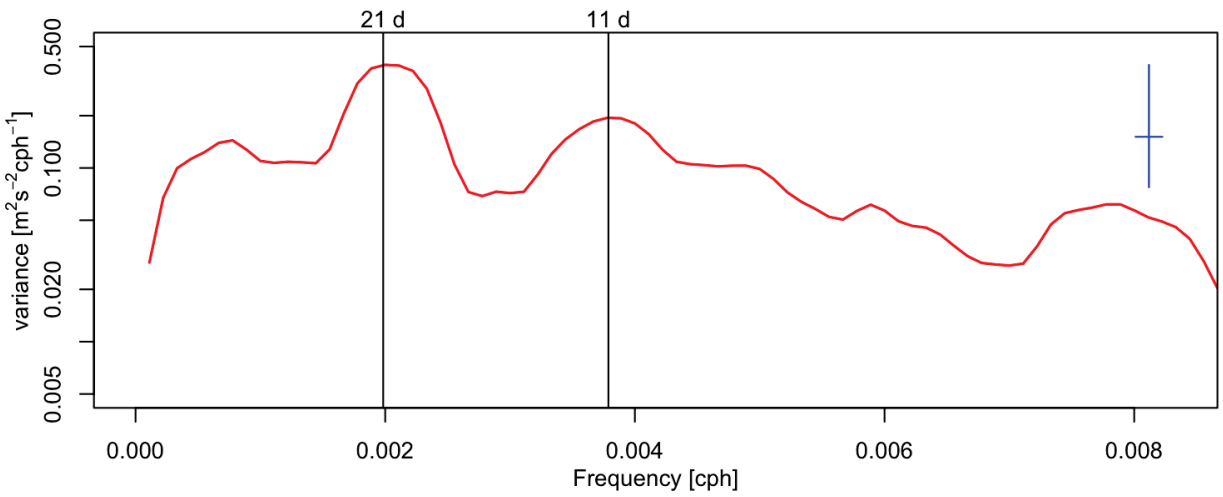

Figure 2.14: Spectrum of speed for the deepest RCM instrument on the Flemish Cap mooring, with the y-axis in *log* space. The blue vertical line indicates the 95% confidence level error bar, an the horizontal blue line is twice the bandwidth.

The detided and low-passed u-velocity, showed in Figure 2.11, indicates a low-frequency signal which increases in magnitude as depth increases (see Appendix B for details on low-passing techniques). The spectrum of the detided speed indicates high power with a peak near 21 days (see Appendix B for details on spectral techniques), as well as another peak around 11 days (Figure 2.13). The spectrum in logarithm space with the error bar is summarized in Figure 2.14, note that the error bar is of the same height for the spectrum at each depth, with the exception of time series of shorter length due to instrument failure.

Some important features of Figure 2.13 are

- The power of the low frequency spectral peak, in general, increases as depth increases.
- There is a peak at a lower frequency at 60 m around 75 days.
- The detided and low-passed time series, Figure 2.11, and the spectrum of the speed, Figure 2.13, suggests that there could be vertical coherency.

The coherency and phase between adjacent mooring instruments were calculated. The coherency indicates whether two signals are similar in frequency space. Near the 3-week spectral peak, the coherency between the de-tided speed for adjacent instruments was calculated (Figure 2.15). The coherency found was between adjacent instruments, for *e.g* the coherency between 60 m and 185 m is indicated at 60 m in Figure 2.15 . At the 3-week spectral peak, velocity is coherent below 365 m. The phase, Φ, below 365 m ranges from -0.45

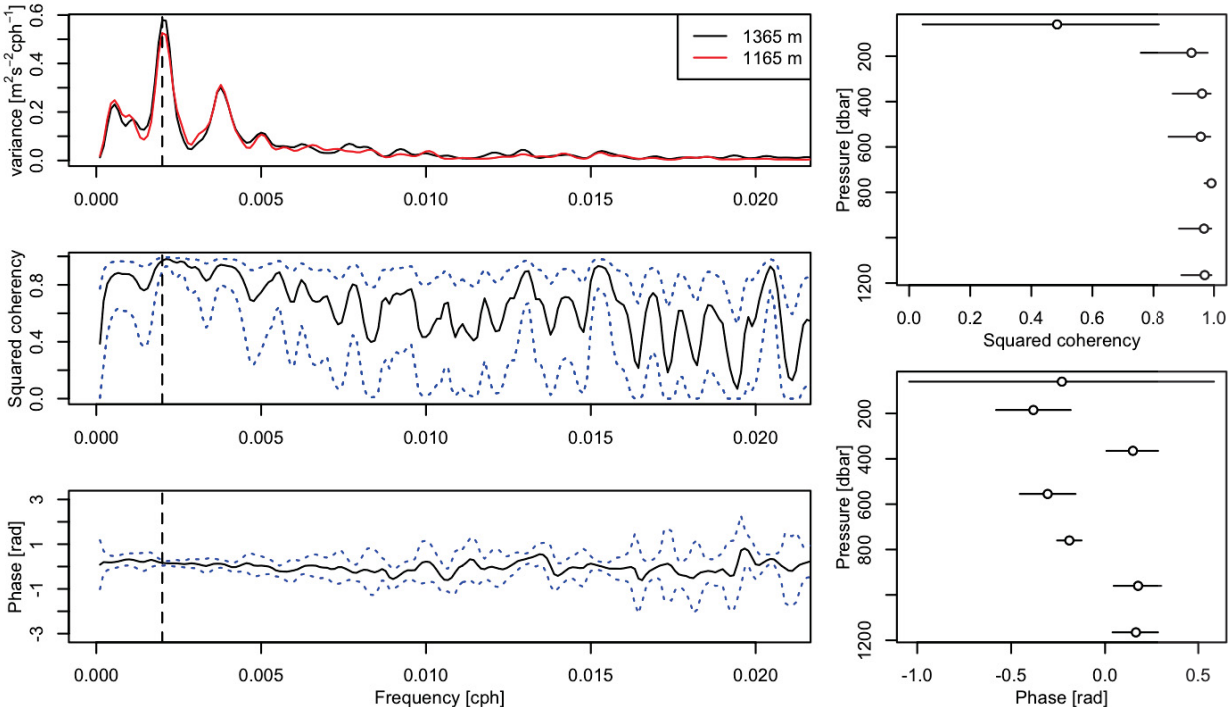

Figure 2.15: Spectrum, squared coherence, and phase for Flemish Cap. (Top left) Spectrum of two deepest instruments. (Middle left) Squared coherency with uncertainty indicated by dashed blue lines. (Bottom left) Phase with uncertainty indicated by dashed blue lines. (Top right) Vertical squared coherency at period 20.83 days between adjacent instruments. (Bottom right) Phase at the same period as squared coherency.

Depth (m)	$\bar{u}$ (m/s)	sd (m/s)	$\bar{v}$ (m/s)	sd (m/s)	$\overline{U}$ (m/s)	$\overline{T}$ (°C)	sd (°C)	$\overline{S}$	sd
55	0.13	0.05	0.09	0.04	0.16	3.41	1.23	34.35	0.2
210	0.15	0.05	0.06	0.03	0.16	3.85	0.45	34.79	0.08
360	0.13	0.05	0.08	0.04	0.16	4.09	0.27	34.87	0.04
560	0.15	0.06	0.1	0.04	0.18	3.97	0.18	34.89	0.02
760	0.16	0.06	0.11	0.05	0.2	3.82	0.1	34.89	0.01
960	0.14	0.07	0.1	0.06	0.18	3.76	0.04	34.89	0.01
1165	0.13	0.1	0.08	0.11	0.19	3.71	0.04	34.91	0
1365	0.13	0.06	0.08	0.06	0.16	3.63	0.07	34.92	0

Table 2.3: Flemish Cap moorings statistics from the RCM and ADCP unfiltered hourly observations and microCAT unfiltered 5 minute observations. $\overline{u}$, $\overline{v}$ are the mean horizontal velocity components, sd indicates standard deviation, $\overline{U}$ is mean speed, $\overline{T}$ is the mean temperature, and $\overline{S}$ is the mean salinity.

to 0.3 radians. The phase can be converted to a time lag, $t_0 = -\Phi/\omega$, with the result being a lag from -6.2 to 9.4 days.

In mid-October, the near-surface temperature increases, Figure 2.16. SST suggests a transition from warmer to cooler waters as indicated in Figure 2.4. The CTD transect data, Figure 2.7 and 2.9, suggests a surface layer roughly 135-170 m thick. Between 210 to 760 m, temperature has an increasing trend from July to March, and there is a cooling trend between March and May, where temperatures returns to roughly the same temperature at the beginning of the sampling period. Below 760 m, temperatures have small excursions about the mean value. The maximum mean temperature is at 360 m, which is consistent with the subsurface temperature maximum as suggested by the CTD profiles, which is within the ULSW depth range. Low-passed temperature fluctuations below 360 m appear to be in agreement with each other from mid March to the end of the sampling period.

The near-surface salinity decreases during the temperature increase during mid-October, Figure 2.17, suggesting that a strong mixing event occurred, as less saline waters are near the surface, as depicted in the CTD transects, Figure 2.7 and 2.9. Temperature events from March to May between depths 210 to 560 m are also apparent in salinity, Figure 2.17. Below 560 m, salinity has small excursions about the mean.

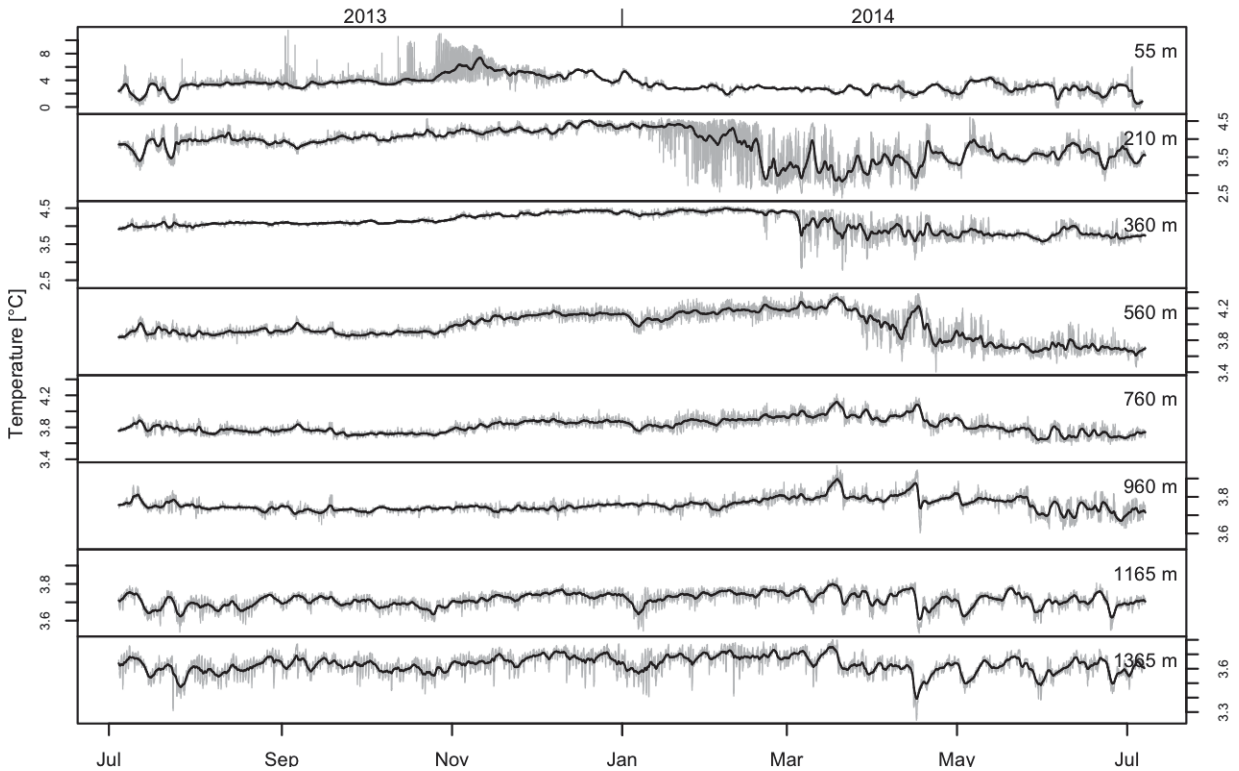

Figure 2.16: Low-passed temperature for Flemish Cap. Note the change in the axis limits between depths.

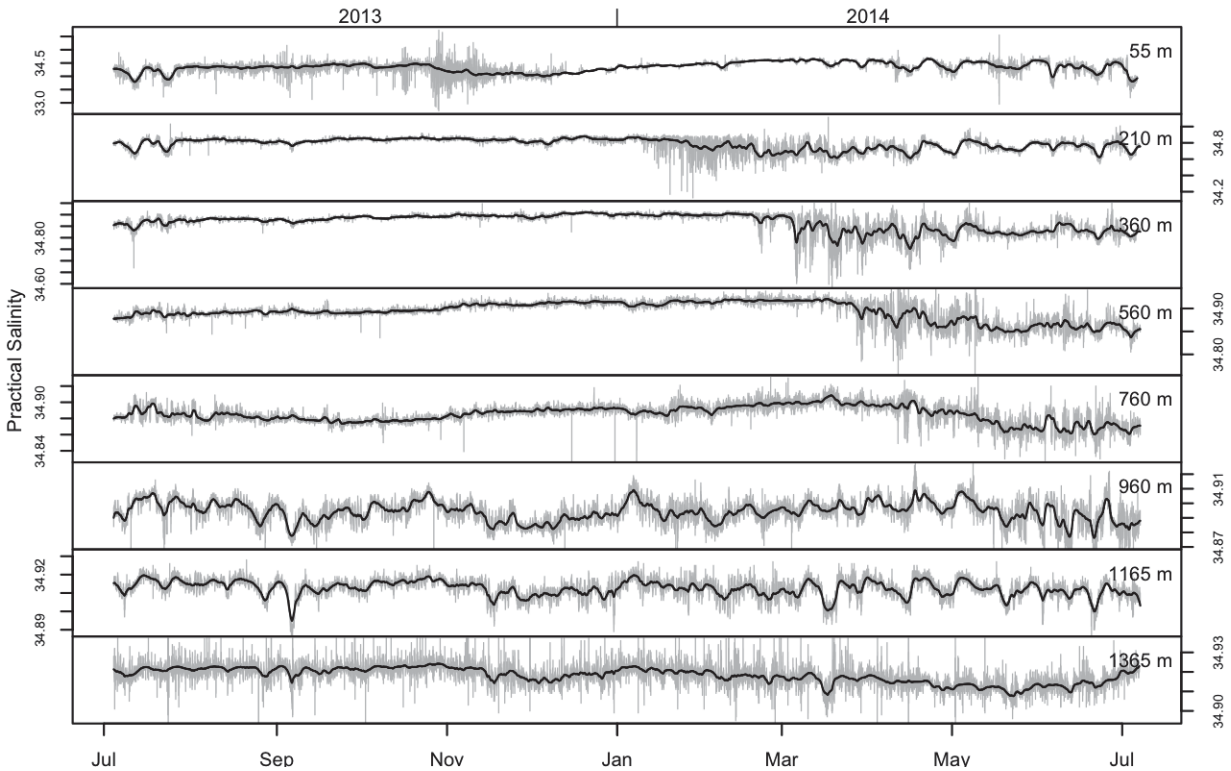

Figure 2.17: As in Figure 2.16, but for salinity, note the change in the axis limits between depths.

2.4 Sackville Spur

2.4.1 Spatial

2.4.1.1 2013

For the Sackville Spur 2013 transect, Figure 2.18, the water column is stratified in temperature and salinity in the top 225 m, with a layer of cold water below the warmer and fresher surface layer. Below 225 m, waters are weakly stratified, primarily in salinity. Signatures of ULSW range from 270 to 1190 m, and LSW north of Sackville Spur reaching from 1190–1805 m. North of Sackville Spur, there is intensified northeast flow which follows bathymetry. Velocity over the spur is weak with flow transitioning from northeast to northwest. Along the western slope of Flemish Pass, flow is surface intensified (Figure 2.18). Along the slope of Flemish Cap, the measurements suggest northeast flow, consistent with topographically generated Taylor column flow as suggested by *Colbourne and Foote* (2000). The vertical and lateral structure of the geostrophic velocity is in reasonable agreement with the observations with surface intensified flow following bathymetry contours north of Sackville Spur, and southward flow within Flemish Pass (Figure 2.19).

2.4.1.2 2014

Figure 2.20 indicates hydrographic and velocity properties at Sackville Spur in 2014. Waters in the top 240 m are stratified in salinity and temperature with a thicker lens of cold water about the bathymetric contours of Sackville Spur. Signatures of ULSW ranges from 265 to 1120 m and LSW is prominent north of Sackville Spur ranging from 1120 to 1740 m. Velocity characteristics are similar to the 2013 transect. There is a surface-intensified northeast current to the north of the spur, and a southwest surface-intensified current along the thalweg of Flemish Pass, where currents are relatively strong throughout the water column (Figure 2.20). Note that the position of the surface intensified flow within the pass is different than in 2013. Similar to the 2013 transect, the lateral and vertical structure of the geostrophic velocity reflects the observations (Figure 2.21).

2.4.2 Temporal

The time series of both velocity components for Sackville Spur can be seen in Figure 2.22 and 2.23. Near-surface velocity varies in magnitude, primarily between November and March, and direction, northeast to southeast. After detiding and low passing the v-velocity

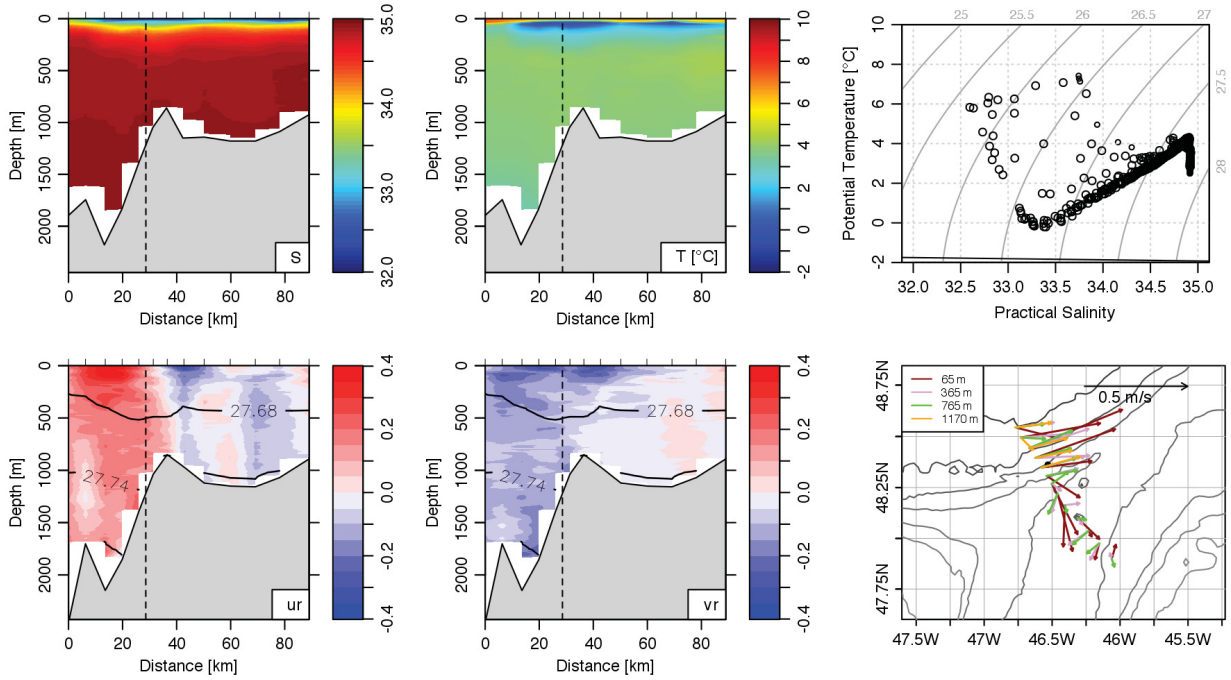

Figure 2.18: Summary of hydrographic properties and velocity for Sackville Spur using CTD and LADCP observations for 2013. The vertical dashed line in section plots is the approximate mooring location. (Top left) Temperature, (top middle) salinity, (top right) temperature-salinity. The horizontal components of velocity (u, v) which have been rotated to the transect line, yielding (u_r, v_r) with (bottom left)$u_r > 0$ indicating flow into the page and (bottom middle) $v_r > 0$ indicating flow right of the page. (Bottom right) Velocity vectors at microCAT depths for the Sackville Spur mooring.

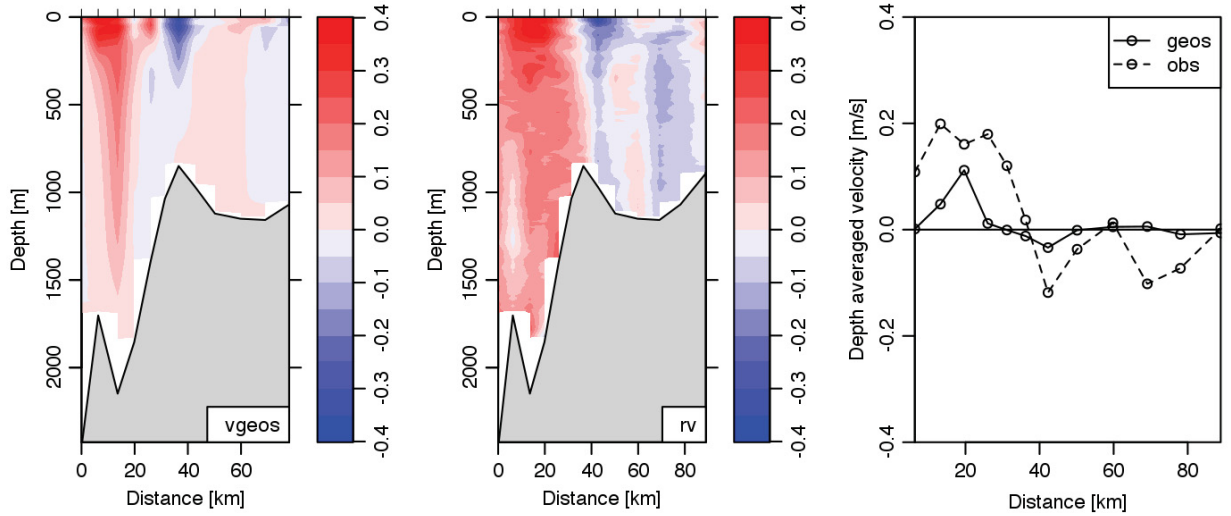

Figure 2.19: Calculated geostropic northward velocity component (left) and LADCP v_r-velocity observations (middle), as well as the depth averaged northward velocity (right) for Sackville Spur 2013 transect.

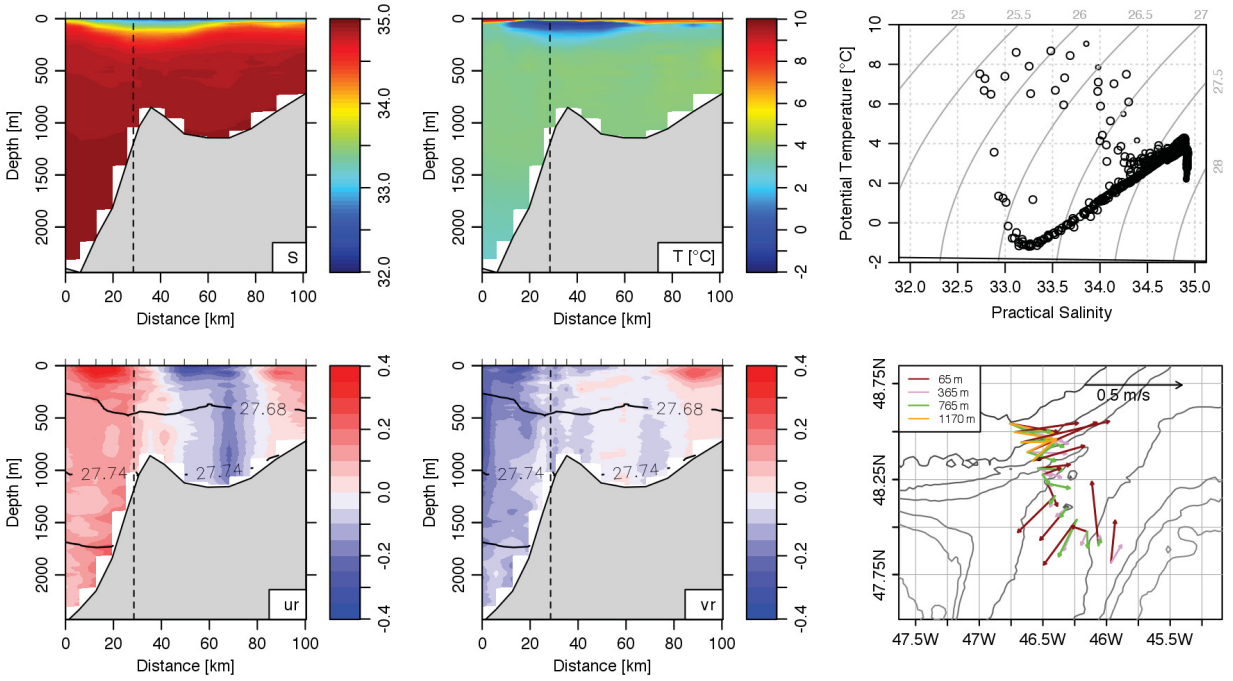

Figure 2.20: As in Figure 2.18, but for Sackville Spur 2014 transect.

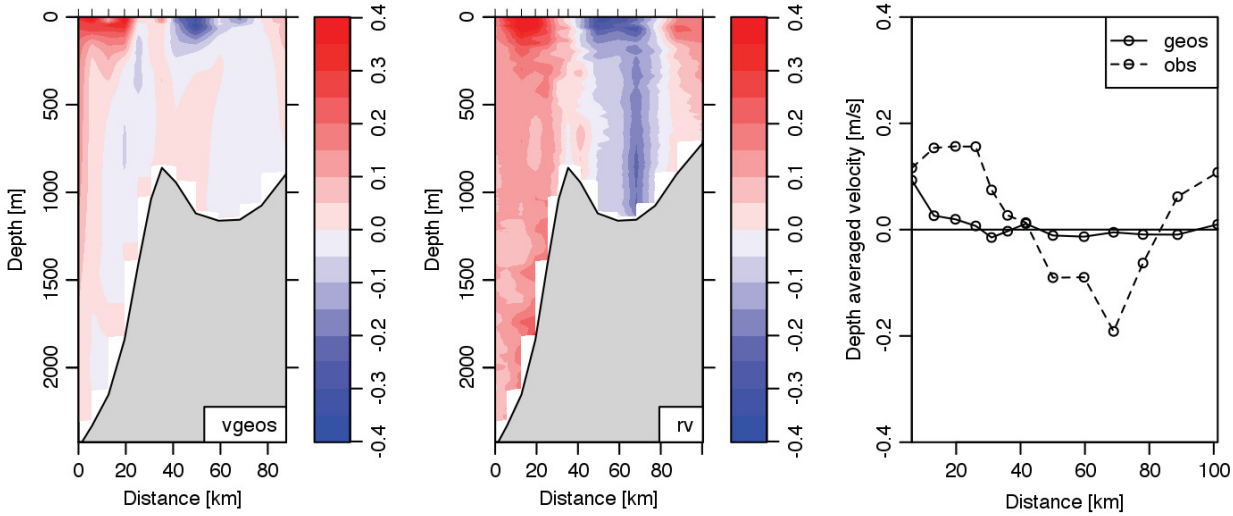

Figure 2.21: As in Figure 2.19, but for Sackville Spur 2014 transect.

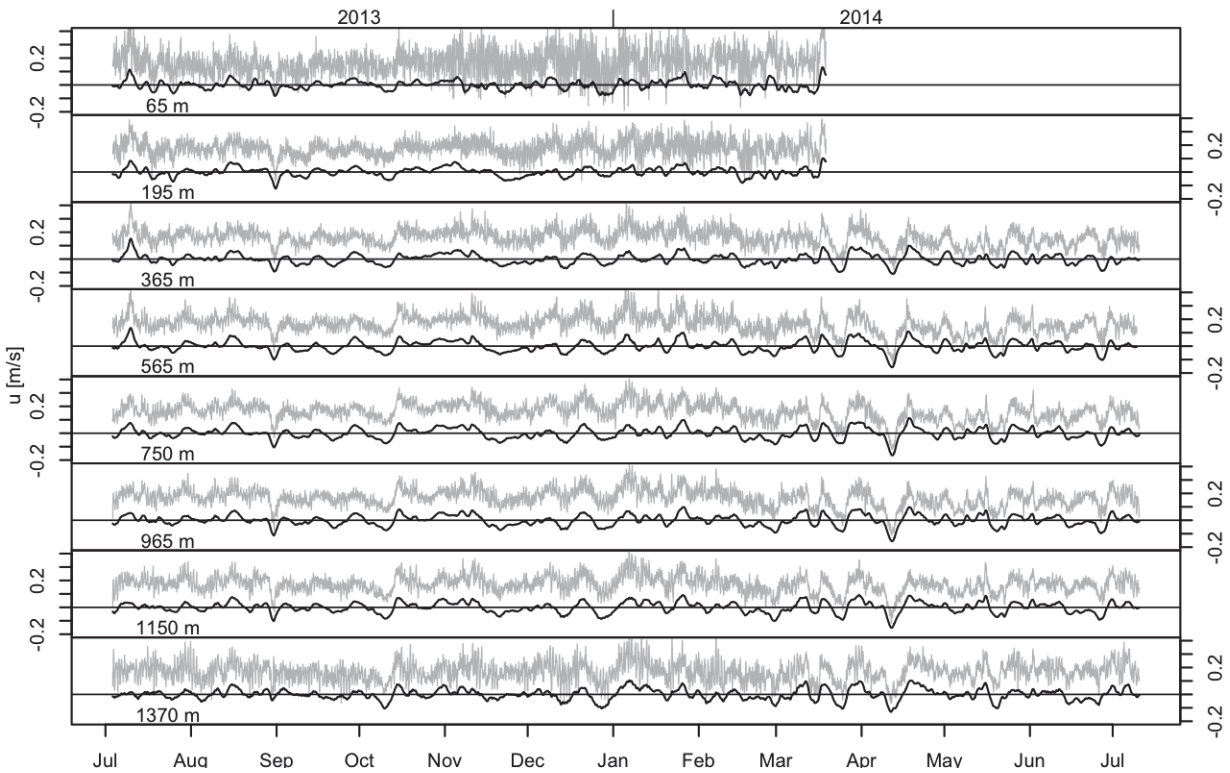

Figure 2.22: Time series of the u-velocity component for Sackville Spur mooring.Grey line represents the raw data. The black line is the detided then low passed using a first order Butterworth filter with a cutoff period of 4 days.

component, the low frequency variation is weak compared with the u-velocity component. Tidal constituents with an amplitude greater than 0.01 m/s calculated from the u velocity component include solar annual (SA), solar semi-annual (SSA), solar monthly (MSM), lunar monthly (MM), lunar solar fortnightly (MF), principal lunar semi-diurnal (M2), and H2 [3]. The dominant tidal constituents for each depth is summarized in Table 2.4. Throughout the water column, velocity magnitude increases as depth increases. Similar to the Flemish Cap mooring, the detided and low passed velocity components suggest low frequency variability between March and May for the moored instruments below 365 m.

constituent	period	65 m	195 m	365 m	565 m	750 m	965 m	1150 m	1370 m
SA	365.26 days	x	x	x	x	x	x	x	x
SSA	182.62 days	x							
MSM	31.81 days	x	x	x	x	x	x	x	x
MM	27.55 days	x	x	x	x	x	x	x	
MF	13.66 days	x	x	x		x	x	x	
M2	12.42 hours			x	x	x	x	x	
H2	12.4 hours				x				

Table 2.4: Tidal constituents with an amplitude greater than 0.01 m/s for the Sackville Spur mooring.

The variance preserving spectrum at each depth indicates, as in the Flemish Cap mooring, high power with a maximum at 21 days for instruments located between 565 m to 1370 m, as well as a second peak with a maximum around 13.5 days (Figure 2.24). Importantly, for the next chapter of this thesis, the power for both peaks increases as depth increases.

The coherency and phase between adjacent instruments at the spectral peak maximum of 21 days was found (Figure 2.25). The coherency between 65 m 195 m as well as 195 m and 365 m, indicates lower coherency with high uncertainty. There is high coherency with a small uncertainty for measurements at and below 565 m. The phase at and below 565 m ranges between -0.277 to 0.291 radians, converting into time, this corresponds to 5.8 to -6.1 days respectively.

The near-surface hydrographic properties are, on average, colder and fresher than underlying waters, Figure 2.26. This could be attributed to the cold waters suggested in the CTD transects (Figure 2.18 and 2.20). Akin to the Flemish Cap mooring, there is a sub-surface temperature maximum at 365 m. Similar to the events found during November in the near surface

[3]Personal communication with Shannon Nudds at Bedford Institute of Oceanography led to an exchange of e-mails with Mike Foreman, which determined that the H2 tidal constituent has never been formally named.

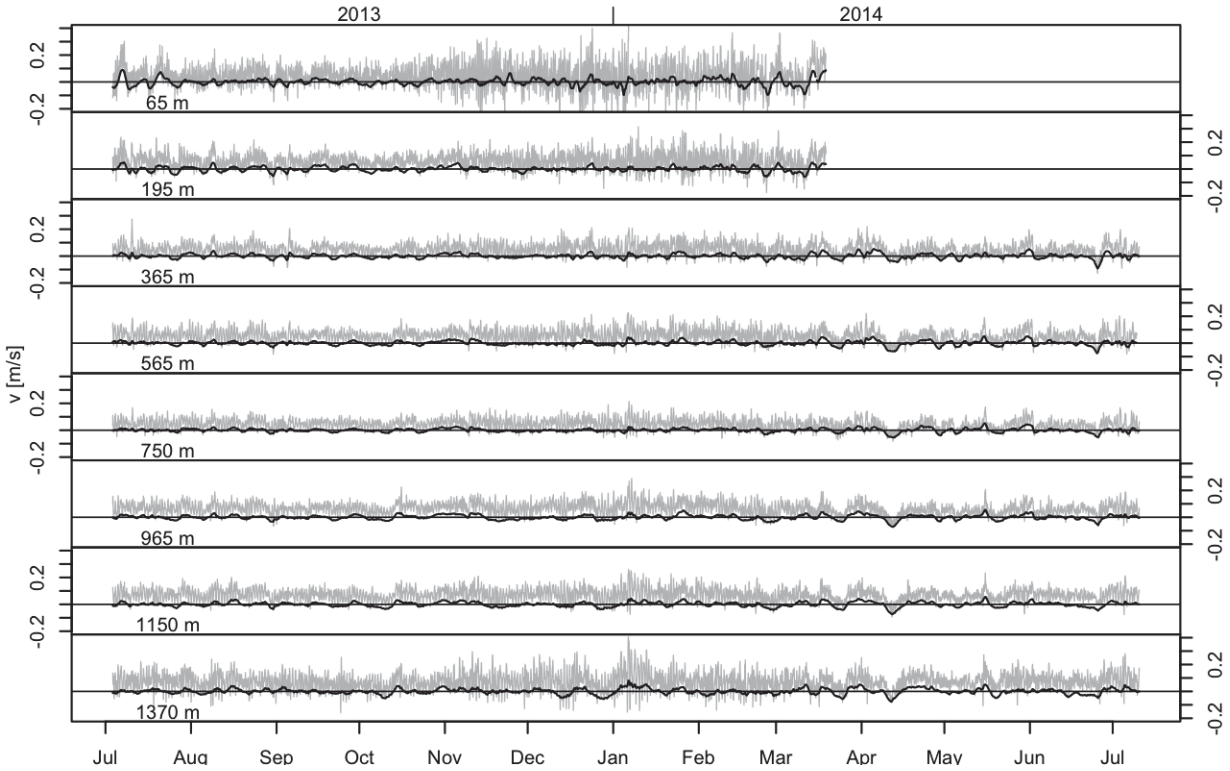

Figure 2.23: As in Figure 2.22, but for the northward velocity component.

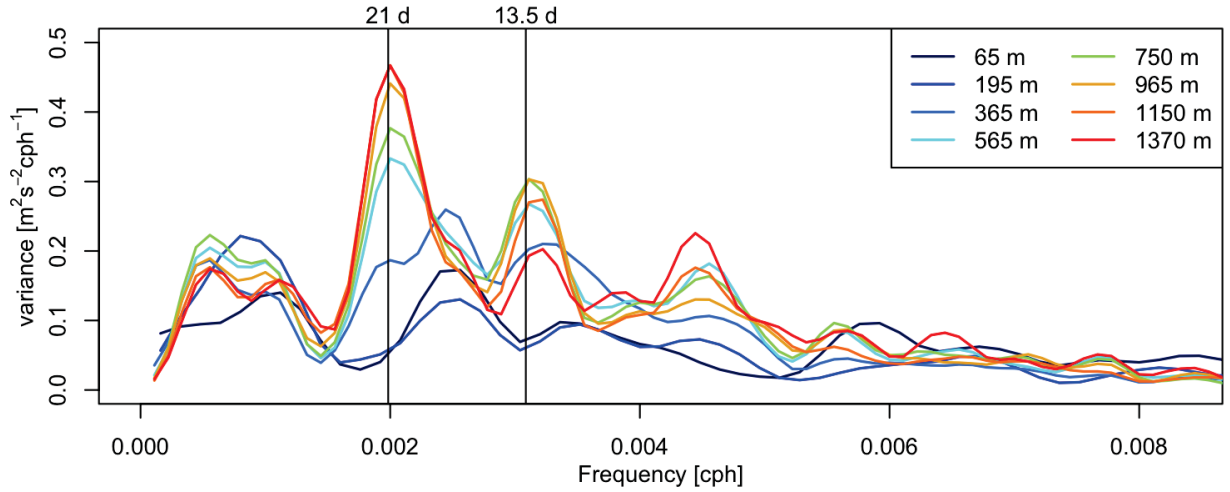

Figure 2.24: Spectrum of speed for Sackville Spur mooring at all microCAT instrument depths. The shallower spectrum are from ADCP data, and the deeper six are from RCM instruments.

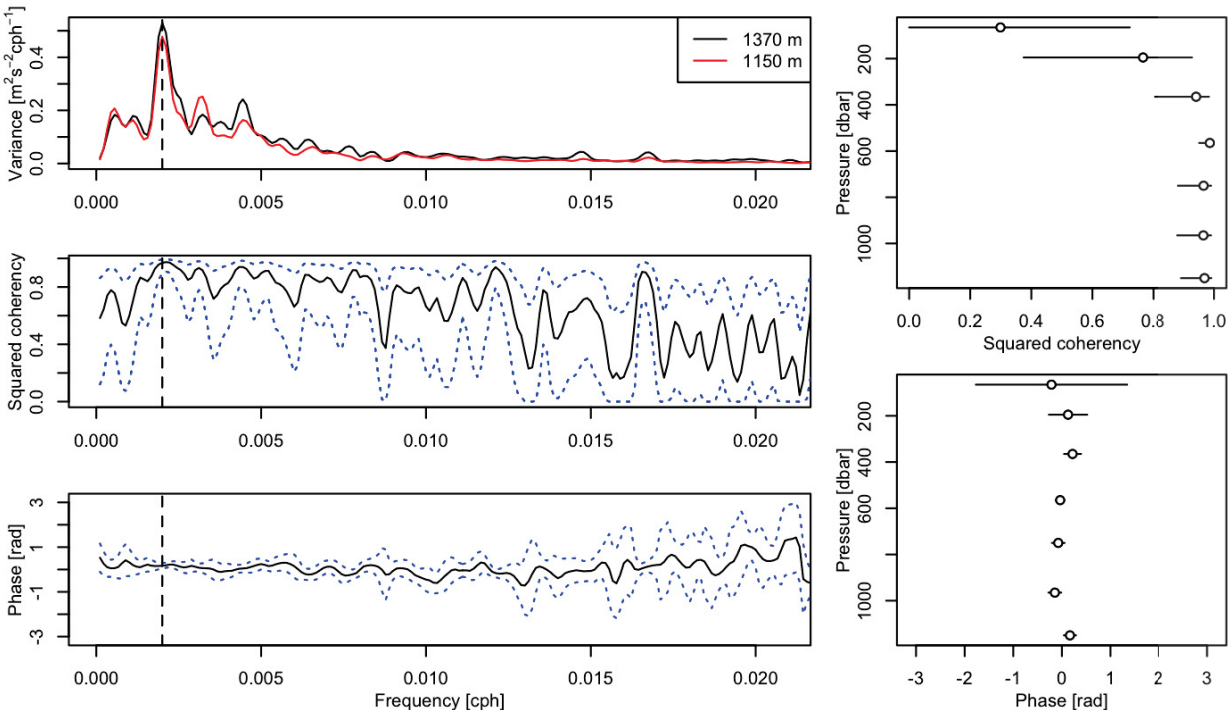

Figure 2.25: Spectrum, squared coherence, and phase for Sackville Spur. (Top left) Spectrum of two deepest instruments. (Middle left) Squared coherency with uncertainty indicated by dashed blue lines. (Bottom left) Phase with uncertainty indicated by dashed blue lines. (Top right) Vertical squared coherency at period 20.83 days between adjacent instruments. (Bottom right) Phase at the same period as squared coherency.

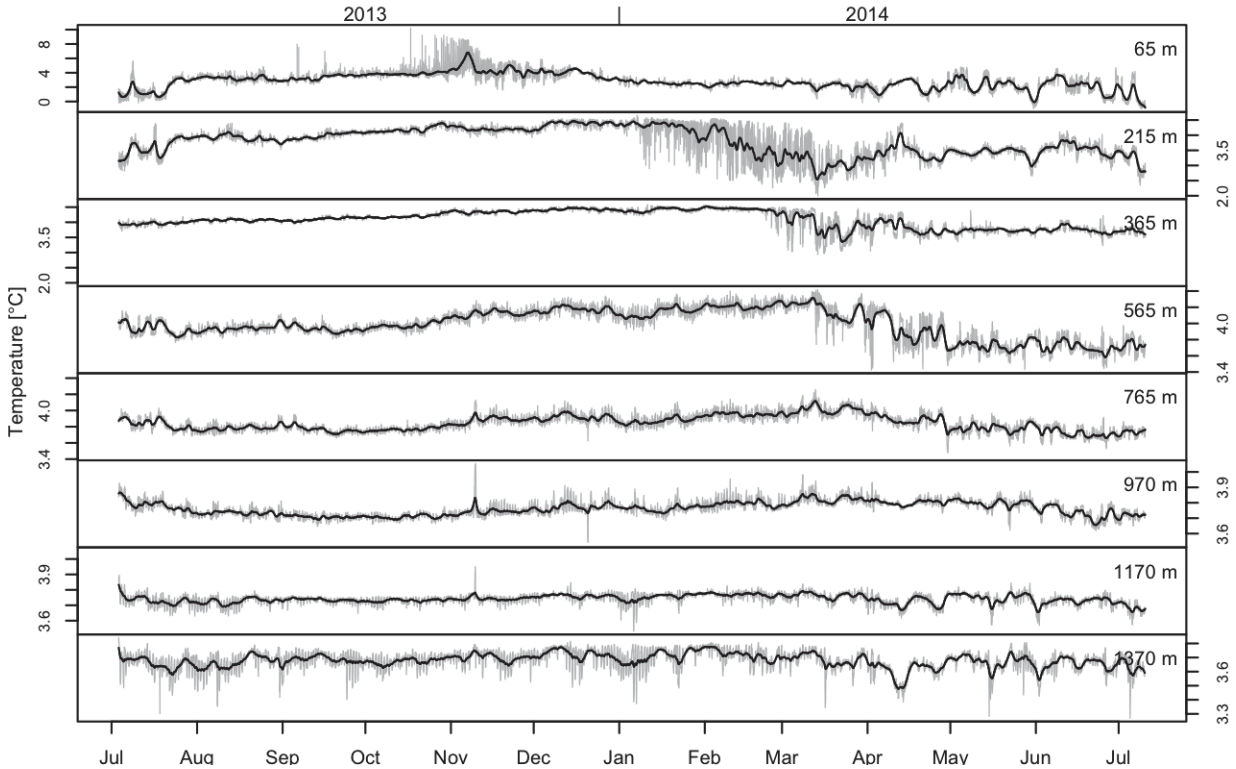

Figure 2.26: Low-passed temperature for Sackville Spur at each instrument depth.

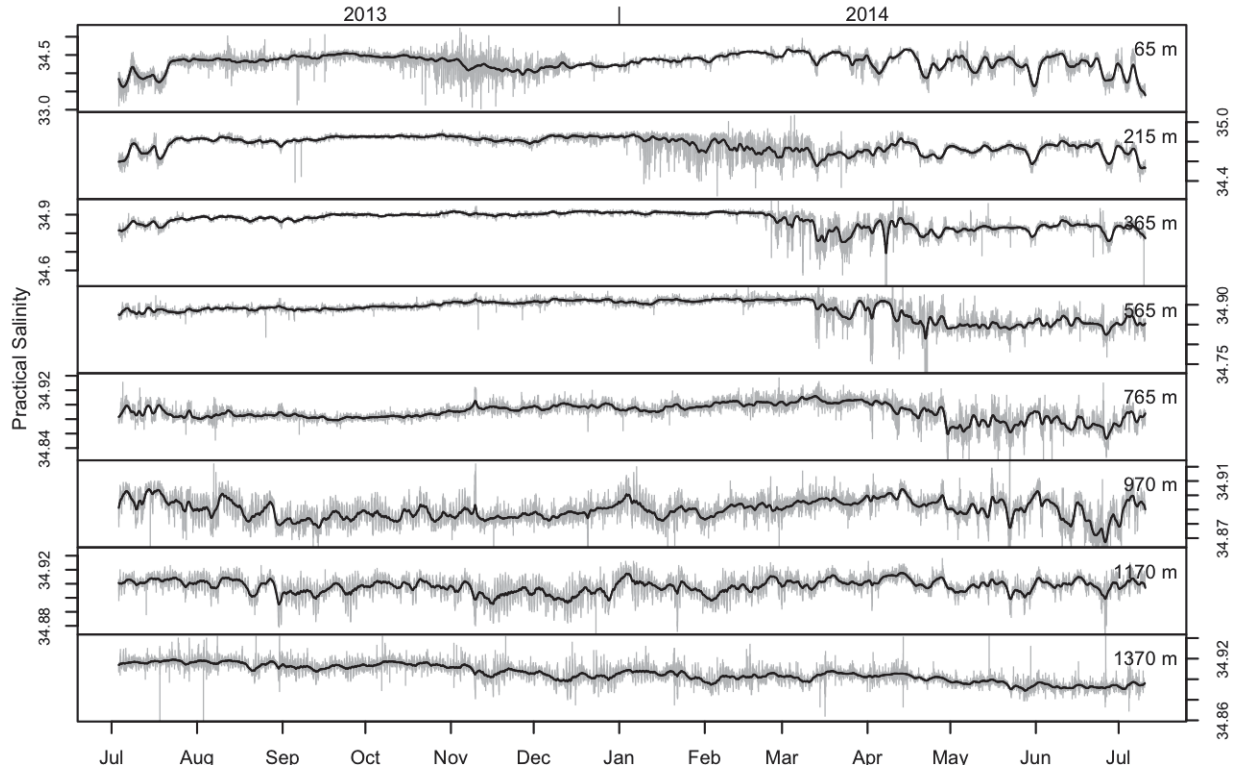

Figure 2.27: As in Figure 2.26, but for salinity.

Depth (m)	$\bar{u}$ (m/s)	sd (m/s)	$\bar{v}$ (m/s)	sd (m/s)	$\overline{U}$ (m/s)	$\overline{T}$ (°C)	sd (°C)	$\overline{S}$	sd
65	0.16	0.06	0.05	0.04	0.18	2.83	1.19	34.3	0.24
215	0.17	0.07	0.06	0.04	0.18	3.8	0.49	34.77	0.09
365	0.16	0.07	0.05	0.04	0.18	4.08	0.3	34.87	0.05
565	0.17	0.07	0.07	0.04	0.19	3.99	0.19	34.89	0.03
765	0.17	0.06	0.07	0.04	0.19	3.84	0.1	34.89	0.01
970	0.17	0.07	0.07	0.06	0.19	3.76	0.05	34.89	0.01
1170	0.17	0.09	0.05	0.09	0.19	3.74	0.03	34.91	0.01
1370	0.18	0.06	0.06	0.05	0.2	3.68	0.07	34.91	0.01

Table 2.5: Sackville Spur moorings statistics from the RCM and ADCP unfiltered hourly observations and microCAT unfiltered 5 minute observations. $\overline{u}$, $\overline{v}$ are the mean horizontal velocity components, sd indicates standard deviation, $\overline{U}$ is mean speed, $\overline{T}$ is the mean temperature, and $\overline{S}$ is the mean salinity.

observations in temperature and salinity at the Flemish Cap site, they are also present at the Sackville Spur location. Also, the decreased temperature and varying salinity between January and March is also apparent at 215 m.

2.5 Flemish Pass

2.5.1 Spatial

2.5.1.1 2013

In order to summarize properties of the near surface, intermediate, and the deep waters, the CTD data for each transect is clustered using the k-means method using the algorithm of *Hartigan and Wong* (1979), where the observations are partitioned into k number of groups such that the sum of the squares about the cluster centre point is minimized (*R Core Team*, 2015). For the cluster analysis, any number of variables can be indicated to be clustered against, as well as the number of clusters.

For the transect CTD data, the data are clustered against σ_θ, spice (π), and longitude. The variables were chosen based on *a-priori* information about the water properties. For watermass clustering, the variables need to have break-points in order to suggest and obtain meaningful clusters. Although experiments were done with clustering in T-S space, it was decided to use $\sigma_\theta - \pi$ space because in some sense they are dynamically independent (see *e.g Flament* (2002)). Waters characterized to have high spiciness are relatively warmer and saltier than waters which are less spicy. Spice can also be interpreted as the distance orthogonal to

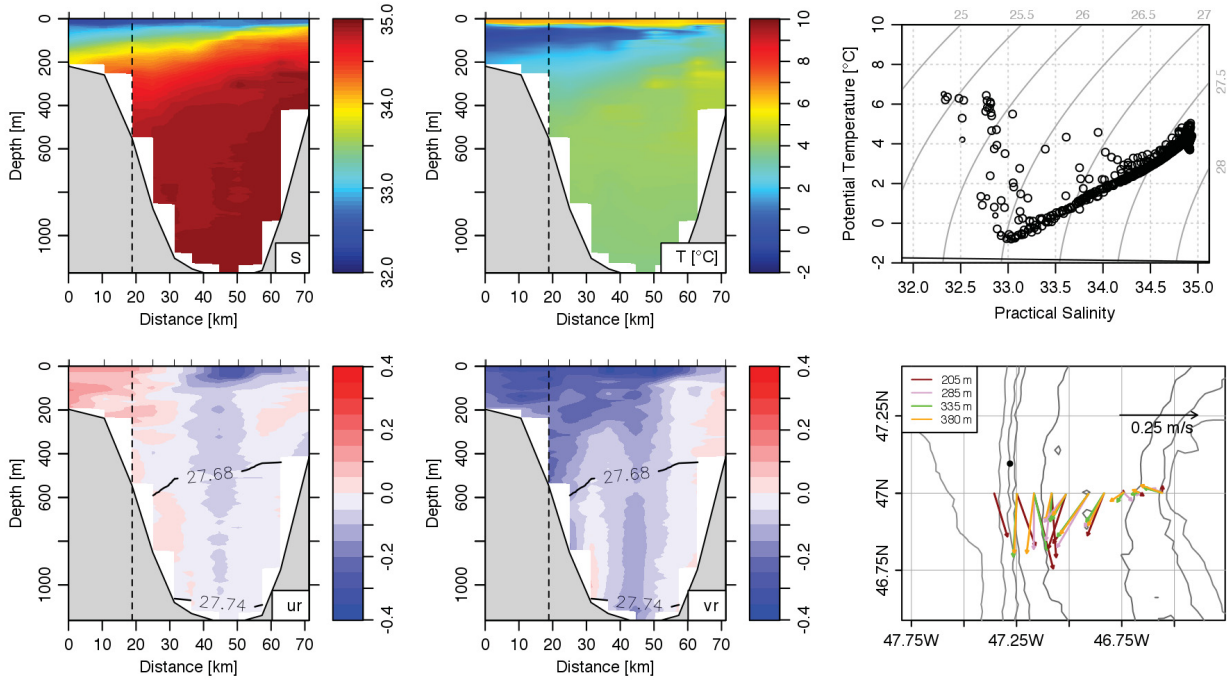

Figure 2.28: Summary of hydrographic properties and velocity for Flemish Pass using CTD and LADCP observations for 2013. The vertical dashed line in section plots is the approximate mooring location. (Top left) Temperature, (top middle) salinity, (top right) temperature-salinity. The horizontal components of velocity (u, v) which have been rotated to the transect line, yielding (u_r, v_r) with (bottom left)$u_r > 0$ indicating flow into the page and (bottom middle) $v_r > 0$ indicating flow right of the page. (Bottom right) Velocity vectors at selected ADCP depths from the Flemish Pass mooring.

isopycnals lines on a T-S diagram (*Flament*, 2002). The orthogonality of σ_θ and spice proved to be successful for clustering water masses in TS-space. Since σ_θ and spice were closely related, adding longitude allowed to observe if there is a spatial difference across transects for 4 clusters.

In the Flemish Pass, the upper 215 m are stratified in salinity and temperature with a warm fresh layer relative to underlying waters in approximately the top 50 m with a salinity range of 32.31 to 33.62, and a temperature range of (0.8 to 6.9)°C (Figure 2.28 and 2.29). Below the surface layers, there is a cold intermediate layer between 25 and 215 m, with a temperature range of (-0.9 to 4)°C, and salinity range of 32.67 to 34.23. The depth and horizontal extent of the cold intermediate layer varies longitudinally within the pass, with a prominent intermediate layer on the western side of the pass, and a much less obvious layer on the eastern side of the pass (Figure 2.29). There are also longitudinally-varying deep watermass

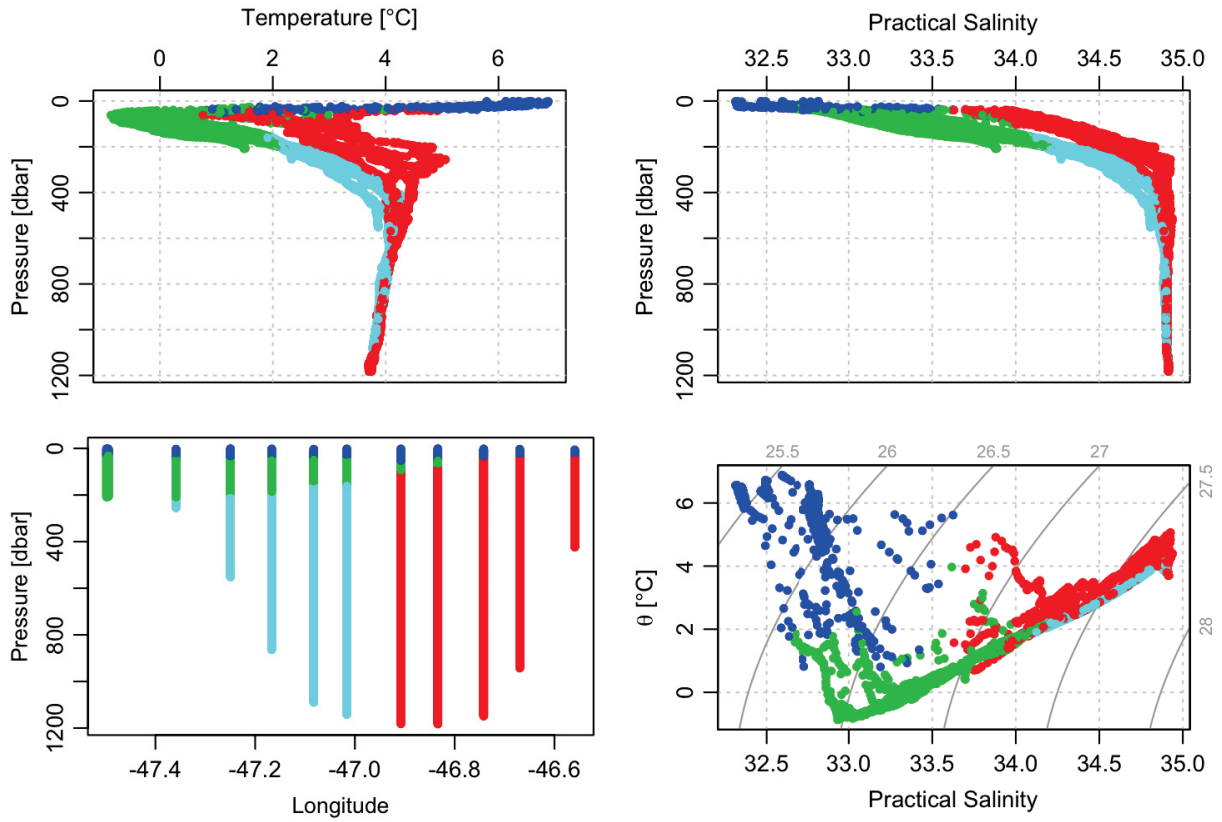

Figure 2.29: Cluster analysis of Flemish Pass transect. The data is clustered using the k-means method using the algorithm of *Hartigan and Wong* (1979), where the observations are partitioned into k number of groups such that the sum of the squares about the cluster centre point is minimized (*R Core Team*, 2015).

properties. Deeper waters (265 to 1020 m) are consistent with ULSW properties. As in the Sackville Spur transect, along the western side of Flemish Pass, the survey measurements suggest weak northeast flow (Figure 2.28). There is surface-intensified southwestward flow near the thalweg, and surface-intensified southeastward flow on the western side of Flemish Pass (Figure 2.28). Along the western side of Flemish Pass, there is northeastward flow, consistent with topographically generated Taylor column flow as suggested by *Colbourne and Foote* (2000).

The geostropic v-velocity component was calculated using Equation (2.5) and is compared to observations in Figure 2.30. The vertical structure of the geostropic velocity captures the surface-intensified signature, as well as reversed flow along the cap. Deep velocity structure tends to differ due to the assumption of zero flow at the seafloor. Based on the general agreement in vertical structure across the transect, as well as the depth averaged velocity,

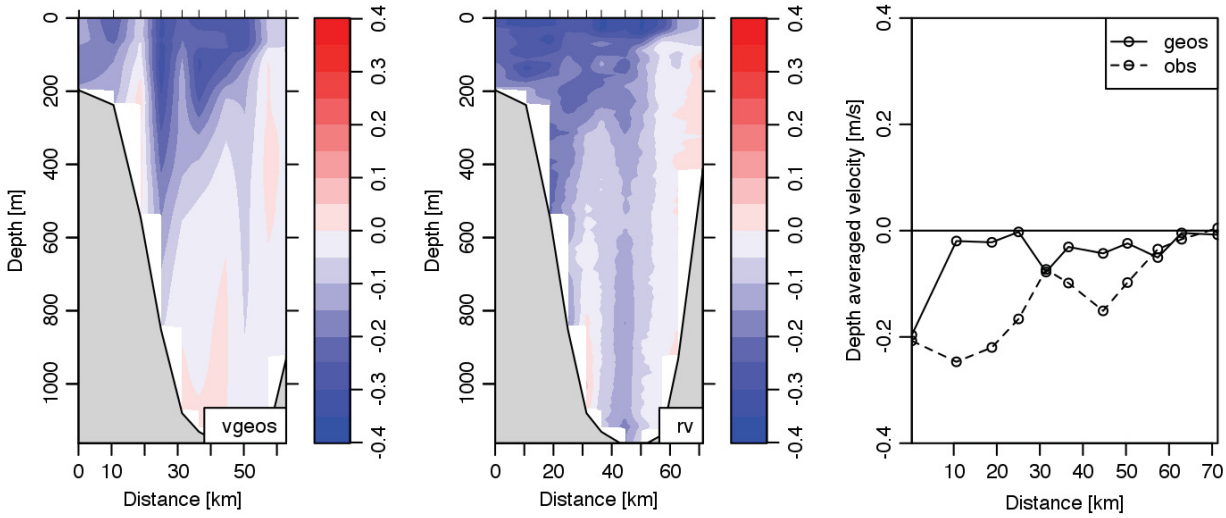

Figure 2.30: Calculated geostropic v velocity component (left) and LADCP v_r-velocity observations (middle), as well as the depth averaged v-velocity (right) for Flemish Pass 2013 transect.

this suggests that the flow in Flemish Pass may be primarily baroclinic.

2.5.2 Temporal

constituent	period	222 m	254 m	286 m	318 m	350 m	382 m
M2	12.42 hours	x	x	x	x	x	x

Table 2.6: Tidal constituents with an amplitude greater than 0.01 m/s for the Flemish Pass mooring.

Velocity measurements for Flemish Pass were recorded with a single ADCP. Measurements below 182 m will be focused on as observations between 38 m to 174 m have a total data return between 45% to 79%. Time series of velocity components at the same depths indicated in Figure 2.28 are summarized in Figure 2.31 and 2.32. As indicated in the LADCP measurements, as well as taking the bathymetry into consideration, flow is primarily southward throughout the year. Tidal components with an amplitude greater than 0.01 m/s include only the M2 tidal constituent, as summarized for each depth in Table 2.6. The u velocity component is small, $|u| < 0.01$ m/s throughout the year. In the bottom 200 m of the water column, the u component has a maximum around the beginning of January, which persists for a few weeks. The detided and low passed u component is relatively weak, suggesting that the variability is primarily due to tides. For the v component, there are tidal and high frequency variations in

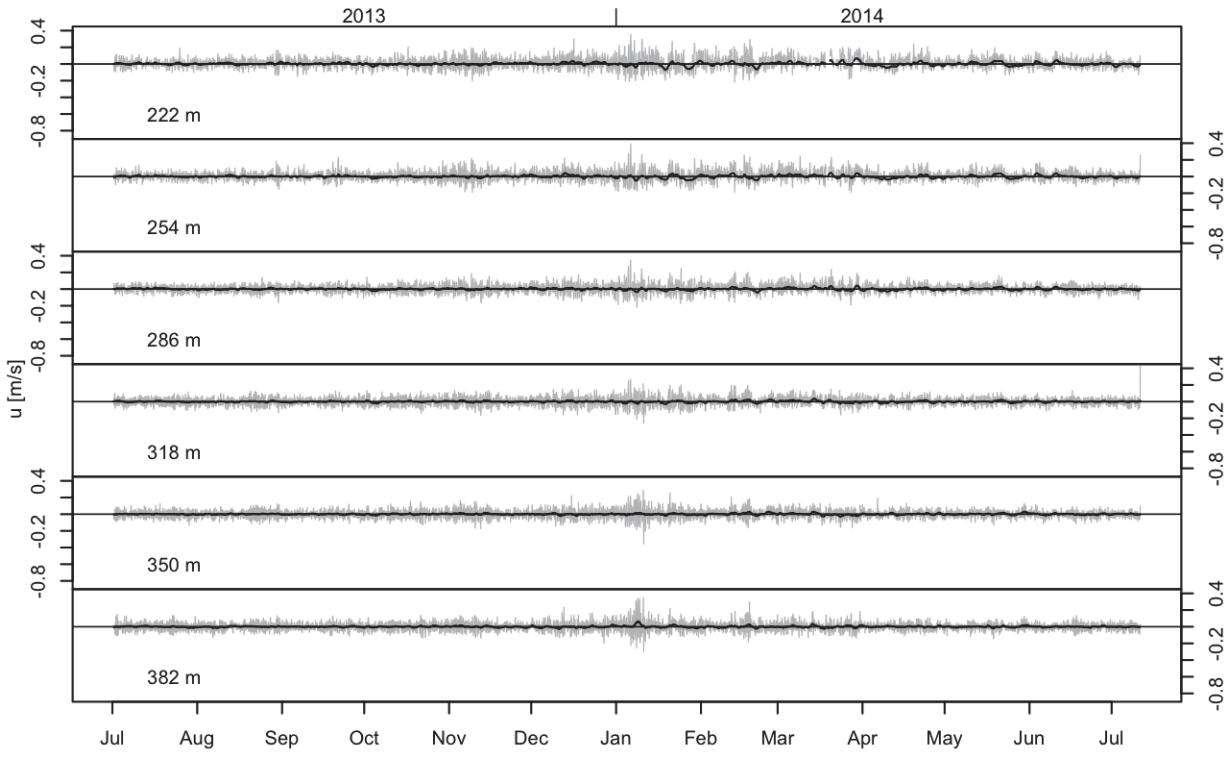

Figure 2.31: Time series of the u velocity component for Flemish Pass mooring. Grey line represents the raw data. The black line is the detided then low passed using a first order butter worth filter with a cutoff period of 4 days.

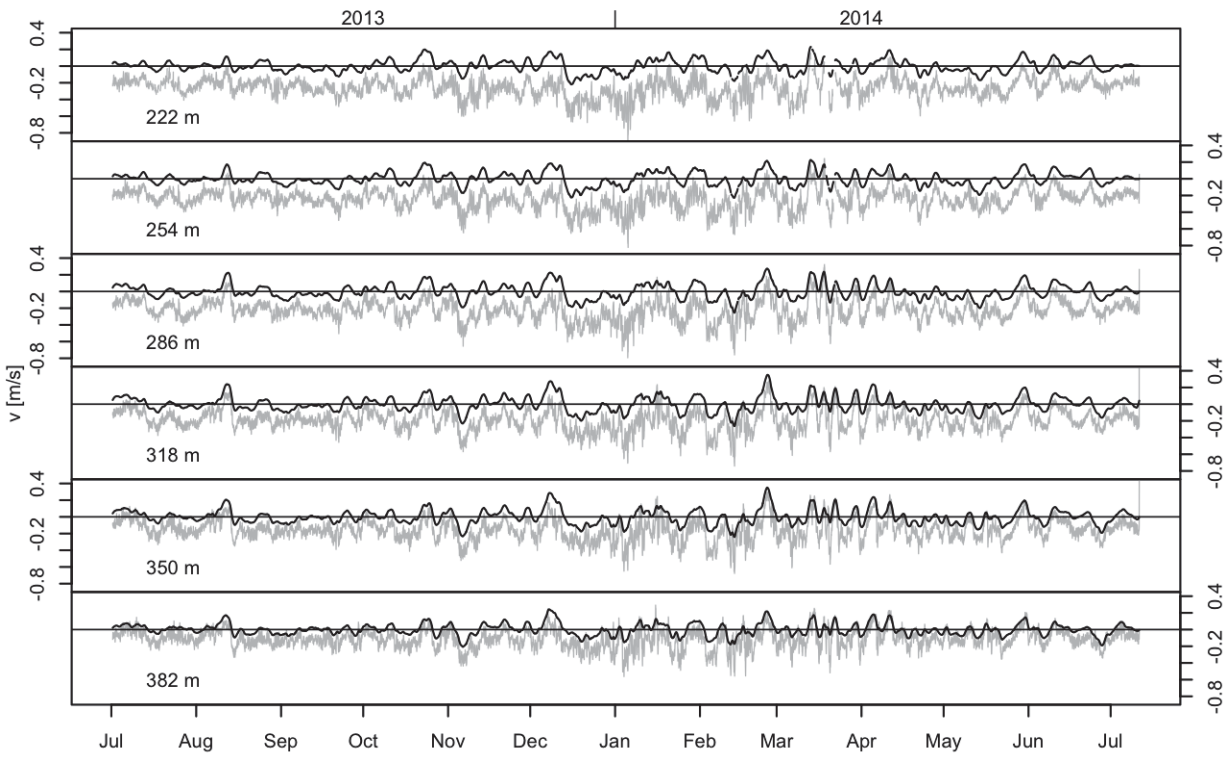

Figure 2.32: As in Figure 2.31, but for v-velocity component

the data, but when removed, a low frequency signal exists. The v component of velocity is primarily southward with a few flow reversal events. Importantly, for Chapter 3, these events primarily take place between February and May.

The spectrum of the speed indicates two spectral peaks, the higher power peak with a maximum around 21 days, and a secondary peak around 47 days (Figure 2.33). The relationship between power and depth for the two peaks is not as clear as it is for the other two moorings assessed in this thesis. The deepest observation has the lowest power at both peaks. The lower power here is expected as the v velocity magnitude is less than shallower observations as suggested by the smoothed values (Figure 2.32). From 222 m to 382 m, the power at the peaks follows the same trend as the previous moorings, with power increasing as depth increases. The power at 47 days for the three shallower depths is roughly equal.

2.6 Summary

The transects give a snapshot in time, and yield information about the spatial hydrography and velocity for July. In general, there is a surface intensified northeastward flow north of

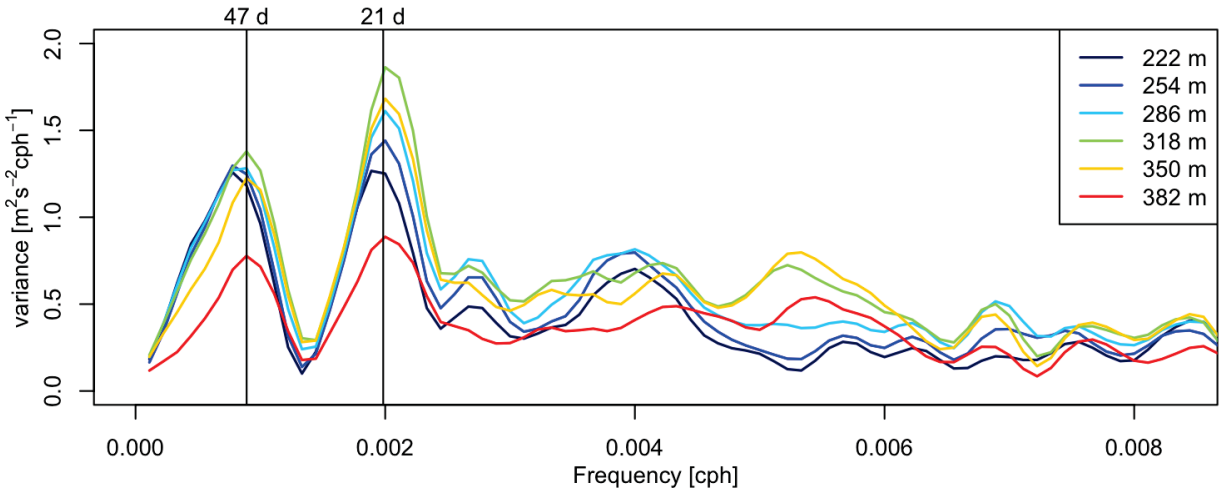

Figure 2.33: Spectrum of speed for Flemish Pass.

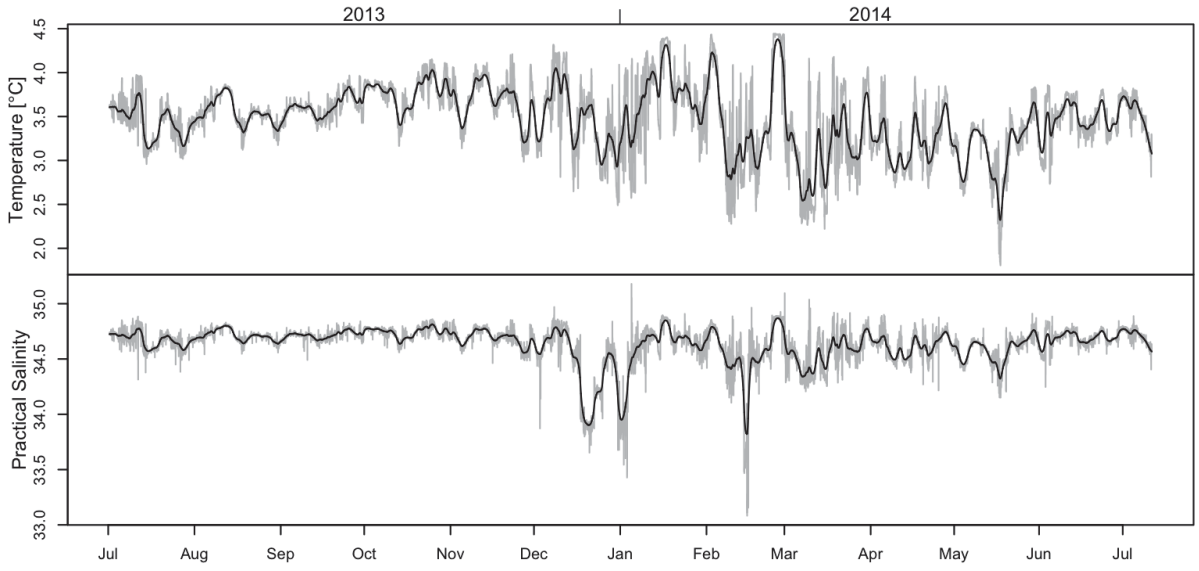

Figure 2.34: Time series for Flemish Pass, grey line indicates raw data and black line indicates low-passed data for (Top) temperature and (Bottom) salinity. Note that the Flemish Pass mooring was equipped with only one microCAT instrument.

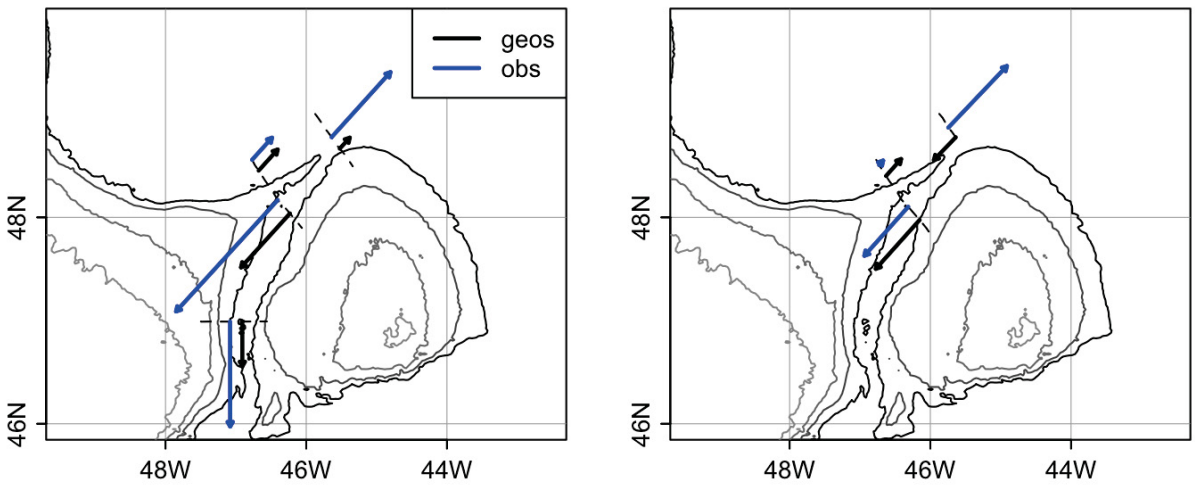

Figure 2.35: Summary map of laterally depth averaged velocity for each transect for (left) 2013 and (right) 2014.

Sackville Spur, which flows along bathymetry contours, and remains fairly surface-intensified along the northwest slope of Flemish Cap. Along the slope of the Cap, flow extends through the water column, where the direction and magnitude can vary for stations further down the slope. In the Flemish Pass, flow is surface intensified, and flows southwest. The location of this flow varies between the two years between the western part of the pass and thalweg. All transects, excluding the 2014 Flemish Cap due to decreased sampling, suggest weak clockwise flow along the upper slope of Flemish Cap. A summary of the laterally depth averaged geostrophic velocity indicates baroclinic flow north of Sackville Spur, and through Flemish Pass (Figure 2.35). Note that due the geography of the Sackville Spur transect, it was split into two, the general northeast flow north of the spur, and the southwest flow within the pass. Geostrophic velocities are much weaker along the Flemish Cap transect, and a comparison with the ship surveys indicating a greater barotropic component to the flow as supported by the flat isopycnals. Signatures of ULSW is apparent in all transects, and LSW in the Flemish Cap and northern part of Sackville Spur transect as summarized in Table 2.7. All transects suggest a layer of cold water beneath the warm surface layers, and this is most prominent in the Flemish Pass transect. During both years a lens of the cold, fresh water is on either side of Sackville Spur, with varying depths each year. This suggests less generation of the cold water, weaker advection off the Grand Banks, or stronger vertical mixing in the upper layers which dissipates the temperature signal more than the salinity signal.

	ULSW			LSW		
Transect	T (°C)	S	depth (m)	T (°C)	S	depth (m)
FC 2013	3.74 to 4.34	34.86 - 34.91	265 - 1020	4.34 to 3.33	34.91 - 34.92	1020 - 1600
FC 2014	3.64 to 4.08	34.8 - 34.87	320 - 1270	4.08 to 3.3	34.87 - 34.91	1270 - 1795
SS 2013	3.78 to 4.28	34.85 - 34.9	270 - 1190	4.28 to 3.35	34.9 - 34.92	1190 - 1805
SS 2014	3.69 to 4.22	34.8 - 34.89	265 - 1120	4.22 to 3.31	34.89 - 34.92	1120 - 1740
FP 2013	3.79 to 4.42	34.87 - 34.92	440 - 1105			

Table 2.7: Temperature, salinity, and depth ranges between the density limits of ULSW and LSW for each CTD transect.

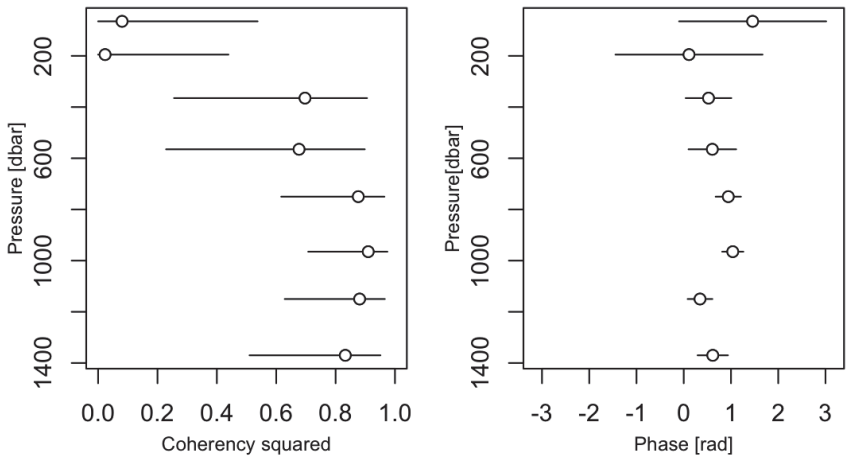

Figure 2.36: (Left) Coherence and (Right) phase of current speed between Flemish Cap and Sackville Spur mooring.

In 2013, the temperature and salinity range of the ULSW are similar, with the depth range varying (Table 2.7). The shallowest extent of the ULSW between the Sackville Spur and Flemish Cap transects are similar, with the deepest extent being larger at the Sackville Spur transect. The depth range of the ULSW is larger than the other two transects, and the thickness is similar to Flemish Cap. In 2014, the ULSW is colder and fresher with depth extents being similar to 2013. Comparing to values found in literature (Table 2.1), these observations are saltier and shallower.

For LSW, temperature, salinity, and thickness is roughly equal between the Flemish Cap and Sackville Spur transects. LSW waters extend deeper at the Sackville Spur transect than the Flemish Cap transect. Comparing these values to those found in the literature indicates that values found in the observations are warmer, saltier, and shallower.

All three mooring locations indicate a spectral peak with a maximum around 21 days, as well as a second peak, which is different for each mooring. The squared coherency at depth is

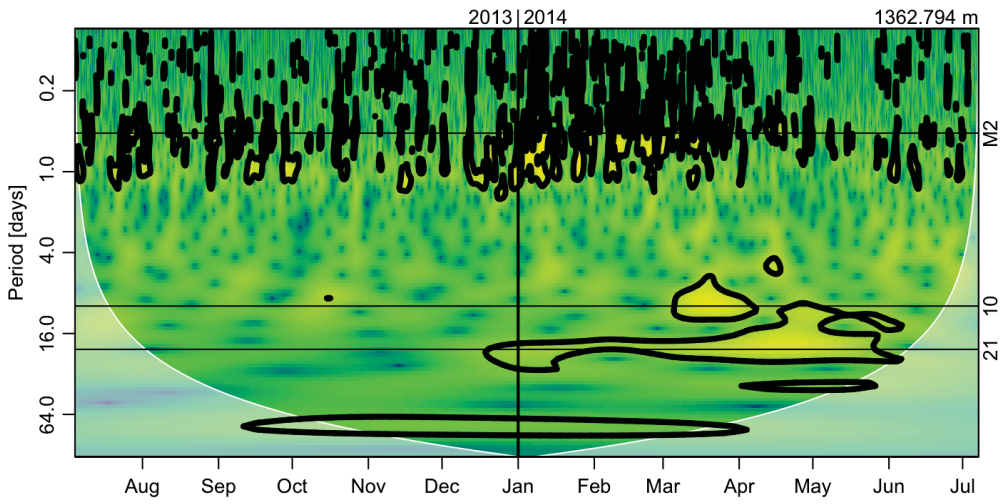

Figure 2.37: Wavelet of the detided u-velocity component from Flemish Cap mooring current meter at 1365 m.

close to 1 at this spectral peak for the Flemish Cap and Sackville Spur moorings, indicating vertical coherence in velocity measurements. Lateral squared coherence and phase of speed between each instruments may provide further insight (Figure 2.36). Near-surface speed, 65 m and 195 m indicates low to no coherency at the 21 day period. The coherency and phase are nearly identical for 365 m and 565 m. At and below 750 m there is lateral coherency between moorings locations. The phase ranges between 0.08 to 1.26, which has a phase time between -1.7 to -26.2 days respectively for the 21-day band. Using this time, and the distance between mooring locations, which is 82 km, gives a speed which ranges between -0.56 to -0.04 m/s.

Describing how oceanic frequency signals vary in time can be difficult for processes not coupled with the atmosphere. Unlike its atmospheric counter part, where time series measurements can be split into, *e.g.* seasonal timescales, oceanic measurements at depth require another technique. This can be achieved using wavelet analysis. Since measurements at depth are vertically and laterally coherent, wavelet results will only be discussed for the deepest RCM instrument from the Flemish Cap mooring. As seen in Figure 2.37, thick black outlines suggest areas where the peaks in the analysis are significant. The peak around 64 days should be taken with caution as the area is within the shaded area, meaning that such long-period signals are not well resolved in a time series of this brevity. Similar to what was found in the spectra of speed for all three moorings, the 21-day peak is more prominent between January and June, as well as a 10-day peak between March and April. Though, the 21-day peak bleeds into this time band, so it could be prevalent during a larger time span.

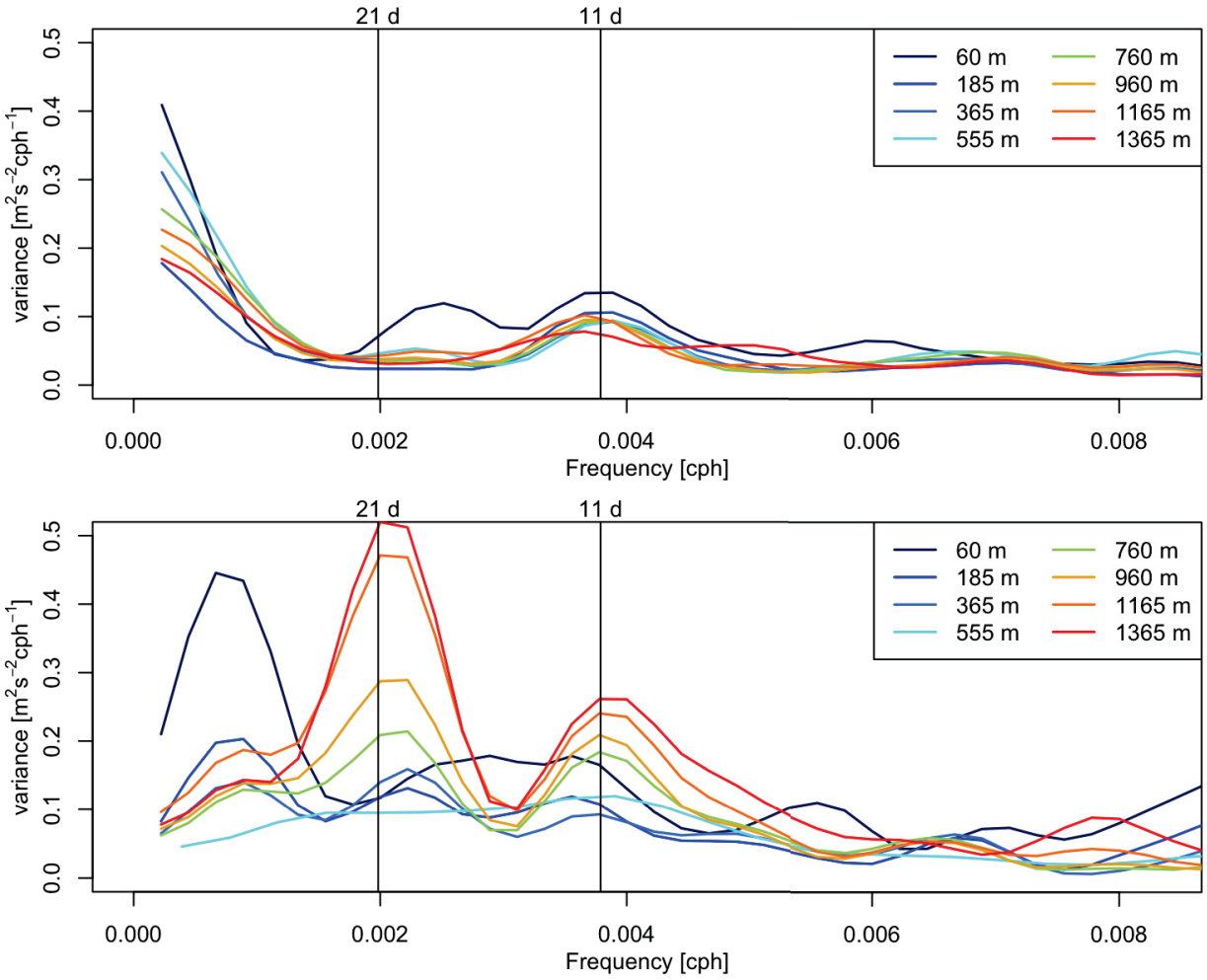

Figure 2.38: Spectrum of Flemish Cap velocity observations from (Top) July 2013 to December 2013 and (Bottom) January 2014 to July 2014.

Splitting the velocity time series up into two sections, one from July 2013 to December 2013 and the second from January 2014 to July 2014, and then finding the spectrum for each depth yields results suggested in Figure 2.37 by wavelet analysis. For the Flemish Cap observations, the spectral analysis of the first section of observations in Figure 2.38 indicates no spectral peak at 21 days. At 11 days, the peak is weaker and the structure of the peak as a function of depth is different from Figure 2.13. In the second half of the observations, Figure 2.38, the low frequency signals are observed, which have similar power to that of the spectrum from the entire year. Results for the Sackville Spur mooring are similar.

The analysis in this chapter has revealed

1. A three week spectral peak from moored velocity measurements at all three mooring

locations, where the signal is predominately between January and May.

2. The power of the spectral peak, in general, increases with increasing depth.

3. Lateral and vertical coherence between velocity measurements.

A possible dynamical context of the above results will be tested in the next chapter.

Chapter 3

Baroclinic Topographic Rossby Waves

3.1 Introduction

Given the observed timescales ($\gg f^{-1}$), and the proximity to topography, a natural candidate for contextualizing the 3-week spectral peak is topographic Rossby waves. Topographic Rossby waves have a restoring force that involves the conservation of potential vorticity. For example, in the barotropic case, potential vorticity,

$$\Pi = \frac{\zeta + f}{H} \tag{3.1}$$

is conserved following water parcels. Here, ζ is relative vorticity, f is the Coriolis parameter, and H is the water depth (*Cushman-Roisin*, 1994, p57). When a fluid parcel in the northern hemisphere moves to deeper/shallower water along a slope, it attains cyclonic/anticyclonic relative vorticity, and this leads to a restoring force that causes a wave that propagates nearly along isobaths, with shallow water on the right (*Cushman-Roisin*, 1994, p57). The baroclinic case is more complicated, but the above explanation is analogous (The mathematical details are given in the next section). Baroclinic topographic Rossby waves have been observed in the ocean in currents flowing over sloped topography (*i.e.* the continental slope) in stratified fluids. In the seminal example of *Rhines* (1970), the dispersion relationship for baroclinic Rossby waves was derived. *Rhines* (1970) work motivated studies of such waves along the western Atlantic shelf (see *e.g Thompson and Luyten* (1976); *Allen* (1980); *Louis et al.* (1982); *Pickart* (1995)), locations of these studies are summarized in Figure 3.1.

Previous studies, as listed above, have noted distinguishing features in observations which have led to suggesting the presence of topographic Rossby waves. These features include

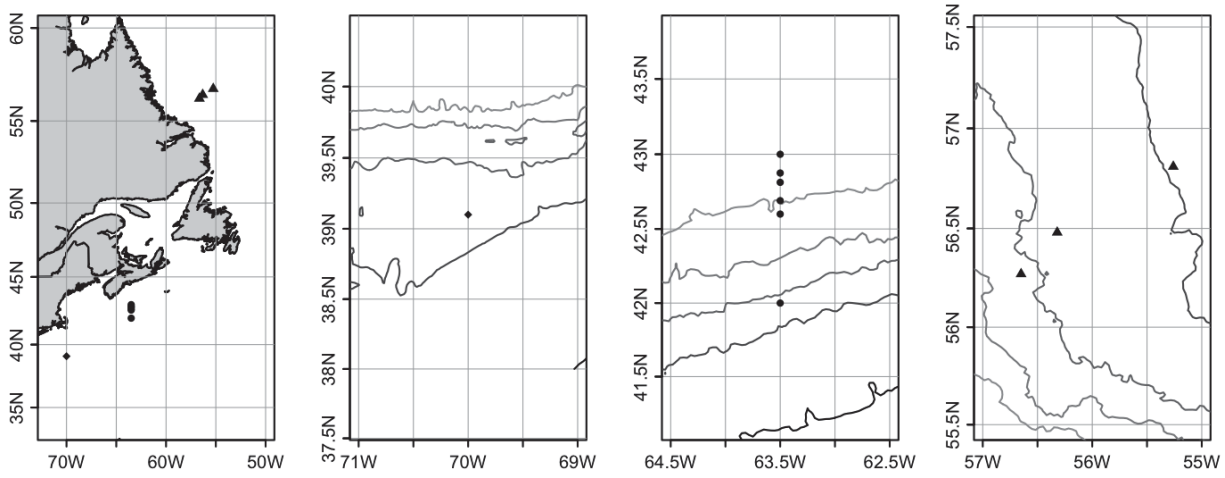

Figure 3.1: Map of mooring locations from previous studies, from left to right, summary map of all mooring locations in north Atlantic, more detailed bathymetry with mooring locations for *Thompson and Luyten* (1976), *Louis et al.* (1982), *Allen* (1980).

1. A sub-inertial timescale signal in auto-correlation in the along-isobath velocity component, (*Louis et al.*, 1982), as well as a corresponding peak in the spectrum (*Allen*, 1980).

2. Increasing energy with depth for the spectral band (*Louis et al.*, 1982).

3. Vertical coherence between current meters on a mooring, (*Louis et al.*, 1982), and lateral coherence for sufficiently close moorings (*Louis et al.*, 1982).

4. Principal axis of the velocity tends to be at some small angle relative to isobaths due to rectilinear motion (*Allen* (1980), *Louis et al.* (1982)).

The analysis of the temporal variability of the moored current meter observations in Chapter 2 has demonstrated all of these features. In this chapter, another, more detailed and dynamically motivated test for Rossby waves will be used, which is based on the dispersion relationship.

3.2 Derivation of Dispersion Relationship

A common tool used to discern waves in data is to compare observations with the theoretical dispersion relationship. This relationship expressed frequency in terms of wavenumber, a

connection of space and time variation that is developed from an analysis of the underlying dynamical equations.A wave is said to be dispersive such that the frequency, ω, is dependent on the horizontal wavenumber, k, such that the wave crests propagate with speed, $c = \omega/k$, which is also known as the phase speed. Following the treatment of *Rhines* (1970), who considered the combined effects of stratification and bathymetry, the derivation of the dispersion relationship, which was derived for general bathymetry as in *Meinen et al.* (1993), is as follows.

Starting with the $2D$ linear momentum, continuity, and density advection equations,

$$u_t - fv = -\frac{1}{\rho_0} p'_x \tag{3.2}$$

$$v_t + fu = -\frac{1}{\rho_0} p'_y \tag{3.3}$$

$$u_x + v_y + w_z = 0 \tag{3.4}$$

$$-p'_z - \rho' g = 0 \tag{3.5}$$

$$\rho'_t - \frac{\rho_0 N^2}{g} w = 0 \tag{3.6}$$

where $\vec{u} = (u, v, w)$ are velocity components, subscripts indicate partial differentiation,

$$f = f_0 + \beta y \tag{3.7}$$

is the Coriolis parameter, $p'(x, y, z)$ is the pressure anomaly, ρ' is density, g is gravity, and

$$N^2 = -\frac{g}{\rho_0} \frac{\partial \rho}{\partial z} \tag{3.8}$$

is the Brunt-Väisälä frequency on a β plane.

Deriving a dispersion relationship requires either assuming a wave form that lets the derivatives be transformed into factors and then solving the above equations using linear algebra techniques, or solving the equations systematically to obtain a single equation in terms of a single variable. Here, the latter will be demonstrated following the approach of *Meinen et al.* (1993). Taking the time derivative of Equation (3.5) yields

$$\rho'_t = -\frac{1}{g} p'_{zt} \tag{3.9}$$

which may be used in Equation 3.6,

$$w = -\frac{1}{\rho_0 N^2} p'_{zt} \tag{3.10}$$

This has eliminated the density derivatives in the system of equations. Next, eliminate pressure from the momentum equations by cross differentiating, *i.e* $(3.2)_y$ - $(3.3)_x$, and using continuity yields the linear vorticity equation,

$$(v_x - u_y)_t - f_0 w_z + \beta v = 0 \tag{3.11}$$

Next, consider the quasi-geostrophic approximations of the velocity field such that $\beta y \ll f_0$, where $u_t(v_t)$ can be ignored compared with $f_0 v(f_0 u)$ to yield

$$v = \frac{1}{\rho_0 f} p'_x \tag{3.12a}$$

$$u = \frac{1}{\rho_0 f} p'_y \tag{3.12b}$$

substituting into the linear vorticity equation yields the quasi-geostrophic equation,

$$\frac{1}{\rho_0 f_0}\left[\left(p'_{xx} + p'_{yy}\right)_t + \beta p'_x\right] = f_0 w_z \tag{3.13}$$

the w_z term may be eliminated by using Equation (3.10) to obtain

$$\left(p'_{xx} + p'_{yy} + \left(\frac{f_0^2}{N^2} p'_z\right)_z\right)_t + \beta p'_x = 0 \tag{3.14}$$

which has reduced Equations (3.2) through (3.6) to a single variable partial differential equation of higher order terms. In order to solve for p', impose kinematic boundary conditions of a rigid lid at the surface and no normal flow through the bottom, or,

$$w = 0 \qquad \text{at } z = 0 \tag{3.15}$$

$$w = -\vec{u} \cdot \nabla \vec{H} \qquad \text{at } z = -H \tag{3.16}$$

note that $\vec{u}$ is the quasi-geostrophic approximation of velocity, as given in Equations (3.12a)

and (3.12b). Using Equation (3.10), the boundary condition in term of p' are

$$p'_{zt} = 0 \qquad \text{at } z = 0 \tag{3.17}$$

$$p'_{zt} = \frac{N^2}{f_0}\left(H_x p'_y - H_y p'_x\right) \qquad \text{at } z = -H \tag{3.18}$$

Equations (3.14), (3.17), and (3.18) are all the required components in order to solve for an analytic solution for p'. Following [*e.g Meinen et al.* (1993)], focus on a plane wave solution

$$p'(x, y, z, t) = \mathcal{F}(z)\exp(i(kx + ly + \omega t)) \tag{3.19}$$

Substituting the wave form into the quasi geostrophic dynamical equation, Equation (3.14) yields,

$$\mathcal{F}_{zz} = \lambda^2 \mathcal{F} \tag{3.20a}$$

where

$$\lambda^2 = \frac{N^2}{f_0^2}\left(k^2 + l^2 + \beta k/\omega\right) \tag{3.20b}$$

Equations (3.20a) and (3.20b) together represent an eigen-value problem in the Sturm-Liouville form. Substituting the plane wave solution, Equation (3.19) into Equations (3.17) and (3.18) yields boundary conditions in terms of the vertical structure of p',

$$\mathcal{F}_z = 0 \qquad \text{at } z = 0 \tag{3.21}$$

$$\omega\mathcal{F}_z = \frac{N^2}{f_0}\left(l\,H_x - k\,H_y\right)\mathcal{F} \qquad \text{at } z = -H \tag{3.22}$$

Using the top boundary condition, Equation (3.21), and Equation (3.20a), the particular solution of $\mathcal{F}$ is

$$\mathcal{F}(z) = \cosh(\lambda z) \tag{3.23}$$

so the waveform is

$$p' = \cosh(\lambda z)\exp(i(kx + ly - \omega t)) \tag{3.24}$$

The bottom boundary condition, Equation (3.18), and the waveform may now be used to

solve for the dispersion relation, yields

$$p'_{zt}|_{-H} = -i\omega\lambda \sinh(-\lambda H) \exp(i(kx + ly - \omega t)) \tag{3.25}$$

for the left hand side of Equation (3.18), while the right hand side is

$$\frac{N^2}{f_0^2}\left(H_x p'_y - H_y p'_x\right)\Big|_{-H} = i\frac{N^2}{f_0^2}\cosh(-\lambda H)\exp(i(kx + ly - \omega t))\left(H_x l - H_y k\right) \tag{3.26}$$

Equating these yields the dispersion relation

$$\omega = \frac{N}{\sqrt{k^2 + l^2 + \beta k/\omega}}\left(H_x l - H_y k\right)\coth(\frac{NH}{f_0}\sqrt{k^2 + l^2 + \beta k/\omega}) \tag{3.27}$$

In the geostrophic limiting case where $\mathrm{O}(w_z) \ll \mathrm{O}(u_x, v_y)$, the continuity equation, assuming a plane wave solution is,

$$ku^* + lv^* = 0 \tag{3.28}$$

such that (k, l) is orthogonal to (u^*, v^*). Let θ be the angle between ∇H and $\vec{k}$ such that by geometry, θ is also the angle between $\vec{u}$ and isobaths.

If $\beta k/\omega \ll \kappa_H$, then Equation (2.5) of *Rhines* (1970) is recovered. The main difference between *Rhines* (1970) and the solution above is that *Rhines* (1970) solved for a channel with rigid vertical walls, and 1-D planar bottom slope geometry. The above treatment is for an infinite domain, takes the planetary beta-effect into account, and 2-D planar bottom bathymetry. Assuming $\kappa_H^2 \approx k^2$, $\beta = f/R_{earth}$, where R_{earth} is the radius of the Earth, and $\omega \approx f/50$, then the above inequality holds true, and thus, Equation (3.27) can be written in the same form as *Rhines* (1970) form. It will be used over the dispersion relationship, Equation (3.27) as the k and l components will be difficult to approximate given the mooring spacing. In order to contextualize if the low frequency variability is associated with topographic Rossby waves, *Rhines* (1970) dispersion relationship will be used

$$\omega = \alpha\, N\, \sin(\theta)\, \coth\left(\frac{\kappa_H\, N\, H}{f}\right) \tag{3.29}$$

where ω is the frequency, α is the linear bottom slope, $\kappa_H^2 = k^2 + l^2$ is the horizontal wavenumber, k is the alongshore wavenumber and l is the offshore wavenumber, H is the total water depth, f is the Coriolis parameter, and θ, and explained above is the angle between

Limit	Dispersion relation	Wave type
$\kappa N H/f > 1$		baroclinic bottom trapped
$\kappa N H/f \gg 1$	$\omega = \alpha N \sin(\theta)$	bottom trapped
$\kappa N H/f = 1$	$\omega = \alpha N \sin(\theta) \coth\left(\frac{\kappa N H}{f}\right)$	weakly bottom trapped
$\kappa N H/f < 1$	$\omega = -\frac{\alpha}{H}\frac{k}{k^2+l^2}$	barotropic

Table 3.1: Limiting cases of topographic Rossby waves from Equation 3.29 as summarized by *Allen* (1980).

the wavenumber vector and upslope, and is also the angle between the velocity vector and the isobaths.

Limiting cases of Equation 3.29 have been described for different modes of topographic Rossby waves by *Allen* (1980) summarized in Table 3.1. Since this model is applicable to constant values of α and N, at a given location, the limits of ω are dependent on the horizontal wavenumber components and the angle between the velocity vector and isobaths.

3.3 Methods

3.3.1 Calculation of buoyancy frequency, N

The theory outlined by *Rhines* (1970), and as in the above, assumes constant stratification, N, or linear density. This allowed a linear regression model to be used to calculated σ_θ as a function of z, with the slope yielding the value of N. Because the deep waters are the focus here, the linear regression was fit between the depths of the two deeper current meters. Since density at depth is fairly constant throughout the year, see Figure 3.2, a CTD profile near each mooring location was used.

3.3.2 Calculation of bottom slope, α

The dispersion relationship derived by *Rhines* (1970) assumes a linear $1D$ planar sloped bottom. Using ETOPO2 bathymetry data, defined on a 2-minute (roughly 4 km) grid, the angle in the cross isobath direction was found using the contour algorithm, explained in detail in Appendix C. The slope, α, was estimated by fitting $H = H(y, z) = \alpha y$ to bathymetry data in the onshore and offshore direction about the point of interest (Figure 3.3).

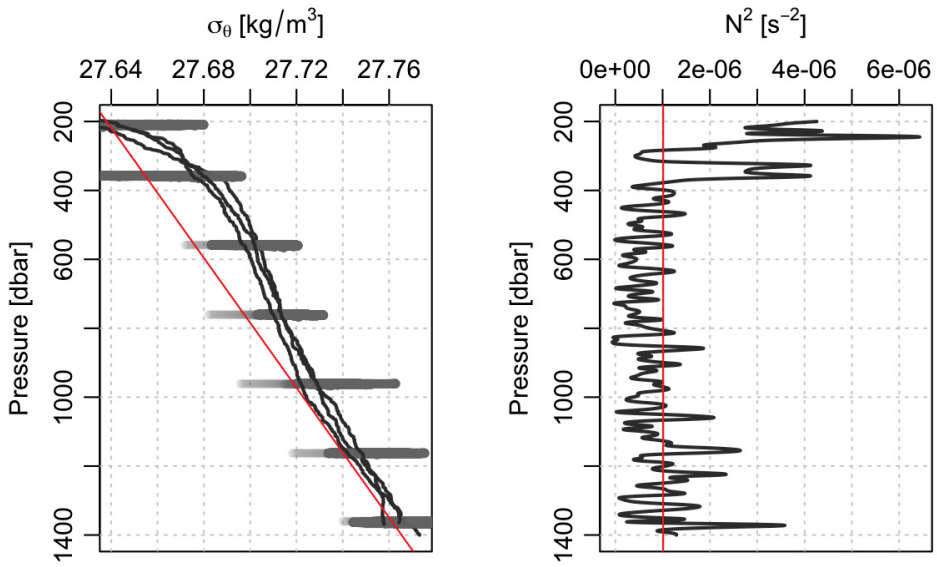

Figure 3.2: Example calculation of N. (Left) Potential density (σ_θ) as a function of depth for the CTD profiles near the Flemish Cap mooring as given by the black lines, and the low-pass σ_θ from microCAT instruments as represented by the grey dots. Red line indicates the predicted fitted values using data from a CTD profile between the two deepest current meter instruments. (Right) N^2 as a function of depth from the CTD profiles (dark grey lines), and the calculated value from the constant N model (red line).

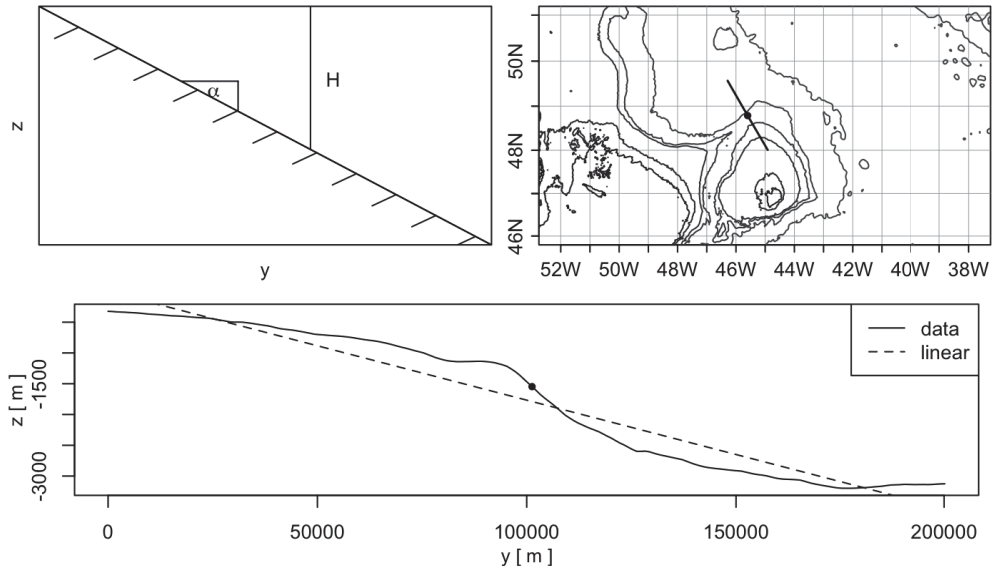

Figure 3.3: Calculation of α. (Top Left) Schematic of *Rhines* (1970) representation for bottom topography, $z = \alpha y$. (Top Right) Map of region, black dot indicates mooring location, thick black line is sampled ETOPO2 bathymetry data in the upslope and downslope direction. (Bottom) Bathymetry along the black line given in the map, the black dot indicates the mooring location, and the linear fit, as indicated by the dashed line.

3.3.3 Estimation of wave-isobath angle, θ

The angle of the principal axis of velocity vectors, θ_v was calculated from the eigenvectors of the co-variance between horizontal velocity components. The along-isobath angle, θ_b, is found using the contour algorithm summarized in Appendix C, then $\theta = \theta_v - \theta_b$.

3.3.4 Estimation of horizontal wavenumber, κ_H

3.3.4.1 Two-point Method

From *Rhines* (1970), the predicted horizontal velocity components are proportional to

$$V = V_0 \cosh\left(\frac{\kappa_H N}{f} z\right) \tag{3.30}$$

Following from Equation 3.30, *Thompson and Luyten* (1976) defined the ratio of kinetic energy, R, between two depths, shallower, z_1 and deeper, z_2, as

$$R = \left[\frac{\cosh\left(\frac{N}{f}\kappa_H\, z_1\right)}{\cosh\left(\frac{N}{f}\kappa_H\, z_2\right)}\right]^2 \tag{3.31}$$

Using spectra output, R is found by taking the ratio of the horizontal velocity component spectrum at a shallower depth, z_1, to a spectrum at a deeper depth, z_2. Knowing the background parameters, N, f, z_1, and z_2, κ_H is solved for using Equation (3.31). *Thompson and Luyten* (1976) used the cross isobath kinetic energy ratio as it "might be less influenced by non-linear phenomena and the mean flow". For consistency, the same will be done with these data, but results will also be compared to along-isobath velocity, and the speed.

3.3.4.2 Regression Method

The method for calculating κ_H as given in *Thompson and Luyten* (1976) is useful for moorings that only have two current meters. This can result in depth varying estimates of κ_H if multiple instruments are on a mooring, in contradiction of the form of the wave that the method is designed to detect. For the Flemish Cap and Sackville Spur moorings, current meters have a vertical resolution of approximately 200 m. Therefore, the method defined by *Thompson and Luyten* (1976) will be extended to estimate κ_H for the watercolumn. A regression method will be used with Equation (3.30).

Mooring	α	N	f	H
FC	$(1.77\pm\ 0.31)\times10^{-2}$	$(1.09\pm\ 0.01)\times10^{-3}$ s^{-1}	1.1×10^{-4} s^{-1}	-1485 m
SS	$(1.83\pm\ 0.56)\times10^{-2}$	$(1.05\pm\ 0.01)\times10^{-3}$ s^{-1}	1.09×10^{-4} s^{-1}	-1454 m
FP	$(1.58\pm\ 0.44)\times10^{-2}$	$(3.76\pm\ 0.08)\times10^{-3}$ s^{-1}	1.07×10^{-4} s^{-1}	-409 m

Table 3.2: Background parameters for all mooring locations.

Mooring	L_R	L	a
FC	16 km	36 - 80 km	2 - 5
SS	16 km	32 - 96 km	2 - 5
FP	4 km	66 - 241 km	16 - 60

Table 3.3: Rossby radius, L_R, horizontal displacement in the along-isobath direction, L, and number of Rossby radii, a, for each mooring location.

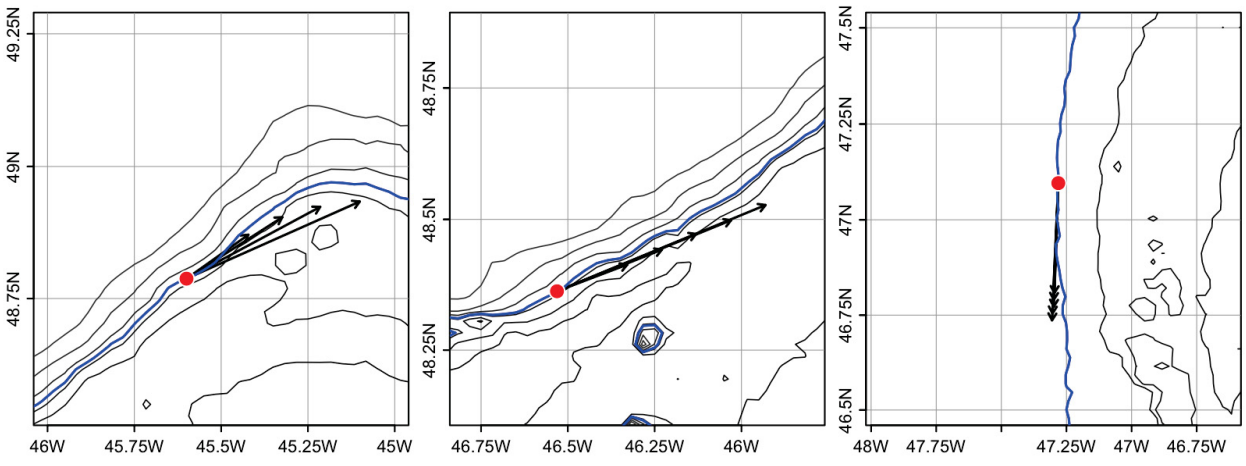

Figure 3.4: Along slope calculation for mooring locations. (Left) Flemish Cap, (Middle) Sackville Spur, and (Right) Flemish Pass. Arrow lengths are proportional to the looking distance chosen based on the Rossby radius for each location.

3.4 Results

Background parameters, N, α, f, and H for each mooring location using the methods outlined earlier in the chapter are summarized in Table 3.2.

In order to estimate the along-isobath angle for each mooring location, the looking distance, L using the contour method, described in detail in Appendix C, needs to be chosen for each location. The value of L will be chosen based on physical quantities, particularly the Rossby radius. The baroclinic Rossby radius, L_R for continuously stratified fluid as defined by *Cushman-Roisin* (1994, p185) is,

$$L_R = \frac{\sqrt{g'H}}{f} \tag{3.32}$$

where g' is reduced gravity,

$$g' = -H\left(\frac{g}{\rho_0}\frac{\partial\rho}{\partial z}\right) \tag{3.33}$$

$$= N^2 H \tag{3.34}$$

so,

$$L_R = \frac{NH}{f} \tag{3.35}$$

using background parameters, the Rossby radius was calculated for each mooring (Table 3.3). Define the looking distance, L, as

$$L = aL_R \tag{3.36}$$

where a is the number Rossby radii derived from observations. To find a, L is estimated from the progressive vector diagrams of velocity to find the scale of the horizontal wave displacement in the along-isobath direction. These values for each mooring are summarized in Table 3.3. The range of aL_R will be tested in calculating the along-isobath angle for each mooring. The Flemish Pass mooring has a wide L_R range, for simplicity $16 \leq L_R \leq 20$ will be used.

The range of L, as defined in Equation (3.36), in order to calculate the along-isobath angle, θ_b was compared for each mooring (Figure 3.4). The Flemish Pass angle is not sensitive to the choice of L based on the horizontal extent of velocity and L_R. The Sackville Spur angle is under estimated by visual inspection, but the difference appears to be small. The Flemish

Cap along-isobath angle is sensitive to the tested L. The bathymetry in this region is more complex than the other two locations, as the mooring is near the northern point of the cap. The two smaller values of L better estimates θ_b by visual inspection. The estimation of κ_H and θ will be summarized for each mooring location.

3.4.1 Flemish Cap

3.4.1.1 Wave-isobath angle, θ

The along-isobath angle using $L = 36$ to 80 km for the Flemish Cap mooring location ranged from 35.3 to 23.9° respectively counterclockwise from 0° pointing east and 90° pointing north. The spectrum of the detided speed data, as summarized in Figure 2.13, was vertically coherent below 185 m, so, the analysis will focus on these depths. The range of θ based on the choice of L at each depth is summarized in Table 3.4. A θ of 0° indicates along-isobath flow, 90° indicates cross-isobath flow downslope, and −90° indicates cross-isobath flow upslope. The sign of θ is dependent on the value of L, as noted in Table 3.4, indicating that flow is slightly upslope and downslope. However, note that the angle is small, with flow being along-isobath near the bottom and an absolute maximum at 555 m. For topographic Rossby waves, the sign of the angle does not matter for the restoring force as $\sin(\theta)$ is symmetric about 0°. When using the angle in the dispersion relationship, the absolute value will be used.

depth (m)	θ (°)
365	-0.3 to 8.4
555	-12.3 to -7.9
760	-2.2 to 2.1
960	-3.1 to 5.6
1165	-2.3 to 6.4
1365	-1.4 to 5.8

Table 3.4: Calculated θ range at each depth for Flemish Cap mooring

3.4.1.2 Horizontal wavenumber, κ_H

In order to calculate κ_H, the velocity data must be rotated to follow the defined coordinate system of the problem defined in Section 3.2. Using θ_b, the velocity components were rotated, and the results supplied in the remainder of this section will use rotated, de-tided, low-passed velocity components. First, the results of the two-point method using *Thompson and Luyten* (1976) method will be summarized and then the results of the extended regression method.

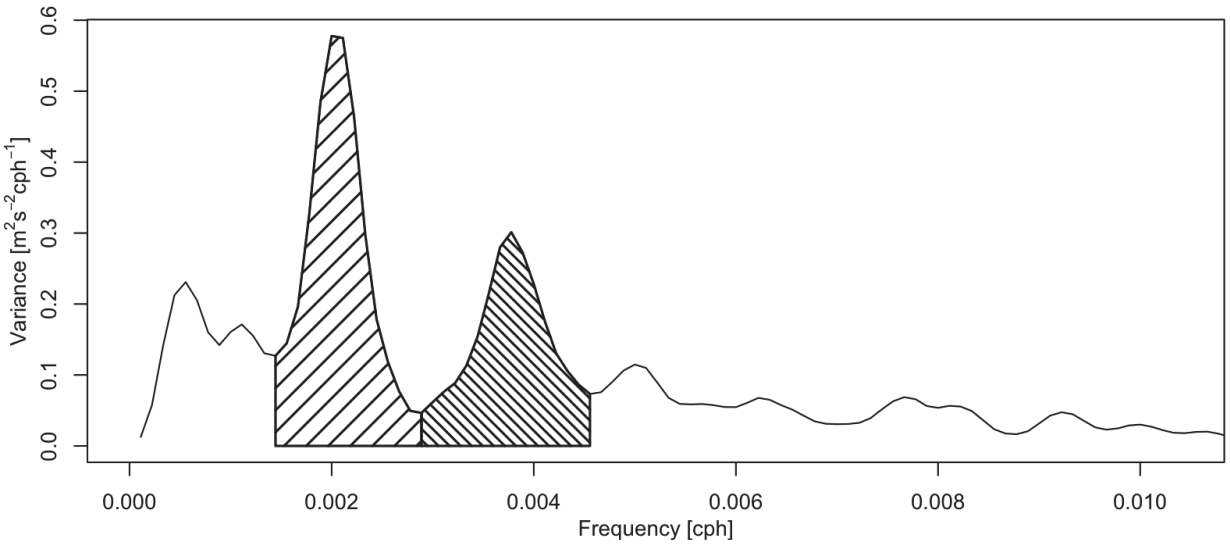

Figure 3.5: Example of variance under spectrum curve for two dominant peaks in spectrum.

In *Thompson and Luyten* (1976), only the cross-isobath velocity was used. Here, results presented will include the along-isobath and the speed as well. Also, the different values of θ_b based on the choice of L will be compared in order to test the sensitivity. The value of R was averaged over the total 3-week spectral peak, an example of the peak range is shown in Figure 3.5. In order for the two-point method to solve for κ_H, $0 \leq R \leq 1$. The resulting κ_H calculated using this method for the horizontal velocity components and speed is summarized in Table 3.5. This method results in wavelengths that vary as a function of depth, and varies based on the angle of rotation. The wavelength ranges from 26 to 189 km.

z_1-z_2 (m)	κ_H ($\times 10^{-4}$1/m) from u	κ_H ($\times 10^{-4}$1/m) from v	κ_H ($\times 10^{-4}$1/m) from U
365-565	NA	NA	NA
565-750	2.32 to 2.37	0.69 to 1.03	2.21
750-965	0.97 to 1.01	0.49 to 0.49	0.86
965-1150	1.43 to 1.47	NA	1.48
1150-1370	0.33 to 0.41	0.6 to 0.6	NA

Table 3.5: Calculated κ_H along and cross-isobath velocity components and speed using the two-point method for Flemish Cap mooring.

For the regression method, similar to the two-point method, results from the spectra are used. Here, the variance under the spectra peak is calculated (see example of variance calculation in Figure 3.5). Fitting Equation (3.30), requires that the variance increases as

depth increases. This is suggested in the data, as shown in Figure 2.13. As in the two-point method, the angle of rotation will be tested. Regressing Equation (3.30) was successful for all values of L for the along-isobath velocity (Table 3.6). The wavelength ranged from 35 to 37 km. There was only one successful fit for the cross-isobath velocity, which was for the largest value of L, which gave a wavelength of 71 km. For the speed, the angle of rotation does not matter as the speed is preserved when rotated, *i.e*

$$u' = u\cos(\theta) + v\sin(\theta) \tag{3.37}$$

$$v' = -u\sin(\theta) + v\cos(\theta) \tag{3.38}$$

where (u', v') are the rotated velocity components, the speed is defined as $U = \sqrt{(u')^2 + (v')^2} = \sqrt{u^2 + v^2}$. The resulting wavelength was 39 km.

velocity component	κ_H $\times 10^{-4}$ (1/m)	total fitted profiles
u	1.7 to 1.78	4/4
v	0.88	1/4
U	1.63	

Table 3.6: Calculated κ_H for along and cross-isobath velocity components and speed using the regression method for Flemish Cap mooring.

Comparing the estimates of ω from the spectra of speed, θ from the along-isobath angle and the principal axis of velocity, and κ_H from the two-point method and the variance regression, the values were overlaid on the schematic of the dispersion relation, Equation (3.29), as shown in Figure 3.6. An intersection of all three variables inferred from the data indicates consistency with topographic Rossby waves. For the northern Flemish Cap mooring, all variables intersect, suggesting that the 3-week period in the data can be contextualized in terms of topographic Rossby waves.

3.4.2 Sackville Spur

3.4.2.1 Wave-isobath angle, θ

The along-isobath angle for the Sackville Spur mooring location using $L = 32$ to 96 km ranged from 20.8 to 22.4°, with the same coordinate system as defined in Section 3.4.1. The spectrum of the detided speed data, as summarized in Figure 2.24, was vertically coherent at and below 365 m, therefore, the analysis will be of focus on these depths. The calculated θ for each L

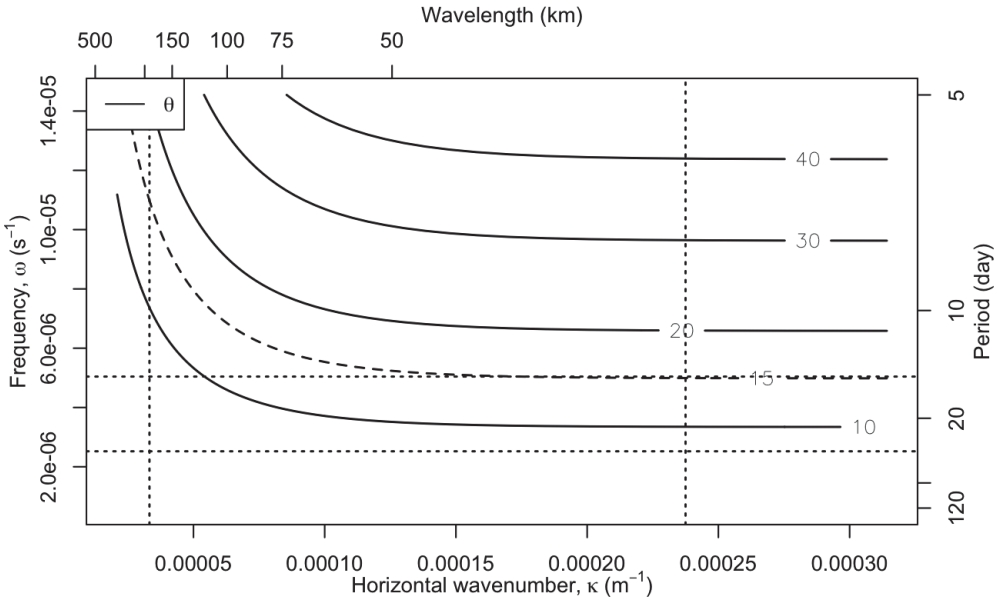

Figure 3.6: Contour plot of θ for given ω and κ_H from the dispersion relationship for topographic Rossby waves for the Flemish Cap mooring. Dotted vertical lines indicate range of κ_H from the two-point and regression method. Dotted horizontal lines indicate range of ω of the 3-week spectra peak. Dashed lines indicate range of θ inferred from data, note that the lower bound is not within the range of the plot.

is summarized in Table 3.7. The range of θ_b is tighter than the Flemish Cap mooring, as bathymetry is more simple, therefore, so is the range of θ for each depth. Similar to Flemish Cap, θ is negative in the upper 965 m indicating that flow is predominantly upslope. Below 965 m the direction is downslope, with flow at 965 m being roughly along-isobath.

depth (m)	θ (°)
365	-7.5 to -9.2
565	-5.5 to -7.2
750	-7.6 to -9.2
965	-0.2 to 0.7
1150	0.4 to 2
1370	4.2 to 5.8

Table 3.7: Calculated θ range at each depth for Sackville Spur mooring

3.4.2.2 Horizontal wavenumber, κ_H

As for the Flemish cap mooring, and using different values of L, results from the two-point method for estimating κ_H will be presented, and then results from the regression method. For the two-point method, results varied between the velocity components and speed, Table

3.8. For the along-isobath velocity, a maximum wavelength was calculated between depths 565 and 750 m, which ranged between 277 to 315 km. The other depths give a wavelength range between 58 to 164 km. Only one value was able to be calculated for the cross-isobath velocity component as $R > 1$ for all depths except between 1150 to 1370 m, which gave a wavelength range of 46 to 56 km. The speed gave a range of wavelengths of 74 to 109 km.

z_1-z_2 (m)	κ_H ($\times 10^{-4}$1/m) from u	κ_H ($\times 10^{-4}$1/m) from v	κ_H ($\times 10^{-4}$1/m) from U
365-565	1.08 to 1.09	NA	NA
565-750	0.2 to 0.23	NA	NA
750-965	0.68 to 0.7	NA	0.85
965-1150	0.38 to 0.39	NA	0.67
1150-1370	0.42 to 0.43	1.11 to 1.36	0.58

Table 3.8: Calculated κ_H along and cross-isobath velocity components and speed using the two-point method for Sackville Spur mooring.

Similar to the Flemish Cap mooring, the regression method fit for the along-isobath velocity for all values of L, but did not fit for the cross-isobath velocity (Table 3.9). The wavelength from the along isobath velocity ranged from 77 to 78 km, and from the speed, the wavelength was 68 km.

velocity component	κ_H $\times 10^{-4}$ (1/m)	total fitted profiles
u	0.8 to 0.82	5/5
v	NA	0/5
U	0.92	

Table 3.9: Calculated κ_H for along and cross-isobath velocity components and speed using the regression method for Sackville Spur mooring.

Estimates of ω from the spectra, and θ and κ_H from methods described earlier in the text were overlaid on the schematic of the dispersion relation as shown in Figure 3.7. As for the Flemish Cap mooring, all estimated variables from observations intersect, again suggesting topographic Rossby waves along the continental slope.

3.4.3 Flemish Pass

3.4.3.1 Wave-isobath angle, θ

The along-isobath angle for the Flemish Pass mooring location using L=64 to 80 km ranged from -92 to -92.6° with the same coordinate system as defined in Section 3.4.1. The spectrum

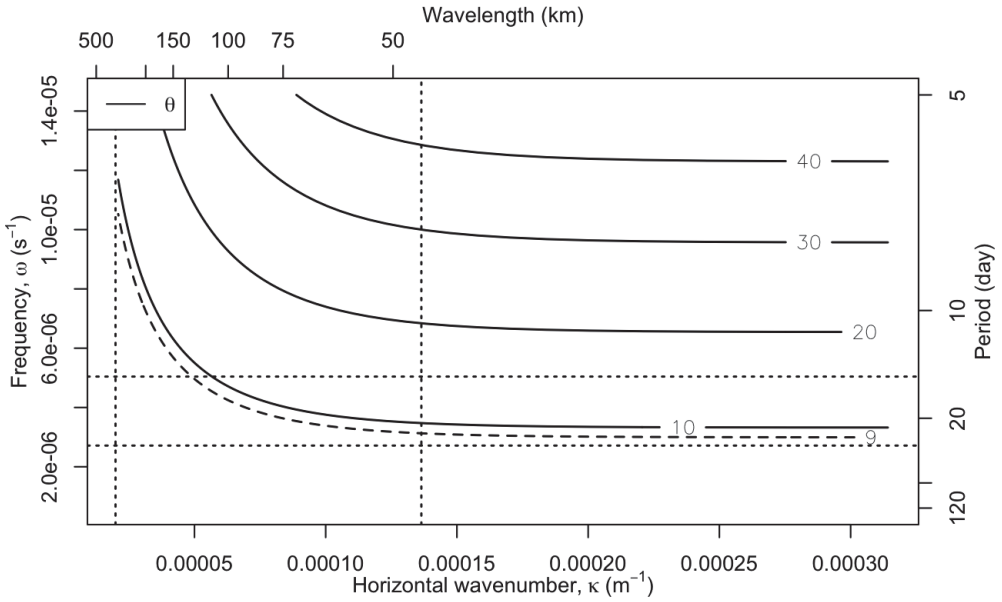

Figure 3.7: Contour plot of θ for given ω and κ_H from the dispersion relationship for topographic Rossby waves for the Sackville Spur mooring. Dotted vertical lines indicate range of κ_H from the two-point and regression method. Dotted horizontal lines indicate range of ω of the 3-week spectra peak. Dashed lines indicate range of θ inferred from data, note that the lower bound is not within the range of the plot

of the detided speed for the three week spectra peak was similar to the other two moorings, except the power did not increase as a function of depth. The deepest location had the lowest power, and a maximum power occurred at 318 m, as in the other moorings, the speed is vertically coherent. The calculated θ for each depth and each L is summarized in Table 3.10. Unlike the other two moorings, where the angle indicated upslope and downslope velocity direction, here velocity is downslope for the chosen depths, but again, the angle is small.

depth (m)	θ (°)
222	4.4 to 5
254	3 to 3.5
286	2 to 2.6
318	2.1 to 2.7
350	1.5 to 2.1
382	3 to 3.5

Table 3.10: Calculated θ range at each depth for Flemish Pass mooring

3.4.3.2 Horizontal wavenumber, κ_H

Again, results from the two-point method and the regression method for estimating κ_H will be presented using different values of L. For the two-point method, few values were able to be calculated as $R \geq 1$, which is outside the range permitted in Equation (3.31). For the along-isobath velocity component, three values of κ_H were calculated, the cross-isobath and speed, only one, Table 3.11. The calculated wavelength ranged from 63 to 119 km.

z_1-z_2 (m)	κ_H ($\times 10^{-4}$1/m) from u	κ_H ($\times 10^{-4}$1/m) from v	κ_H ($\times 10^{-4}$1/m) from U
222-254	0.84 to 0.84	NA	0.53
254-286	0.99 to 1	NA	NA
286-318	0.83 to 0.83	NA	NA
318-350	NA	NA	NA
350-382	NA	0.75 to 0.83	NA

Table 3.11: Calculated κ_H along and cross-isobath velocity components and speed using the two-point method for Flemish Pass mooring.

Similar to the other moorings, the regression method fit for all values of L for the along-isobath velocity component, however, for this mooring, the method did not fit for the cross-isobath velocity, or speed, Table 3.12. Resulting wavelength is 112 km.

To put these results in context, it should be noted that the bathymetry of Flemish Pass is fundamentally different to the other two mooring locations. The pass can be estimated to be a channel with a width of $\simeq 60$ km estimated from the 400 m isobath at the mooring latitude, with a length of $\simeq 300$ km. In *Stocker and Hutter* (1986), the dispersion relationship was developed for lakes for the barotropic case, therefore, conclusions based on the dimensions will be brief. Fitting Equation 4.1 of *Stocker and Hutter* (1986) results in a sidewall parameter $\epsilon \simeq 0.2$, the topographic parameter $q \simeq 1.5$, and a channel width, $B = 60$ km. These parameters, in particular, q, indicates that the channel is U-shape, indicating that wave activity could be near the sides of the channel (*Stocker and Hutter*, 1986). As stated by *Stocker and Hutter* (1986), the first mode of topographic Rossby waves is likely to be captured given that the mooring is placed within $0.05\,B$ to $0.1\,B$ from the edge, and the Flemish Pass mooring location is within this range. An extension of the model to the baroclinic case would describe the dynamics for the Flemish Pass, and then these data could be used to check the model, this will not be covered in this thesis.

velocity component	κ_H $\times 10^{-4}$ (1/m)	total fitted profiles
u	0.56 to 0.56	5/5
v	NA	0/5
U	NA	

Table 3.12: Calculated κ_H for along and cross-isobath velocity components and speed using the regression method for Flemish Pass mooring.

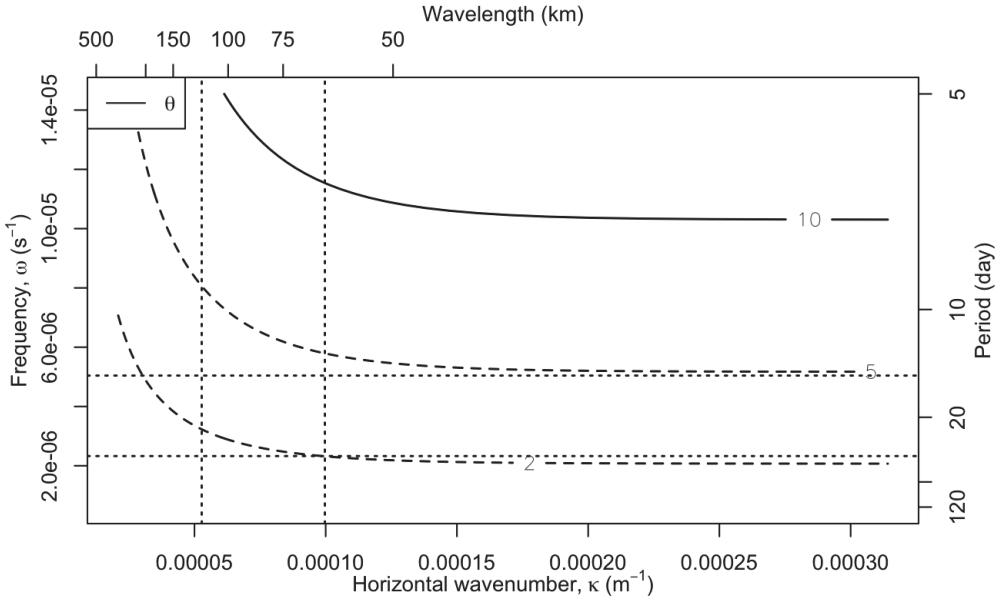

Figure 3.8: Dispersion relation diagram for Flemish Pass mooring.

3.5 Summary

The dispersion relationship as derived by *Rhines* (1970), was used to test if signatures summarized in Chapter 2, in particular, the 3-week spectral peak at each mooring, was consistent with topographic Rossby waves. Single mooring methods for estimating parameters in the dispersion relationship followed from *Thompson and Luyten* (1976). The results for this study region are as follows.

1. The stratification and slope are similar to other studies along the western Atlantic shelf. Compared to the other study in the sub-polar gyre, *Allen* (1980), the moorings of this study were placed on a steeper slope along the shelf.

2. Waters in the study region discussed in this thesis were more stratified than those in *Allen* (1980) study region.

3. The angle between the principal axes of velocity and isobaths was small, which is consistent with previous studies.

4. Both methods for inferring κ_H from a single mooring proved to not be suitable for all cases, and were sensitive to the choice of the along-isobath angle. The range of wavelengths agree with previous studies. Calculated wavelengths using the two-point and regression method overlapped, and between moorings, wavelengths overlap.

Given suitable lateral mooring spacing, the horizontal wave components, k and l, can be solved for. The spacing between the Flemish Cap and Sackville Spur mooring is $\simeq 80\,\text{km}$, the range of wavelengths calculated at these two locations was 26 to 315 km with a mean of 91 km. Ideally when resolving these wave components, the maximum resolution between measurements is half the wavelength. So with the moorings spacing, resolving the k-wavenumber component is not possible, and neither is it possible to infer the propagation direction.

In summary, the frequency-wavenumber characteristics observed in the moorings are consistent with the predictions of the theory of baroclinic topographic Rossby waves.

Chapter 4

Conclusions

This thesis summarized the spatial and temporal variability in the region of northern Flemish Cap. The spatial variability was summarized using CTD and LADCP station transects, which were roughly cross isobath about the location of each mooring in Chapter 2. The general circulation in the region was summarized. Along Sackville Spur, northeastward flow follows bathymetric contours, which is also prevalent along the northwest slope of Flemish Cap. Within Flemish Pass, flow is also surface intensified, with the position of the Labrador current varying between the western slope and the thalweg. Along the upper slope of Flemish Cap, all three transects suggest weak clockwise flow.

In terms of the spatial hydrographic properties, as discussed in Chapter 2, waters at depth have signatures of upper Labrador seawater in all transects, and Labrador seawater in the Flemish Cap and the northern section of Sackville Spur transects. All transects suggest the presence of a cold, fresh layer below the warm surface waters. Sea surface temperature suggests this water could be advected off the continental shelf, and may be the results of ice melt.

Temporal variability from the moorings, as discussed in Chapter 2, indicated low frequency variations in the detided, low-passed velocity data, with the power at this peak increasing as depth increases for each mooring. Wavelet analysis indicated that this low-frequency variability is most prevalent between January and June, corroborating a pattern that can also be seen by close inspection of the time-series graphs of the currents. The spectral peak was vertically coherent, also, there was lateral coherency below 750 m between the Sackville Spur and Flemish Cap mooring.

All of the above temporal characteristics are consistent with signatures of topographic

Rossby waves. This suggested a hypothesis that such waves are present in the study region. In Chapter 3, this hypothesis was tested in greater detail, through a comparison between the observations and the predictions of Rossby wave theory for the given stratification, bottom slope, *etc.*. The dispersion relationship, as derived in *Rhines* (1970), and the single moorings methods (due to mooring spacing) of *Thompson and Luyten* (1976), which were extended here, indicated that the 3-week peak found at all three moorings was, in fact consistent with topographic Rossby wave theory.

The results from this thesis can aid in issues ranging from the planning of offshore oil rigs to studying preferential habitats for benthic corals. For hydrocarbon drilling, knowledge of low frequency velocity variability will help in determining potential maximum stresses at depth, and can also help modelling a spill if an event were to occur. From a biological perspective, the time series will give insight about hydrographic conditions and flow regimes the benthic community is subject to over a time period of a year. For physical applications, it could could aid in the interpretation of past and future point measurements such as transport calculations from hydrographic surveys and momentum flux calculations. In particular, calculating the total average transport of the Labrador current in this region requires using at least 20 days of consecutive measurements. If modelled data are used to supplement observations, the model should capture the low frequency dynamics.

4.1 Future Work

This thesis has suggested low frequency variability which could be associated with topographic Rossby waves. With this region, and Rossby waves in mind, this could motivate the following future work

1. **Modelling.** Due to the complex bathymetry in the region, models may not capture the full dynamics, such as the sub-inertial timescales identified in this thesis. An investigation into this would aid in the event of a spill in order to identify areas of concern.

   A model which is currently used for this region is a NEMO based model with $1/12^{\circ}$ resolution with 50 vertical layers ranging from 1 m near the surface to 460 m in deep basins. Virtual mooring locations were chosen based on the hydrographic stations and mooring locations used in this thesis, and the model was ran by Zeliang Wang, a Physical Scientist at Bedford institute of Oceanography. Model output was every

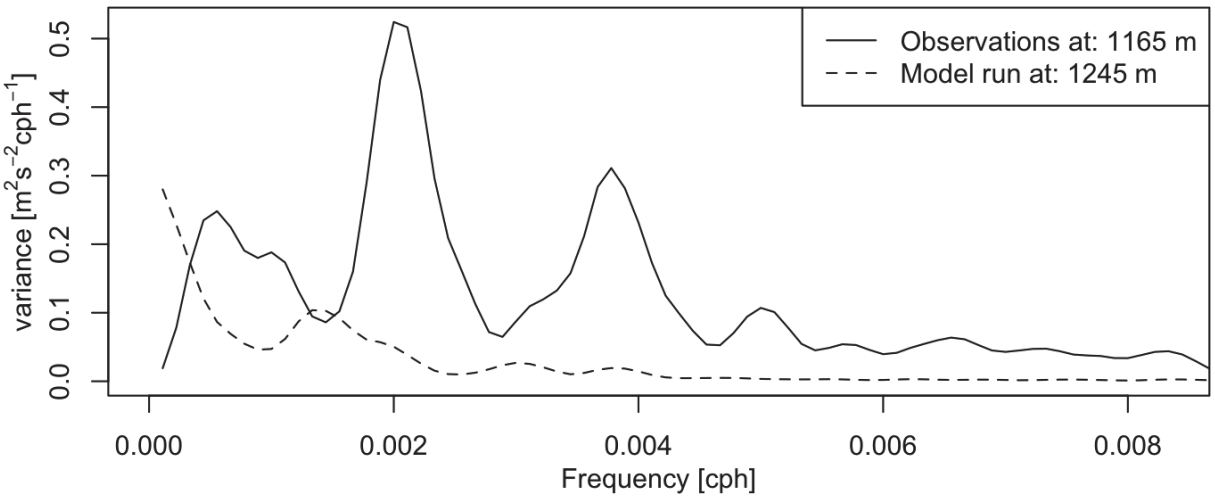

Figure 4.1: Spectra comparison of the de-tided speed observations from Flemish Cap mooring at 1165 m and speed from model at nearest level 1245 m

six hours. A brief comparison of the spectra of the moored observations from Flemish Cap at 1165 m and the nearest model level at 1245 m can be seen in Figure 4.1. As an initial test, the model spectrum of speed at the nearest level of observations does not encapsulate the low frequency signals found in the observations.

2. **Flemish Pass dynamics.** As noted in Chapter 3 (Section 3.4.3), the bathymetry is unique compared to the other moorings as it resembles a channel as opposed to simple planar bathymetry, as assumed in the derivation of the dispersion relationship. The dispersion relationship for Rossby waves in a channel was derived for lake dynamics, thus it does not take stratification into consideration. This theory could be extended for the ocean case, and then tested using these data.

3. **Mooring grid.** While the single mooring methods of *Thompson and Luyten* (1976), and its extension presented in this thesis, gave estimates of the wavelength, which were similar to previous studies, the range calculated at each location was large. In order to

   (a) obtain a better estimate of κ_H

   (b) estimate the horizontal wave components, k and l

   (c) estimate the phase speed and direction in the cross and along isobath direction

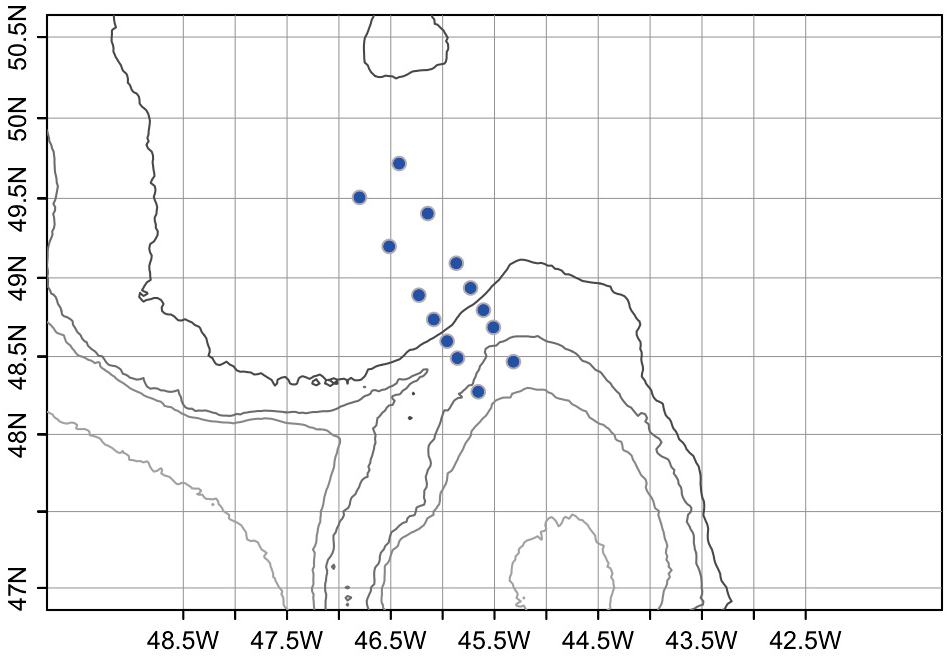

Figure 4.2: Suggestion of future mooring placement based on inferred values for Rossby waves as presented in this thesis, and similar in resolution to *Louis et al.* (1982). Chosen mooring lines are cross isobath, and distance between mooring lines is $\simeq 40\,\text{km}$.

multiple moorings would be required. Suggestions for moorings in the region to resolve the above is given in Figure 4.2. Previous studies, particularly *Louis et al.* (1982) has moorings along the shelf, slope, and rise, a similar setup was suggested here. Since vertical coherence was found generally below 185 m and 365 m for the Flemish Cap and Sackville Spur mooring respectively, it is suggested that current meters be placed at and below these depths. Also, as done in this study, it is suggested that current meters be placed at regular intervals, and at the same depths between each mooing. Given the choice of mooring placement about Flemish Pass and Sackville Spur, as suggested in Figure 4.2, it could also give insight about the bifurcation of the Labrador Current.

Appendix A

Data Details

The moored and shipboard data presented in this thesis are publicly available. To access the data, contact the Ocean Data and Information section at Bedford Institute of Oceanography, DataServicesDonnees@dfo-mpo.gc.ca

A.1 Moorings

Instrument	Ser. No.	Depth [m]	Filename
RCM-11	0456	759	MCM_HUD2013021_1840_0456_3600
RCM-11	0566	363	MCM_HUD2013021_1840_0566_3600
RCM-11	0612	556	MCM_HUD2013021_1840_0612_3600
RCM-11	0680	959	MCM_HUD2013021_1840_0680_3600
RCM-11	0684	1363	MCM_HUD2013021_1840_0684_3600
RCM-11	0685	1164	MCM_HUD2013021_1840_0685_3600
Microcat	2305	358	MCM_HUD2013021_1840_2305_300
Microcat	2306	559	MCM_HUD2013021_1840_2306_300
Microcat	2307	761	MCM_HUD2013021_1840_2307_300
Microcat	2415	1163	MCM_HUD2013021_1840_2415_300
Microcat	2436	1364	MCM_HUD2013021_1840_2436_300
Microcat	3062	961	MCM_HUD2013021_1840_3062_300
Microcat	3506	209	MCM_HUD2013021_1840_3506_300
Microcat	5831	57	MCM_HUD2013021_1840_5831_300
RDI ADCP	12556	18 - 186	MADCPS_hud2013021_1840_12556-106_3600

Table A.1: List of instruments for mooring 1840 with corresponding serial number and other parameters from cruise HUD2013021 with a sounding of 1408 m, a latitude of 48.7877 N and longitude 45.5998 E as inferred from ADCP.

Instrument	Ser. No.	Depth [m]	Filename
RCM-11	0265	1370	MCM_HUD2013021_1841_0265_3600
RCM-11	0376		MCM_HUD2013021_1841_0376_3600
RCM-11	0392		MCM_HUD2013021_1841_0392_3600
RCM-11	0397	363	MCM_HUD2013021_1841_0397_3600
RCM-11	0563	966	MCM_HUD2013021_1841_0563_3600
RCM-11	0598	563	MCM_HUD2013021_1841_0598_3600
Microcat	2775	1371	MCM_HUD2013021_1841_2775_300
Microcat	2797	1168	MCM_HUD2013021_1841_2797_300
Microcat	3061	969	MCM_HUD2013021_1841_3061_300
Microcat	3508	765	MCM_HUD2013021_1841_3508_300
Microcat	3509	564	MCM_HUD2013021_1841_3509_300
Microcat	3510	365	MCM_HUD2013021_1841_3510_300
Microcat	5324	216	MCM_HUD2013021_1841_5324_300
Microcat	5830	64	MCM_HUD2013021_1841_5830_300
RDI ADCP	3367	25 - 193	MADCPS_hud2013021_1841_3367-104_3600

Table A.2: List of instruments for mooring 1841 with corresponding serial number and other parameters from cruise HUD2013021 with a sounding of 1400 m, a latitude of 48.3627 N and longitude 46.5313 E as inferred from ADCP.

Instrument	Ser. No.	Depth [m]	Filename
Microcat	7374	402	MCM_HUD2013021_1842_7374_00000
RDI ADCP	3380	38 - 382	MADCPS_hud2013021_1842_3380-101_3600

Table A.3: List of instruments for mooring 1842 with corresponding serial number and other parameters from cruise HUD2013021 with a sounding of 408 m, a latitude of 47.0959 N and longitude 47.2813 E as inferred from ADCP.

Appendix B

Data Processing

The spectrum of the raw moored velocity data reveals high frequency variations associated with various tidal constituents, as well as power in the low frequencies. In order to focus on the low frequency variability, the data will be detrended by removing the tides, and then smoothed using various filtering techniques. The response on the time series and spectrum will be compared.

The spectrum estimated by a smoothed periodogram with a 10% taper, is detrended (linear with the mean removed), zero pad, and a twice applied modified Daniell kernel. The spectrum is smoothed in frequency space by a bandwidth as given in *Shumway and Stoffer* (2006, p.197 Equation (4.49)),

$$B_w = L/n \tag{B.1}$$

where L is value of the spans argument in the `spectrum()` function in R, which is represented as $L = 2m + 1$, where m is the width of the modified Danielle smoother, and n is the number of observations. Equation B.1 holds true for a once applied smoother. In general, from *Shumway and Stoffer* (2006, p.204 Equation (4.57)),

$$L = \left(\sum_{k=-m}^{m} h_k^2 \right)^{-1} \tag{B.2}$$

where h_k are the coefficients of the kernel. It is beneficial to use two different weights for the smoother as it yields a bell shaped kernel. Using the same values yields a flat-top kernel which can affect narrow spectral peaks. Also, too large of a bandwidth can cause flattening of a peak and spectral leakage. If a spectral peak is present, a 95% confidence interval of the power can be constructed using a chi-squared distribution, $\chi^2_{df}(0.025)$ and $\chi^2_{df}(0.975)$

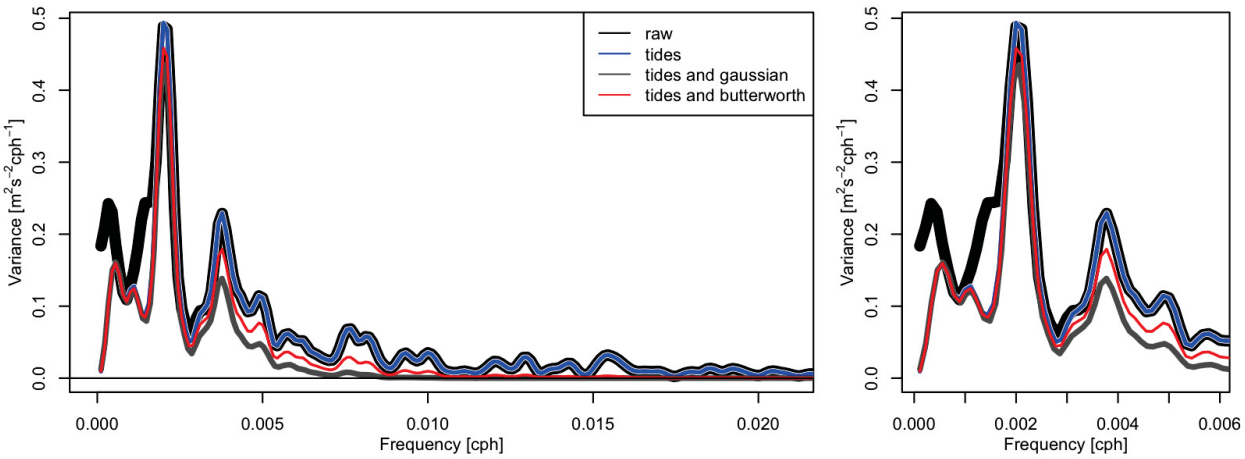

Figure B.1: Spectrum response of u velocity from various filtering techniques

where df is the adjusted degrees of freedom as defined in *Shumway and Stoffer* (2006, p.198 Equation (4.53)),

$$df = \frac{2\,L\,n}{n'} \tag{B.3}$$

where n' is calculated using the `nextn()` function in R, which takes the value of n (*R Core Team*, 2015). The confidence interval can be used as an indicator to determine if spectral peaks are more significant than the baseline spectrum.

In order to remove the tides, tidal constituents are fitted with a series of sines and cosines using pre-defined methods (*Foreman*, 1977; *Pawlowicz et al.*, 2002; *Kelley and Richards*, 2016). De-tiding removes low frequency tidal constituents such as the solar annual (SA), solar semiannual (SSA), solar monthly (MSM), lunar monthly (MM), lunisolar synodic fortnightly (MSF), and lunisolar fortnightly (MF) (Figure B.1). Low frequency spectral peaks remain after detiding, indicating that some other physical process is associated with this low frequency variability. Also, after detiding, high frequency variability remains in the time series, Figure B.2.

In order to remove the remaining high frequencies, a low-pass filter will be applied. Here two filters will be compared. A 95% Gaussian with a filter length of 1152 hours was applied to the detided horizontal velocity components. A first order Butterworth filter with a cut-off period of 48 days was applied to detided horizontal velocity components. A first order filter was used over higher orders to reduce the effects of side-lobes in the time series which might leak into the spectrum, resulting in false peaks.

Both filter adequately smooth the data, with the Butterworth retaining more information.

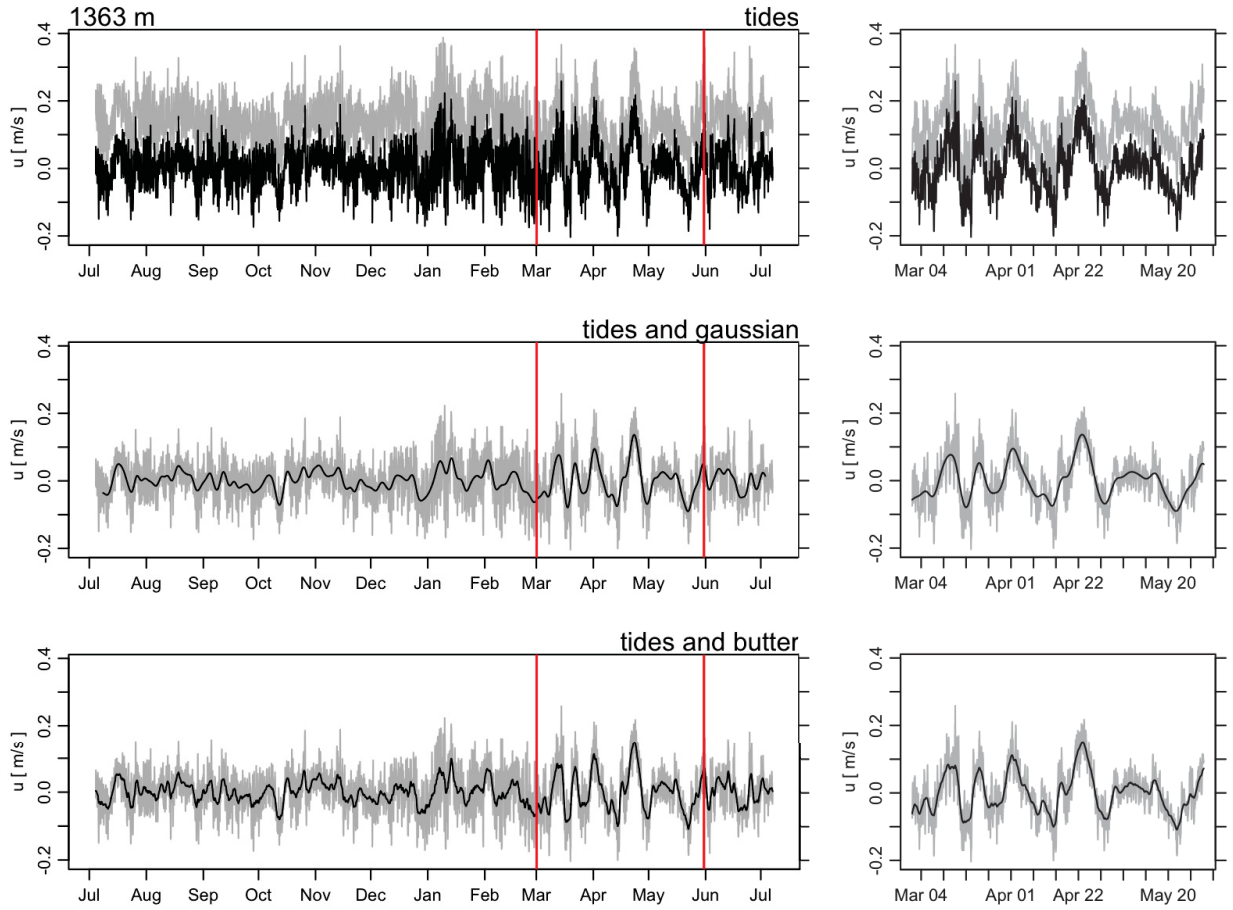

Figure B.2: Time-series of u velocity component with various filtering. Grey is the raw (top) or detided (middle and bottom), and black indicates the filtered data. Red vertical lines indicate a subset of the data in order to see more details. (Top) Raw and de-tided, (Middle) Detided and low-pass Gaussian, (Bottom) Detitded and low-pass Butterworth.

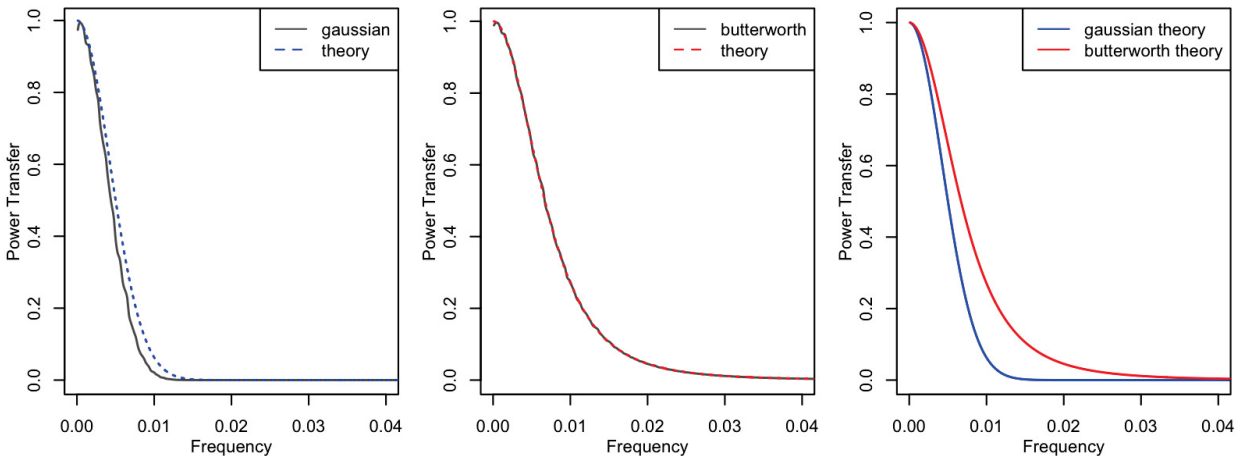

Figure B.3: Gaussian and Butterworth filter transfer function. Random numbers were generated with similar length and sample frequency as velocity data in order to compare with theoretical transfer function. (Left) Observational transfer function (black line), and the theoretical transfer function (dashed blue line) for a Gaussian filter with a filter length of 1152. (Middle) Observational transfer function (black line), and theoretical transfer function (dashed red line) for a first order Butterworth filter with a cutoff period of 48 days. (Right) Comparison of the theoretical transfer functions for Gaussian (blue) and Butterworth (red) filters.

From the time series, both filters look similar, however, low-pass filters can have varying responses on the spectral output. The power transfer function explains the frequency response on a system. Functions for both filters is compared (Figure B.3). The response on a spectrum that a filter has gives information about the power reduction of spectral peak within some range. For example, if a spectral peak is present at the half power frequency, after low-passing the observations, the spectral peak would have half the power of the pre-filtered data. The Gaussian has a half power period at 9.59 days, and the first order Butterworth filter at 6.075 days.

Low-passing the data removes the remaining high frequency variability in the velocity data, however, in the spectrum, it reduces the power of the low frequency spectral peaks. The Butterworth filter will be used over the Gaussian filter because it does not reduce the length of the time series. For example, using a filter length of 1152 removes 576 observations at the beginning and end of the time series, whereas the Butterworth filter retains the length of the original time series.

Appendix C

Upslope Angle Methods

C.1 Methods

C.1.1 Two-point

Using high-resolution bathymetry data, a circle with radius L is drawn around a point $\mathcal{P}_0 = (\lambda_0, \theta_0)$, where λ is longitude and θ is latitude. The maximum and minimum depths along the circle are found. Defining the minimum and maximum depth points points as $\mathcal{P}_S$ and $\mathcal{P}_D$ respectively, in spherical vector notation where the xy plane lies along the plane of the equator, or the longitudinal axis, with λ negative/positive west/east of 0°, and the z-axis is about the earth's axis, where θ is positive from the equator,

$$\mathcal{P}_S = (\cos\theta_S \cos\lambda_S,\, \cos\theta_S \sin\lambda_S,\, \sin\theta_S) \tag{C.1}$$

$$\mathcal{P}_D = (\cos\theta_D \cos\lambda_D,\, \cos\theta_D \sin\lambda_D,\, \sin\theta_D) \tag{C.2}$$

using the spherical law of cosines, the central angle, ϕ, between the two points with respect to the centre of the Earth is,

$$\cos\phi = \mathcal{P}_D \cdot \mathcal{P}_S \tag{C.3}$$

solving for ϕ yields

$$\phi = \cos^{-1}\left(\sin\theta_D \sin\theta_S + \cos\theta_D \cos\theta_S \cos(\lambda_D - \lambda_S)\right) \tag{C.4}$$

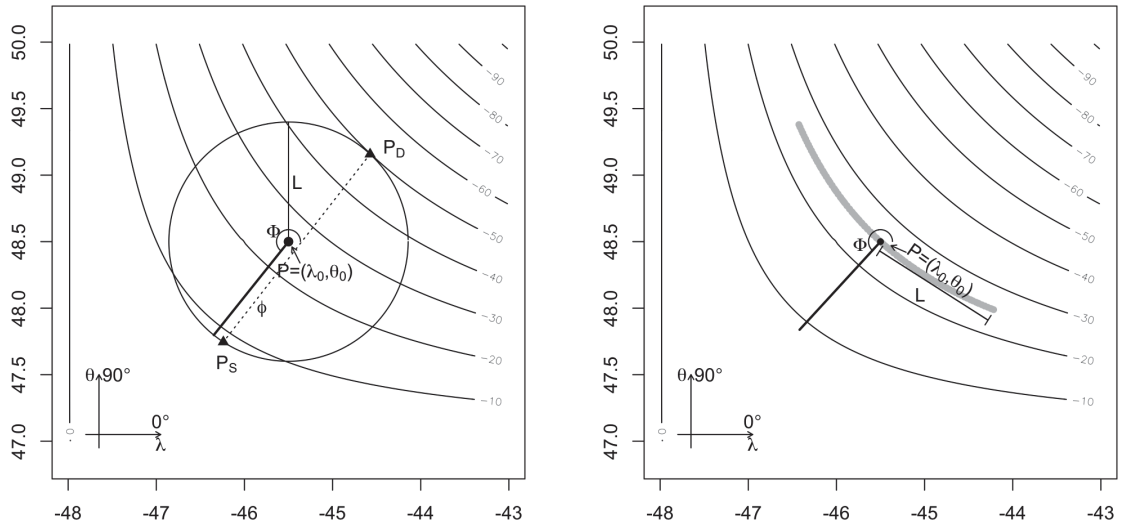

Figure C.1: Schematics of both upslope angle methods. (a) Two-point method. Black dot indicates the point, $\mathcal{P}$, in which the upslope angle is desired. The triangles indicate $\mathcal{P}_S$ and $\mathcal{P}_D$, along the circle drawn with radius L about $\mathcal{P}$. The dashed line is the angle between $\mathcal{P}_S$ and $\mathcal{P}_D$ with respect to the centre of the Earth. The thick line indicates the upslope direction for this bathymetry. (b) Contour method. Black dot indicates the point, $\mathcal{P}$ and the grey dots are the points along the contour of length $2L$ about $\mathcal{P}$. The thick black line is the upslope direction.

using results from Equation C.4, the heading Φ_n, which is the upslope angle in the geographic coordinate system where 0° points north with positive angle clockwise,

$$\Phi_n = \cos^{-1}\left(\frac{\sin\theta_D - \sin\theta_S\cos\phi}{\sin\phi\cos\theta_S}\right) \tag{C.5}$$

for consistency between the methods, the angle will be given in terms of the normal Cartesian coordinate system where 0° points east, with a positive angle anti-clockwise, Φ_c, using the simple transformation,

$$\Phi_c = 90 - \Phi_n \tag{C.6}$$

C.1.2 Contour

Using bathymetry data, the (λ, θ) grid is converted to (x, y) space using geodesic calculations. Similar to the spherical method, a circle of radius L is draw around point $\mathcal{P}_0 = (x_0, y_0)$, and all points within the circle are retained. The depth, z_p, at $\mathcal{P}_0 = (\lambda_0, \theta_0)$, and points along the contour depth are found, Figure C.1(b). The points along the contour are converted to (x, y)

space. A co-variance matrix gives the amount of variance between i^{th} number of variables, which is expressed as

$$\Sigma_{i\,j} = cov(X_i, X_j) = E\left[(X_i - \mu_i)(X_j - \mu_j)\right] \tag{C.7}$$

where $\Sigma_{i\,j}$ is the $n \times n$ co-variance matrix, and $\mu_i = E(X_i)$, or the expected value of the i^{th} component. For the case where $i = j$, this is the variance of the i^{th} component. The axes of the systems co-variance can be described by the eigenvalues and eigenvectors of $\Sigma_{i\,j}$. In vector notation, the eigenvalues are the roots of the co-variance matrix,

$$\mid \Sigma_{i\,j} - \lambda I \mid = 0 \tag{C.8}$$

where λ is an eigenvalue, which could be zero or nonzero, and I is the $n \times n$ identity matrix. The eigenvector, $\mathbf{x}$, associated with λ, is a nonzero vector such that

$$\Sigma_{i\,j}\mathbf{x} = \lambda\mathbf{x} \tag{C.9}$$

where $\mathbf{x}$ has dimensions $n \times 1$. And

$$\left(\Sigma_{i\,j} - \lambda I\right)\mathbf{x} = \mathbf{0} \tag{C.10}$$

For a simple 2 variable system, putting the eigenvector associated with each eigenvalue as columns in a matrix gives the rotation matrix,

$$\begin{pmatrix} \cos\Phi & -\sin\Phi \\ \sin\Phi & \cos\Phi \end{pmatrix} \tag{C.11}$$

where Φ is the angle of rotation. Therefore, Φ can be calculated,

$$\Phi = \tan^{-1}\left(\frac{\sin\Phi}{\cos\Phi}\right) \tag{C.12}$$

which is simply the eigenvector associated with the eigenvalue which describes variance of the along slope axes component. To obtain the upslope angle in the normal Cartesian coordinate system, 90° is added.

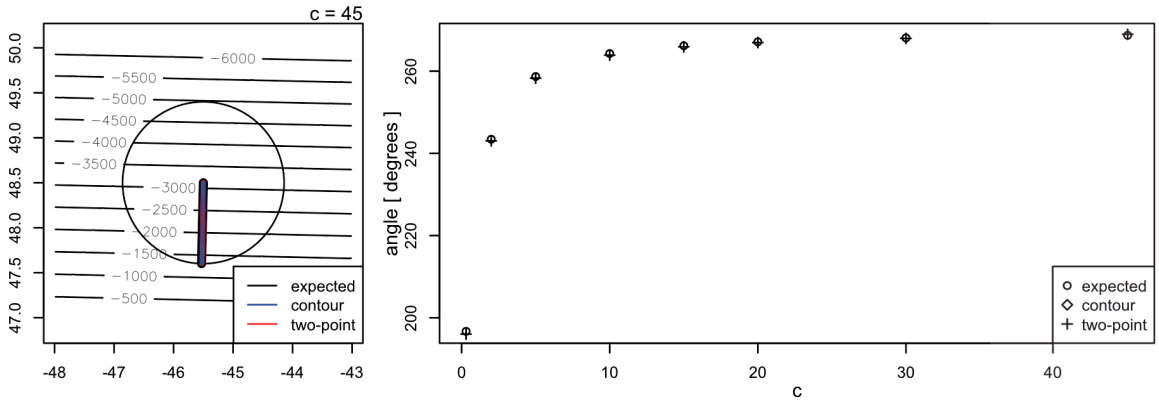

Figure C.2: Comparison of methods using idealized bathymetry. (Left) Example of idealized bathymetry, with a circle of radius L about point $\mathcal{P}$ (see Figure C.1 for variable definition). Resulting upslope angle found from both methods, along with the expected angle. Example is with $c = 45$. (Right) Resulting angles from both methods compared to expected angle for various values of c.

C.2 Results

To compare both methods, first, idealized bathymetry with varying upslope angles was tested. Following that, using real bathymetry data, different values of L will be chosen and compared for varying bathymetry complexity.

C.2.1 Idealized Bathymetry

To construct idealized bathymetry data, a matrix is filled using a linear function of the form $a + bx + cy$ in order to easily calculate the upslope angle. For simplicity, take $a = 0$, $b = 1$, and vary c. The upslope angle is calculated as $\tan^{-1}(c) + 180$.

Upon completing test cases of the two-point, for certain cases, the resulting angle was the complement angle about 270°. From Equation C.5, $\cos^{-1}$ only returns angles between $0 \leq \Phi_n \leq \pi$. To correct the angle, if $|\lambda_{min}| > |\lambda_{max}|$, then

$$\Phi_c = 90 + \Phi_n \tag{C.13}$$

Using idealized bathymetry, both methods should return values close to the expected angle. As in Figure C.2, both methods estimate the upslope angle within 0.10°, therefore both methods are satisfactory for estimating the upslope angle.

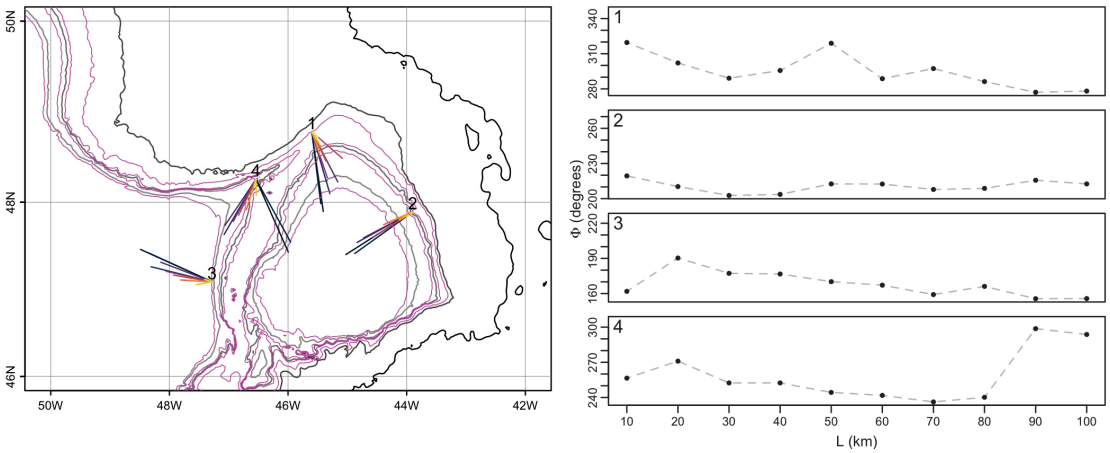

Figure C.3: Test locations for two-point method. (Left) Selection of points with varying bathymetry complexity. Lines from each point are the calculated Φ_c proportional to L. (Right) L vs. Φ_c for each location. Note that the y-axes have the same range of values.

C.2.2 Values of L

For the two-point method, sensitivity to L will be tested by arbitrarily choosing this length, as no methods for choosing it have been formulated. For the contour method, methods will be constructed to choose suitable values of L based on the total water depth, H and the baroclinic Rossby radius.

C.2.2.1 Two-point

In previous uses of this method, values of L ranged from 25-100 km. Here, 10 lengths between 10 and 100km are used to test sensitivity.

For simple bathymetry, points 2 and 3 in Figure C.3, the range of estimated Φ is within 30° for $10 < L < 100$km. A point of relatively simple bathymetry, point 1, the range increases to 40°. For complex bathymetry, point 4 in Figure C.3, the range of Φ is 70°. The method is sensitive to L, but, in general, choosing a mid range value of L reduces the sensitivity in most cases. For example, in Figure C.3, choosing $40 < L < 70$km reduces the range of Φ, except for point 1, where there is still a wide range of Φ.

C.2.2.2 Contour

In order to estimate a suitable range of L, for the contour method, a set of lengths will be tested. Setting the maximum value of L,

$$L_{max} = H \times 10^2 \tag{C.14}$$

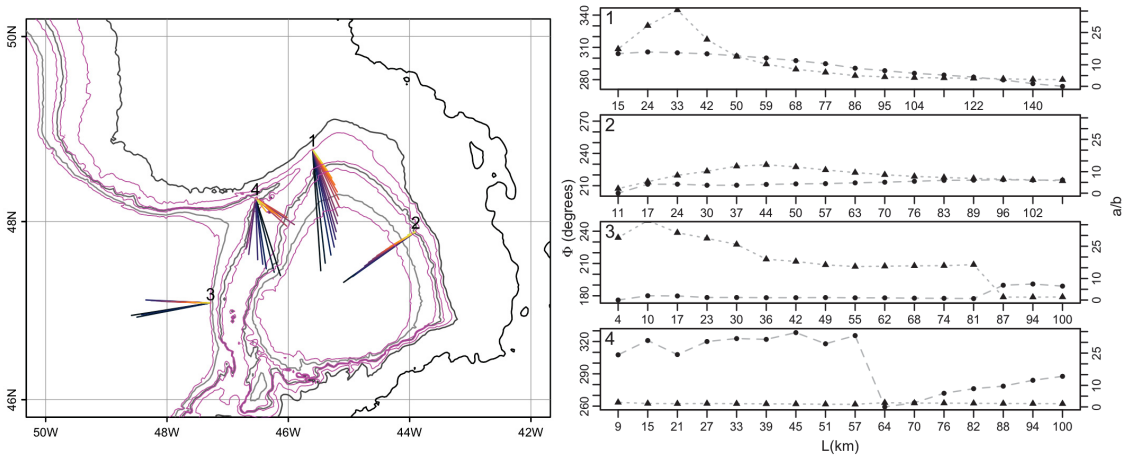

Figure C.4: Test locations for contour method, same locations as Figure C.3. (Left) Selection of points with varying bathymetry complexity. Lines from each point are the calculated Φ proportional to L. (Right) L vs. Φ as indicated by the dots. L vs a/b, where a is the major axis and b is the minor axis, equivalently it is the ratio of the eigenvalues, as indicated by the triangles. Note the different x-axis values for each test point.

and the minimum L to be the baroclinic Rossby radius for continuously stratified flow,

$$L_{min} = \frac{\sqrt{g'H}}{f} \tag{C.15}$$

where g' is reduced gravity,

$$g' = -H\left(\frac{g}{\rho}\frac{\partial \rho}{\partial z}\right) \tag{C.16}$$

$$= N^2 H \tag{C.17}$$

so L_{min} is

$$L_{min} = \frac{NH}{f} \tag{C.18}$$

for the Flemish Cap region $N \sim 10^{-3}s^{-1}$ and $f \sim 10^{-4}s^{-1}$, so $L_{min} \sim 10H$, where H is the water depth. A conditional L_{max} and L_{min} is set for $H < 500$m, where $10 \leq L \leq 100$km, in order for there to be a sufficient number of data points in the eigenvalue analysis. Using n number of L ranging from L_{min} to L_{max}, the method is tested for varying complexity of bathymetry.

Points of simple bathymetry, points 2 and 3 of Figure C.4, results in Φ that do not vary much based on the value of L. For point 1, which has relatively simple bathymetry, has a

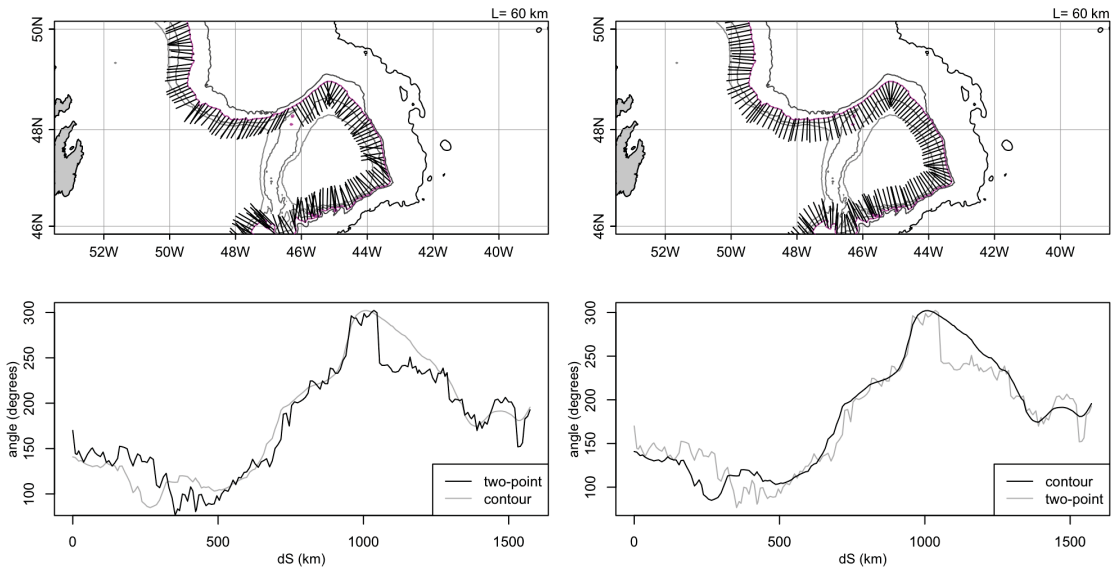

Figure C.5: Comparison of both methods along a line element , dS, using $L = 60$km. In the top plots, lines indicate Φ at a given point along dS which is proportional to L. Bottom plots are the calculated angle along the contour. (Left) Two-point method. (Right) Contour method. Grey lines in the bottom panels are from the alternative method and provided for comparison.

similar range of Φ as the spherical method.

The ratio of the eigenvalues can help identify a suitable sub-range of L to choose from. Larger values of the ratio indicates a larger amount of variance in the along slope direction than the cross shore direction, or simply the straightness of the bathymetry. For points 1-3, Figure C.4 (Right), reducing the range of L to be between points where the eigenvalue ratio is greater than 10 reduces the variance of Φ. However, for complex bathymetry, point 4, finding a sub-range of L is difficult and fails when using the criteria above.

C.3 Conclusion

The two-point method for finding upslope direction utilizes simple known geometric properties of the Earth to find the heading between two points. The parameter choice of L proved to be sensitive for a given point, and yields a wide range of Φ, regardless of the simplicity or complexity of the bathymetry.

The application of eigenvalue analysis demonstrates the flexibility and suitability of this statistical technique. The choice of the free parameter L was narrowed using the ratio of the eigenvalues. The criteria for the ratio is suitable for most bathymetry except for those which

have nearly equal variance in both the longitude and latitude directions.

Along a contour line, Figure C.5, using the same L for both methods yields similar Φ for a given point along the line. To test if there is a significant difference between the choice of L for each unique method, a one-way anova test,

$$\Phi_{ik} = L_k \tag{C.19}$$

where $i = 1, \ldots, I$ is the experimental unit, here it is the calculated angle at each unique point along the contour, and $k = 1, \ldots, K$ is the response unit, here it is the values of L. The test will be applied to both methods using the same values of L, which range from $10 < L < 100$ km. The goal is to see if there is a significant difference between successive values of L. Both methods do not have any statistical significance between calculated values of Φ and successive values of L.

To check if there is a significant difference between the two methods for the same value of L, a two-way factorial anova,

$$\Phi_{ikj} = L_k + G_j \tag{C.20}$$

where i and k are the same as the one-way anova. $j = 1, \ldots, J$ is another response unit which corresponds to the two described methods. There is no statistical significance between the two methods using the same value of L.

While there is no statistical significance between the choices of L and between the two methods, the eigenvalue method solves the choice of the free parameter L, which is arbitrarily chosen and sensitive for the spherical method. A suitable range of L for a given point can be found by those values where the ratio of the eigenvalues is greater than 10.

Bibliography

Allen, A., Current variability at the offshore edge of the Labrador current, Master's thesis, Dalhousie University, 1980.

Bower, A., S. Lozier, and S. Gary, Export of Labrador Sea water from the subpolar North Atlantic: A Lagrangian perspective, *Deep Sea Research Part II*, *58*, 1798–1818, 2011.

Colbourne, E. B., and K. D. Foote, Variability of the stratification and circulation on the Flemish Cap during the decades of the 1950s - 1990s, *Journal of Northwest Atlantic Fishery Science*, *26*, 103–122, 2000.

Cushman-Roisin, B., *Introduction to geophysical fluid dynamics*, Prentice Hall, 1994.

Fischer, J., and F. A. Schott, Labrador Sea water tracked by profiling floats - from the boundary current into the open north Atlantic, *Journal of Physical Oceanography*, *32*, 573–284, 2002.

Flament, P., A state variable for characterizing water masses and their diffusive stability: spiciness, *Progress in Oceanography*, *54*, 493–501, 2002.

Foreman, M., *Manual of tidal heights analysis and prediction*, Pacific Marine Science Report, 1977.

González-Costas, F., and D. González-Troncoso, Spanish 2006-2008 fisheries footprint, scientific observers and surveys coverage and update of the standardized cpue indices for greenland halibut., *NAFO SCR Doc. No. 22, Serial No. N5657*, p. 16 pages, 2009.

Hartigan, J. A., and M. A. Wong, Algorithm as 136: A k-means clustering algorithm, *Journal of the Royal Statistical Society. Series C (Applied Statistics)*, *28*, 100–108, 1979.

Kelley, D., and C. Richards, *oce: Analysis of Oceanographic data*, 2016, r package version 0.9-20.

Kieke, D., M. Rhein, L. Stramma, W. M. Smethie, D. A. LeBel, and W. Zenk, Changes in the CFC inventories and formation rates of upper Labrador Sea water, 1997-2001, *Journal of Physical Oceanography*, *36*, 64–86, 2006.

Lavender, K. L., R. E. Davis, and W. B. Owen, Mid-depth recirculation observed in the interior Labrador and Irminger Seas by direct velocity measurements, *Nature*, *407*, 66–69, 2000.

Lazier, J. R. N., and D. G. Wright, Annual velocity variations in the Labrador current, *Journal of Physical Oceanography*, *23*, 659–678, 1993.

Louis, J. P., B. D. Petrie, and P. C. Smith, Observations of topographic Rossby waves on the continental margin off Nova Scotia, *Journal of Physical Oceanography*, *12*, 47–55, 1982.

Lowe, D. G., P. J. Sylvester, and M. E. Enachescu, Provenance and paleodrainage patterns of upper jurassic and lower cretaceous synrift sandstones in the flemish pass basin, offshore newfoundland, east coast of canada, *AAPG bulletin*, *95*, 1295–1320, 2011.

Meinen, C., E. Fields, R. Pickart, and D. R. Watts, Ray tracing on topographic rossby waves, *Tech. rep.*, Univeristy of Rhode Island, 1993.

Mertens, C., M. Rhein, M. Walter, G. W. Boning, E. Behrens, D. Kieke, R. Steinfeldt, and U. Stober, Circulation and transports in the Newfoundland basin, western subpolar North Atlantic, *Journal of Geophysical Research: Oceans*, *119*, 7772–7793, 2014.

Murillo, F., P. D. Munoz, A. Altuna, and A. Serrano, Distribution of deep water corals of the flemish cap, flemish pass and the grand banks of newfoundland (northwest atlantic ocean): interaction with fishing activities, *Journal of Marine Science*, *68*, 319–332, 2011.

Murillo, F. J., P. D. Muñoz, J. Cristobo, P. Ríos, C. González, E. Kenchington, and A. Serrano, Deep-sea sponge grounds of the Flemish Cap, Flemish Pass and the Grand Banks of Newfoundland (northwest Atlantic Ocean): distribution and species composition, *Marine Biology Research*, *8*, 842–854, 2012.

Northwest Atlantic Fisheries Organization, Northwest Atlantic Fisheries Organization conservation and enforcement measures, *Doc 15/1 Serial No. N6409*, NAFO, 2015.

OSPAR, C., Ospar list of threatened and/or declining species and habitats, *Reference Number: 2008-6*, p. 4 pages, 2008.

Pawlowicz, R., B. Beardsley, and S. Lentz, Classical tidal harmonic analysis including error estimates in matlab using t_tide, *Computers & Geosciences*, *28*, 929–937, 2002.

Petrie, B., and J. Buckley, Volume and freshwater transport of the Labrador current in Flemish Pass, *Journal of Geophysical Research*, *101*, 28335–28342, 1996.

Pickart, R. S., Gulf Stream-generated topographic Rossby waves, *Journal of Physical Oceanography*, *25*, 574–586, 1995.

Pickart, R. S., Eddies of newly formed upper Labrador Sea water, *Journal of Geophysical Research*, *101*, 20711–20726, 1996.

R Core Team, *R: A Language and Environment for Statistical Computing*, R Foundation for Statistical Computing, Vienna, Austria, 2015.

Rhines, P., Edge-, bottom-, and Rossby waves in a rotating stratified fluid, *Geophysical Fluid Dynamics*, *1*, 273–302, 1970.

Rossby, T., Visualizing and quantifying oceanic motion, *Annual Review of Marine Science*, *8*, 35–57, 2016.

Schneider, L., D. Kieke, K. Jochumsen, E. Colbourne, I. Yashayaev, R. Steinfeldt, E. Varotsou, N. Serra, and M. Rhein, Variability of Labrador Sea water transported through Flemish Pass during 1993-2013, *Journal of Geophysical Research: Oceans*, 2015.

Shumway, R. H., and D. S. Stoffer, *Time Series Analysis and Its Applications With R Examples*, 2 ed., Springer New York, 2006.

Stocker, T., and K. Hutter, One-dimensional models for topographic rossby waves in elongated basin on the f-plane, *Journal of Fluid Mechanics*, *170*, 435–495, 1986.

Stramma, L., D. Kieke, M. Rhein, F. Schott, I. Yashayaev, and K. P. Koltermann, Deep water changes at the western boundary of the subpolar North Atlantic during 1996 to 2001, *Deep Sea Research Part I*, *51*, 1033–1056, 2004.

Talley, L. D., and M. McCartney, Distribution and circulation of Labrador Sea water, *Journal of Physical Oceanography*, *12*, 1189–1205, 1982.

Thompson, R. O. R. Y., and J. R. Luyten, Evidence for bottom- trapped topographic Rossby waves from single moorings, *Deep Sea Research*, *23*, 629–635, 1976.